Spectroscopy of the $A = 33$ Isobars in the Island of Inversion

A dissertation presented to

the faculty of

the College of Arts and Sciences of Ohio University

In partial fulfillment

of the requirements for the degree

Doctor of Philosophy

Andrea L. Richard

May 2018

This dissertation titled

Spectroscopy of the $A = 33$ Isobars in the Island of Inversion

by

ANDREA L. RICHARD

has been approved for

the Department of Physics and Astronomy

and the College of Arts and Sciences by

Heather L. Crawford

Assistant Professor of Physics and Astronomy

Robert Frank

Dean, College of Arts and Sciences

Abstract

RICHARD, ANDREA L., Ph.D., May 2018, Physics

Spectroscopy of the A = 33 Isobars in the Island of Inversion (135 pp.)

Director of Dissertation: Heather L. Crawford

The question of the immutability of the traditional "magic numbers" and structure of exotic nuclei near to shell closures has long been an area of interest both experimentally and theoretically. The neutron-rich $_{12}$Mg isotopes around N=20 are examples of a region where the expected spherical shell gap has narrowed or disappeared entirely. The "Island of Inversion," centered around ^{32}Mg, is a region where a narrowed N=20 shell gap and collective *np-nh* excitations result in nuclei with deformed ground states. However, despite years of theoretical and experimental efforts, a complete picture of the detailed nature of deformation in this region has not been achieved and the level schemes remain largely incomplete for many of these neutron-rich nuclei. Furthermore, the presence of rotational band structures, which are key signatures of deformation, have only recently been observed in this region.

Two experiments were performed at the National Superconducting Cyclotron Laboratory (NSCL) in order to probe the structure of the A=33 isobars in the "island of inversion." A β-decay experiment (NSCL e14063) was performed to investigate the level schemes and decay schemes for the decay of ^{32}Na $\rightarrow$ ^{32}Mg, ^{33}Na $\rightarrow$ ^{33}Mg, ^{33}Na $\rightarrow$ ^{33}Mg $\rightarrow$ ^{33}Al, and ^{33}Mg $\rightarrow$ ^{33}Al. The details of the experiment are discussed and level schemes and decay schemes, along with the implications for the observed structure. Additionally, the half-lives for ^{32,33}Na and ^{33}Mg were determined.

A measurement (NSCL e11029) of the low-lying level structure of ^{33}Mg populated by a two-stage projectile fragmentation reaction and studied with GRETINA was also performed. The experimental setup is discussed along with the γ-ray singles and $\gamma - \gamma$ coincidence analysis used to construct the level scheme for ^{33}Mg. The experimental

level energies, ground state magnetic moment, intrinsic quadrupole moment, and γ-ray intensities are compared to a leading order rotational model in the strong-coupling limit. Lastly, the level schemes from both measurements are discussed along with potential future projects.

To my mom, who shaped me into the person I am today and introduced me to coffee. To my dad, who is no longer with us, but is always in my heart. To Kyle, my brother, who never fails to help in whatever way he can. To Ashley, my sister, who shows me what it means to be strong. To Brittany, my amazing friend, who loves Jane Austen as much as I do and continues to impress me daily. To Bella, who makes me smile on a daily basis and brings me joy. To Larousse, who gave me support when I needed it most and will forever be my best friend.

ACKNOWLEDGMENTS

First, I want to thank my advisor and mentor, Heather Crawford. Thank you for your guidance, kindness, and patience, and for seeing me through my Ph.D. I know it was not always easy and that you did not have to remain my advisor, but I will be forever grateful that you did. Thank you for everything.

I could not have accomplished all that I did without the support of the Nuclear Structure group at LBNL, especially Augusto Macchiavelli and Paul Fallon. They supported my trips to LBNL and made me feel like part of the group. Their guidance with our rotational band work has been invaluable and their love for coffee matches my own. I loved every moment of my time in Berkeley and my experiences there.

Carl Brune, you have been a constant source of support for me over these past few years. Thank you for agreeing to be my local supervisor and for mentoring me. I cannot say how grateful I am for you and Roxanne.

A huge debt of gratitude goes to members of my committee, Daniel Phillips, Alexander Neiman, and Katherine Cimatu who took time out of their busy schedules to read my dissertation and get me through this process. Thank you!

I also owe my gratitude to David Ingram, who let me join him in material science pursuits for the last few years. The experience has allowed me to spread my wings and learn how to be a better researcher.

In truth, I owe thanks to the entire Physics and Astronomy Department for their educational efforts, encouragement, and support throughout the past few years. I am particularly grateful for Tracy Robson, Candy Dishong, and Candi Spaulding for their assistance with every little thing that came up. They always found a way to make me smile and for that I am truly grateful. The staff of the Edwards Accelerator Lab, Don Carter and Devon Jacobs, are some of the best, most helpful people that I have ever met. Their technical support was invaluable.

To my friends in the Edwards Accelerator Lab, thank you. From coffee to lunch, study sessions and midnight shifts, we have had an amazing time and you've each influenced me. Cody took me under her wing when I first arrived in Edwards and enabled my coffee and tea addictions. To Tyler, Theresa, Nick, Britny, Perry, and Thushan, I say thank you. Our weekly "bro lunch" and monthly "bro dinners" were wonderful and I will truly miss all of you. To Tyler, Kristyn, and Doug, you guys have truly made me laugh these past few years. Thank you for all of the chats, Franco's Fridays, and coffee. I will miss all of you. Larousse, you have been my support over the last few years. You are a true friend and someone whose kindness is unending.

Lastly, I am so thankful for my family. In no small part, they are the reason that I am getting my Ph.D. They inspire me, push me, and love me unconditionally. My dad always said that I could do whatever I set my mind to and he was right. His tenacity and gentle spirit are big parts of my life and drive me to keep learning and to never lose sight of who I am. Mom, you are my guiding light, my inspiration, and the kind of person that I aspire to be. You are my heart.

Table of Contents

List of Tables

List of Figures

1 Introduction

Every physical thing in our universe is composed of atoms. Experimental and theoretical studies of atomic matter throughout the years have probed the very nature of the composition of matter and how it came into being, and have shown that matter, and the objects that we interact with on a daily basis are composed of smaller and smaller constituents. The nucleus resides at the center of the atom and occupies approximately 10^{-15} of the atom's volume and yet the majority of its mass. The nucleus itself is a many-body system made up of protons and neutrons, or nucleons. Together these nucleons combine to form the elements in the periodic table, and more generally all of the isotopes in the chart of the nuclides, or the nuclear landscape.

1.1 The Nuclear Landscape

The nuclear landscape consists of nuclei having varying numbers of protons and neutrons. Protons are the positive charge-carriers and are denoted with Z, while neutrons are neutral and are denoted as N. A particular nucleus is defined by the total number of protons it contains and its mass, denoted by A, where $A = Z + N$. Any nucleus can be denoted as ${}^{A}_{Z}X_{N}$, where X is the symbol from the periodic table of the elements. Variation in the number of neutrons for a particular element gives rise to different isotopes. The chart of the nuclides, or the Segré chart, is a map of all of the isotopes, stable or otherwise, laid out with increasing proton number (Z) on the y-axis and increasing neutron number (N) on the x-axis, as shown in Fig. 1.1. The stable isotopes are displayed in black while the unstable isotopes are displayed color-coded according to their dominant decay mode. Unstable nuclei can decay via a number of processes including β-decay, electron capture, α-decay, spontaneous fission (SF), proton decay, and neutron decay. The β-decay processes convert a neutron into a proton (β^- decay) or a proton into a neutron (β^+decay and electron capture) while A remains constant and are dominant across the nuclear chart. It proceeds

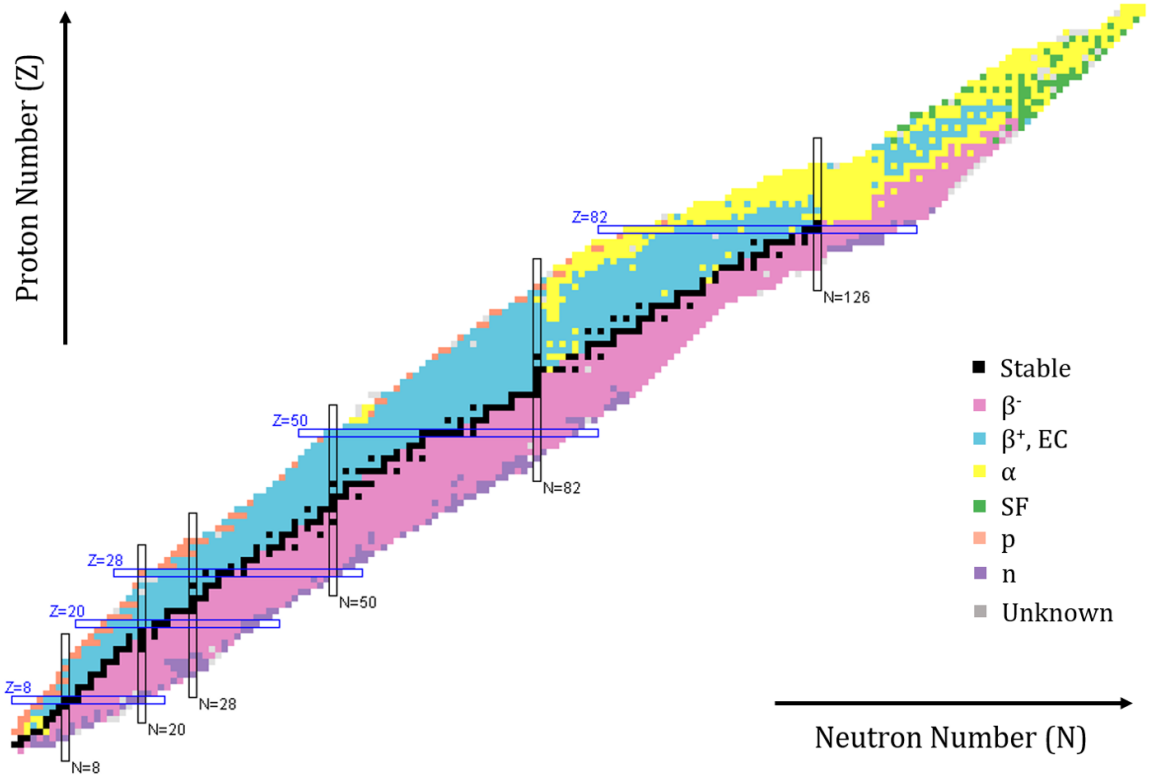

Figure 1.1: The chart of the nuclides showing increasing proton number (Z) vs. increasing neutron number (N). The isotopes shown in black are stable isotopes and the remaining isotopes are color-coded by their dominant decay process: pink for β^-, blue for β^+, yellow for α, green for spontaneous fission, salmon for proton-decay, purple for neutron-decay, and gray for unknown. Figure modified from [1].

along a chain of isotopes until it reaches the line of stability, also known as the valley of β stability. The remaining decay processes (α, SF, etc.) typically occur for large-Z isotopes or those that are farther from stability with more extreme proton-to-neutron ratios.

With approximately 3000 known isotopes and many more predicted, understanding the dynamics and interactions between protons and neutrons and how their arrangement within a particular isotope impacts its structure has become an over-arching goal in nuclear

science. The nuclear landscape is not fully described by a static description of all of the known and predicted isotopes; the nuclear properties observed in one region may differ from those in another. However, there are some general trends. Certain regions are observed to be more stable than their neighbors. These enhanced regions of stability occur at the nucleon numbers 2, 8, 20, 28, 50, 82, and 126 and are known as the nuclear magic numbers. The first hints of the magic numbers were observed in studies of the bulk properties of nuclei near the valley of stability, specifically in observables related to their masses. One such observable is the one-neutron separation energy, S_n, which is the difference in binding energy between two nuclei that differ by one neutron, i.e. $(A, Z) \rightarrow (A-1, Z)$. After the instance of a magic number, there is a steep drop in the value for S_n, which indicates additional stability. The decrease in separation energy arises from the addition of neutrons to what are known as valence 'shells', which are less bound than the closed shells at the magic numbers.

The effect of the magic numbers is seen more strongly when comparing the difference in the one-neutron separation energy between neighboring isotopes, given by

$$\Delta S_n = [BE(A, Z) - BE(A-1, Z)] - [BE(A+1, Z) - BE(A, Z)], \tag{1.1}$$

where ΔS_n is the change in the one-neutron separation energy and BE refers to the binding energy of a particular nucleus. At an instance of a magic number, ΔS_n peaks. Fig. 1.2 shows the trends for S_n and ΔS_n for even-even nuclei with $N > Z$.

The magic numbers were first mentioned by Elsasser in 1933 [3], where it was noted that isotopes with certain numbers of nucleons appeared to be more stable. Since then many theoretical studies were completed in order to reproduce the observed magic numbers. This lead to the development of the nuclear shell model which proved to be a good description for the experimental evidence of magic numbers.

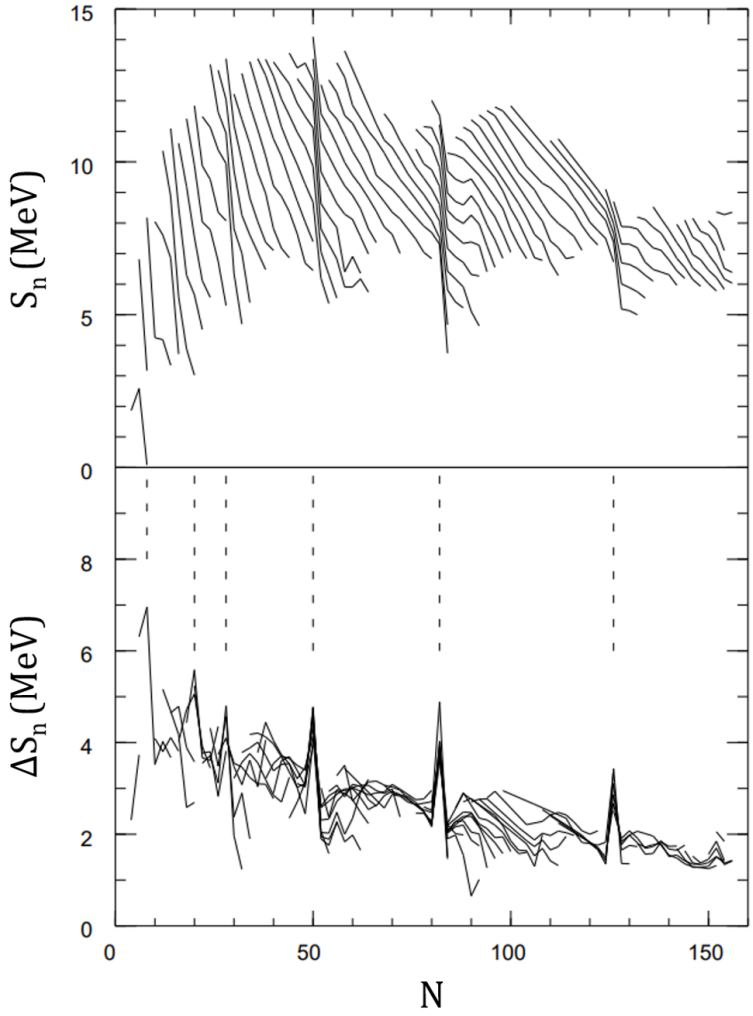

Figure 1.2: The top panel shows the one-neutron separation energy as a function of neutron number and the bottom panel shows the change in the one-neutron separation energies between neighboring isotopes as a function of neutron number. The peaks located at the magic numbers show regions of enhanced stability. Figure taken and modified from [2].

1.2 The Nuclear Shell Model

In 1948, Mayer published a shell model study that summarized the experimental evidence for a subset of the magic numbers, and prepared a shell model to explain them, but was unable to reproduce all of the observed values [4]. One year later, Mayer and the

collaboration of Haxel, Jensen, and Suess independently published studies that included a spin-orbit coupling term into their shell models and the experimental magic numbers were fully reproduced [5, 6]. Together, they provided the basis for the current nuclear shell model.

The first step in formulating the nuclear shell model is deciding which potential should be used to describe the nucleons within the nucleus. At the beginning, the harmonic oscillator (HO) and square well potentials were used but proved to be too simple and unrealistic for describing the nucleus since both go to infinity for large radii. These potentials were only able to reproduce the magic numbers up to 20.

A more realistic nuclear potential is the Woods-Saxon (WS) potential, which is flat inside the nucleus, negative such that the nucleus is bound, and goes to zero for large radii (outside the nucleus). The functional form is given by,

$$V(r) = \frac{-V_0}{1 + e^{(r-R_0)/a}}, \tag{1.2}$$

where V_0 is the depth of the potential, r is the distance from the center of the nucleus, R_0 is the mean nuclear radius, and a describes the nuclear surface diffusion. The Woods-Saxon potential alone was still unable to reproduce the observed magic numbers above 20, but inclusion of a spin-orbit term into the potential reproduced the observed gaps at the larger magic numbers. The spin-orbit force describes the interaction between orbital angular momentum and spin angular momentum and breaks the degeneracy of orbits having $\ell > 0$. The spin-orbit potential can be written as

$$V_{SO} = V_{SO}(r)\hat{\ell} \cdot \hat{s}, \tag{1.3}$$

where $\hat{\ell}$ is the orbital angular momentum and $\hat{s}$ is the nucleon spin. The shell structure for a WS potential plus the spin-orbit coupling term is shown in Fig. 1.3, where the gaps at 2, 8, 20, 28, etc. represent the closed shells at the magic numbers. As it turns out, the HO

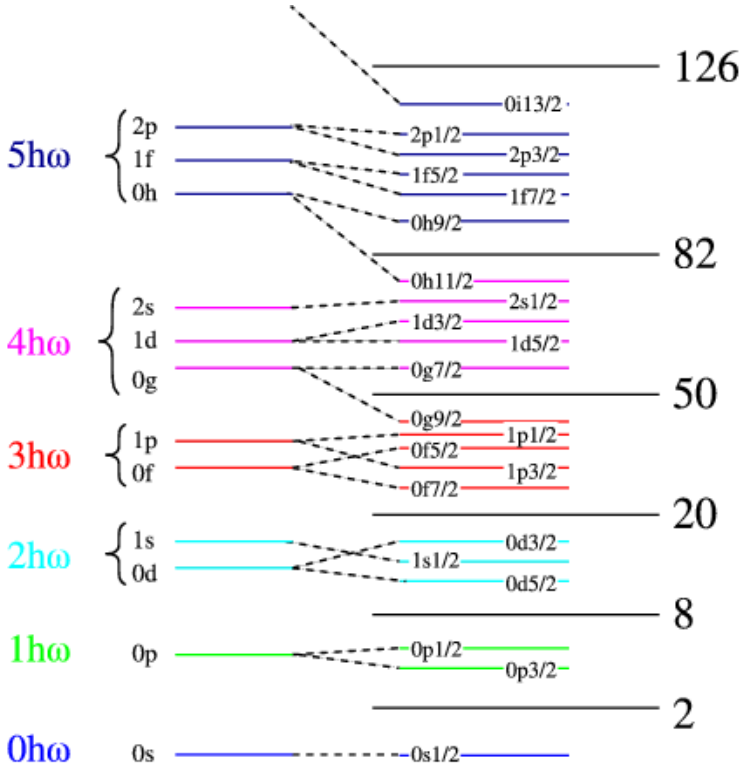

Figure 1.3: Nuclear shell structure for a WS potential with the spin-orbit coupling included. Figure modified from [7].

potential plus spin-orbit coupling also provides a reproduction of magic numbers and most often modern nuclear shell model calculations will use either a HO potential or the WS potential.

The orbitals from the shell model can be labeled as $n\ell_j$, where n is the principal quantum number (n = 0, 1, 2, 3, ...), ℓ is the orbital angular momentum quantum number (ℓ = 0, 1, 2, 3, ...), and j is the total angular momentum, $\hat{j} = \hat{\ell} + \hat{s}$, where $\hat{s}$ refers to the intrinsic spin angular momentum quantum number ($\hat{s} = \pm\frac{1}{2}$). The shells are referred to by their orbital angular momentum as the s-shell, p-shell, sd-shell, ... etc., where s, p, d, ... correspond to ℓ=0, 1, 2, ..., respectively. The energy of an orbital is referred to as the single-particle energy.

1.2.1 Single-Particle Excitations

We can often describe low-energy nuclear excitations within the shell model by treating the nucleus in terms of individual nucleons. A single-particle excitation refers to the transition of an individual nucleon from a single-particle orbital $n\ell_j$ to a higher single-particle orbital $n'\ell'_{j'}$. Nucleons successively fill the single-particle levels (see Fig. 1.3) generated by the nuclear potential and filled shells do not contribute any angular momentum to the total angular momentum. The Hamiltonian arises from the interaction of a single nucleon with the mean field generated by the remaining nucleons in the nucleus.

Single-particle models have provided a framework for understanding and predicting the structure of nuclei near closed shells. Low level excitations (near closed shells) can be thought of as excitations of individual nucleons, where the energy levels in a particular nucleus are formed by promoting a valence nucleon from its ground state orbital to a higher single-particle state. These models are valid mostly for nuclei that are a few nucleons outside of closed shells.

Take, for example, the structure in ^{209}Pb, which is one valence neutron outside of the doubly magic ^{208}Pb. Using the single-particle approach, the valence neutron would occupy the $\nu 1g_{9/2}$ orbital. The ground state of ^{209}Pb is observed to be a $\frac{9}{2}^+$, which is expected based on where the valence neutron is located [1]. The next several levels in the level scheme follow the promotion of the valence neutron into the $\nu 0i_{11/2}$, $\nu 0j_{15/2}$, $\nu 2d_{5/2}$, and so on, and the corresponding J^π for the first, second, and third excited states are $\frac{11}{2}^+$, $\frac{15}{2}^-$, and $\frac{5}{2}^+$, respectively. This is a great example of the success of single-particle models, where the observed structure arises from the promotion of single nucleons.

1.2.2 Evolution of Single-Particle Energies

While the shell model has proven to be a good description for nuclei close to stability, the question of whether or not the description holds true for nuclei far from stability has

been an area of immense experimental and theoretical effort. As experimental nuclear structure studies push beyond the valley of stability and toward the proton and neutron driplines, evidence for changing structure has become apparent and brings into question the validity of the shell model description with fixed magic numbers for exotic nuclei. In particular, in regions such as $N = 8$ for neutron-rich ^{12}Be, or $N = 20$ for the neutron-rich $_{12}$Mg isotopes, the breakdown of traditional magic numbers has been observed.

The ordering of single-particle levels has been observed to change in regions near traditional magic numbers, and experimental evidence exists showing the disappearance of traditional magic numbers and, in some cases, the appearance of new magic numbers. In regions where a closed shell is expected but is no longer present due to changes in the single-particle energy levels is known as an "Island of Inversion." Fig. 1.4 summarizes the locations of the "Islands of inversion" suggested by Ref. [8]. These regions include the major shell closures at $N = 8$ and 20, and the sub-shell closures at $N = 14$, 28, and 40. The focus of this dissertation is the "island" around $N = 20$.

1.3 N = 20 Island of Inversion

The $N = 20$ "Island of Inversion" includes the neon, sodium, and magnesium isotopes and is centered around ^{32}Mg. Studies of nuclei near the "Island of Inversion" began in 1975 with Thibault *et al.* [9], who stated that in a systematic study of Na isotopes, $^{31-32}$Na exhibited anomalies in their two neutron separation energies (S_{2n}), namely that S_{2n} increased when it was expected to continue to decrease. This anomaly in S_{2n} was attributed to deformation of the ground state, an interpretation that was supported by Hartree-Fock calculations done by Campi *et al.* [10]. Systematic studies of the $_{12}$Mg isotopes were then completed in 1983 by Détraz *et al.* [11], showing the same type of behavior with an increase in S_{2n} for $^{31-32}$Mg.

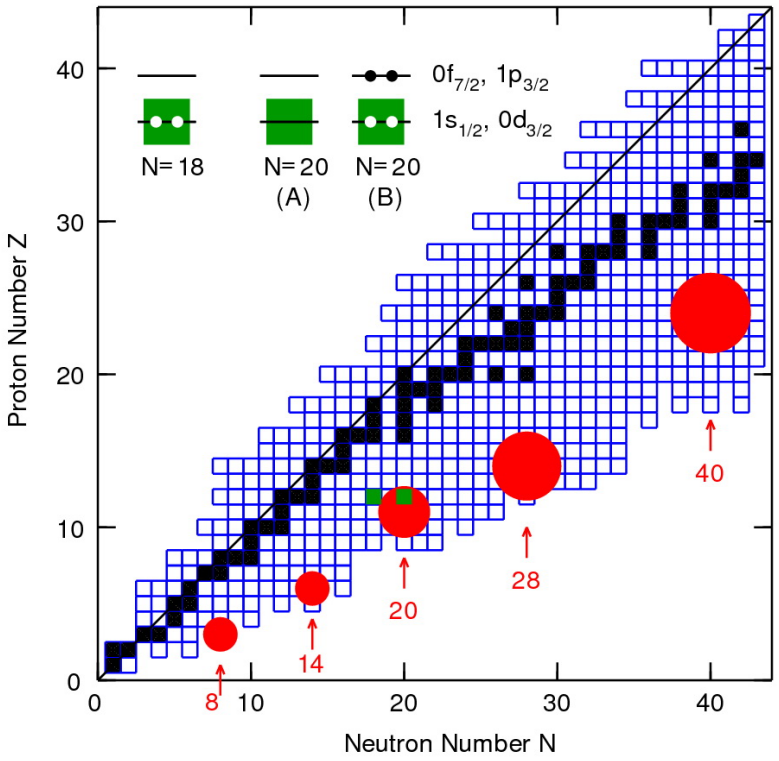

Figure 1.4: Chart of the nuclides showing the proposed "Islands of Inversion" with red circles. Figure used from Ref. [8]. The stable isotopes are shown in black and the remainder are unstable. The solid black line is showing the $N = Z$ line.

The term "Island of Inversion" was first used in 1990 by Warburton *et al.* [12], who studied mass systematics in the neutron-rich Z~8-20 region with the use of the WBMB (Warburton, Becker, Millener, Brown) potential for interpretation of the available data. Coupled with systematic studies done by Poves and Retamosa [13], the "Island of Inversion" was characterized to consist of at least nine isotopes: $^{30-32}$Ne, $^{31-33}$Na, and $^{32-34}$Mg. These isotopes are understood as having ground states that are dominated by deformation due to the vanishing of the N=20 shell gap and the dominance of intruder configurations, namely particle-hole excitations (np-nh), where n = 2, 4, 6 dominates.

These intruder configurations correspond to the promotion of pairs of neutrons from the $0d_{3/2}$ to the $0f_{7/2}$ orbital. Nuclei in and around this region exhibit lowered 2^+ energies, and large transition probabilities, B(E2: $0^+_{g.s.} \rightarrow 2^+_1$), all of which support these nuclei being deformed. The discovery of the "island of inversion" caused a shift in thinking because prior to its discovery, it was believed that the magic numbers were static for all nuclei. Studies of the shell evolution observed in these "islands of inversion" have brought into question the impact of specific aspects of the nuclear force on the shell structure of nuclei.

1.3.1 Tensor Monopole Force

One contributing factor to the evolution of shell structure with isospin is the tensor monopole force, which is part of the spin-isospin interaction between nucleons [14, 15]. The interaction arises mainly due to one-pion exchange between nucleons. This force affects the effective single-particle energies (ESPEs), which account for the mean field felt by a nucleon as a result of all other nucleons in the nucleus. The force between individual nucleons can either be attractive or repulsive depending on the angular momentum of the nucleons involved in the interaction but is maximally attractive for spin-orbit partners. The single-particle energy of a nucleon in an orbital, j, is given by its kinetic energy and the effects of the surrounding nucleons in the core. When nucleons are added to another orbital, j', the single-particle energy of the original orbital (j) may be shifted. This shift is governed, to a large extent, by the monopole component of the nucleon-nucleon interaction given by

$$V^T_{j,j'} = \frac{\Sigma_J (2J+1) \langle jj' | V | jj' \rangle_{JT}}{\Sigma_J (2J+1)}, \tag{1.4}$$

where $\langle jj' | V | jj' \rangle_{JT}$ is the two-body interaction (V) matrix element for j coupling to j' with total angular momentum J and isospin T. If the orbital angular momentum is written as ℓ and ℓ', then the total angular momentum for protons and neutrons in the two orbitals can

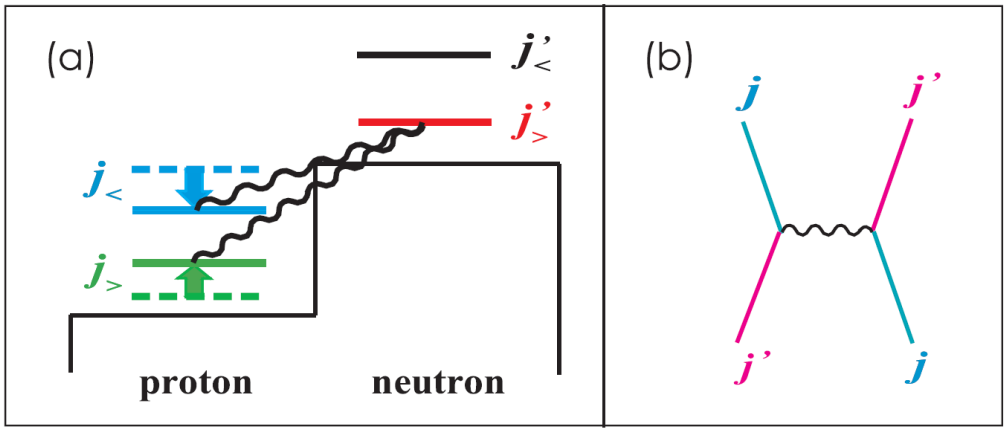

Figure 1.5: Illustration of the tensor monopole interaction between spin-orbit partners. Panel (a) shows a schematic of the monopole interaction produced by the tensor force between a proton in the $j_{>,<}$ orbital and a neutron in the $j_{>,<}$ orbitals. Panel (b) shows the pion exchange process. Figure taken from Ref. [15].

be written as $j_{>,<} = \ell \pm 1/2$ or $j'_{>,<} = \ell' \pm 1/2$. For spin-orbit partners (e.g. the proton in the $0d_{5/2}$ and the neutron in the $0d_{3/2}$ orbitals), the tensor force is maximally attractive and drives shell evolution. This process is shown schematically in Fig. 1.5.

In the region close to stability where $Z = N = 20$, or ^{40}Ca, protons fill the $\pi 0d_{5/2}$ orbital (see Fig. 1.3) and have an attractive interaction with neutrons in the $\nu 0d_{3/2}$ orbital and a repulsive interaction with neutrons in the $\nu 0f_{7/2}$ orbital. This results in a relative lowering of the $\nu 0d_{3/2}$ orbital and a raising of the $\nu 0f_{7/2}$ orbital resulting in the traditional gap at the magic number 20. However, when protons are removed from the $\pi 0d_{5/2}$ orbital and the number of neutrons is maintained, the $\pi 0d_{5/2}$-$\nu 0d_{3/2}$ attraction is weakened, and the $\nu 0d_{3/2}$ orbital moves up in energy. This energy shift causes an effective narrowing of the N=20 shell closure and n-particle-n-hole excitations become energetically favorable as pairs of particles are promoted across the narrowed gap from the $\nu 0d_{3/2}$ to the $\nu 0f_{7/2}$ orbital.

The "island of inversion" has been an immense area of study, both theoretically and experimentally, for the past three decades. While much is known about the $_{12}$Mg isotopes around $N = 20$ and it is well-established that deformed ground states are present, there are still unanswered questions about the deformation of these nuclei and their properties. The shell model describes the single-particle structure of a nucleus and does well at explaining nuclear properties based upon the behavior of individual nucleons. This representation holds true where only a few nucleons contribute, but away from closed shells, single particle structure alone may not provide the most intuitive description of the experimental evidence in the "island of inversion." Collective models are better suited to explain observed phenomena and will be the focus of the following sections.

1.4 Deformation, Collectivity, and Rotational Motion

In the late 1920s, Gamow proposed what is now known as the Liquid Drop Model (LDM), which treats the nucleus as a liquid drop, or an incompressible fluid [16]. It was the first model proposed to explain the different properties within the nucleus and to suggest that nuclei need not be spherical. In the 1930s, Bohr used the idea of the nucleus as liquid drop to describe the notion that the motion of the nucleons corresponds to fundamental modes of excitation and to further emphasize that nuclei could be non-spherical [17]. When the nuclear shell model was proposed in the late 1940s by Haxel and Mayer [5, 6], the idea of the nucleus as a liquid drop seemed contradictory to the shell model description. The shell model treats nucleons as independent particles filling orbitals and describes single-particle excitations. In contrast, the LDM describes collective phenomena where many nucleons are involved, and their properties are wholly dependent on the surrounding nucleons.

Both the LDM and the shell model are limiting cases and in 1950 J. Rainwater was able to unify these two models by considering the nucleus as a deformed liquid drop and

suggested that a non-spherical shape would allow the nucleus to rotate and that this motion would arise from the single particle motion in anisotropic orbits [18]. He explained that measurements of large quadrupole moments in nuclei could be explained by adding an average deformed potential to the spherical shell model (i.e. a deformed shell model). The mathematical formalism was completed by A. Bohr and B. Mottelson in the early 1950s [19, 20] to describe simple rotational spectra and collective properties of deformed nuclei. In 1955, S. Nilsson used the deformed shell model to describe the intrinsic shell model states under an increased deformation of the nuclear potential and showed how the single-particle orbitals changed as a function of deformation. Deformation, in this definition, can be regarded as an anisotropy that allows the system of nucleons to be treated as a single body. A system of nucleons exhibiting collective excitations is characterized by the systematic motion of a large number of nucleons. While the shell model takes a microscopic approach to describing nuclear structure via the motion of independent nucleons, collective models represent a macroscopic approach where all of the nucleons are described coherently.

1.4.1 Nilsson Model

The previous section motivated the notion that there are two limits to describe nuclear structure, single-particle and collective motion. Instead of treating the two as separate, Nilsson considered single particles moving in a deformed nuclear potential [21], resulting in the so-called Nilsson model, or the deformed shell model. Assuming that the nucleus is axially symmetric, the Nilsson model is essentially a way to specify single-particle energies as a function of deformation, where the degeneracy of each single particle state (j) is broken and the extent of "brokenness" increases as the nucleus becomes more deformed [22]. The degeneracy is 2-fold and because it's broken, the single particle states repel each other; the strength of the repulsion depends on the proximity of the states in terms of energy. The

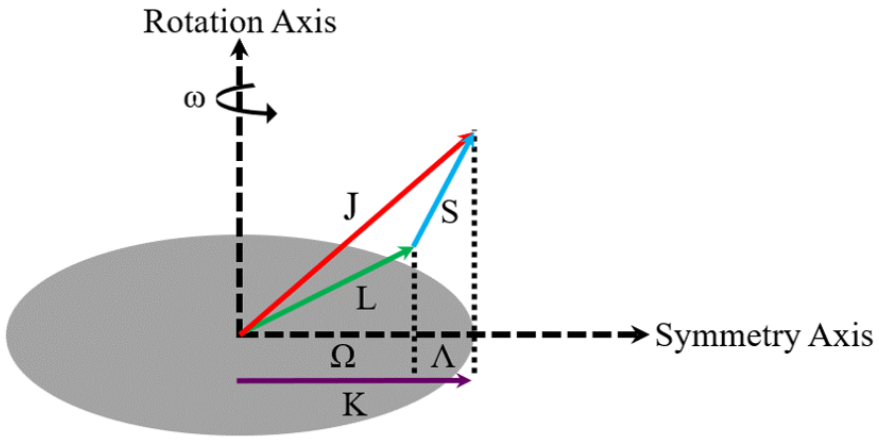

Figure 1.6: Schematic diagram showing a deformed nucleus (gray ellipsoid). The quantum numbers used to specify the system are Ω, Λ, J, L, S, and K. The nucleus rotates with angular frequency ω around the rotation axis, which is perpendicular to the symmetry axis.

Nilsson model is especially useful for deformed odd-A nuclei as it is able to describe the valence particle and coupling to the rotor.

There are several ways to quantify deformation parameters, which are β, ε, δ, or η [23]. To first order, β, ε, δ are all interchangeable with one another. For the purposes of this discussion, ε will be used, specifically ε_2, which represents the quadrupole deformation parameter. When $\varepsilon_2 = 0$, the nucleus is spherical, and the spherical shell model can be used. If $\varepsilon_2 > 0$, the nucleus has a prolate deformation, which appears as an elongated sphere like a football. In the other limit, when $\varepsilon_2 < 0$, the nucleus is oblate deformed and looks more like a pancake in shape.

The Nilsson Hamiltonian, or the deformed single-particle Hamiltonian takes the form of a deformed harmonic oscillator given by [24]

$$H_{sp} = H_0 + 2\kappa\hbar\omega[\hat{\ell}\cdot\hat{s} - \mu(\hat{\ell}^2 - <\hat{\ell}^2>)], \tag{1.5}$$

where H_0 is the deformed harmonic oscillator such that at zero deformation, it corresponds to the spherical harmonic oscillator, 2κ corresponds to the spin-orbit strength and $\kappa\mu$ to the orbital energy shift. Both κ and μ are empirical parameters found by adjusting them to data. The ℓ^2 term splits the degeneracy in each major oscillator shell, N, and the $\hat{\ell} \cdot \hat{s}$ term further splits the sub-shells into $j = \ell + s$ degenerate orbits.

In order to describe each Nilsson level, several key quantities are needed to specify the deformed system, which are shown in Fig. 1.6. The axis along which the nucleus is deformed is known as the symmetry axis. Rotation occurs with frequency ω about the rotation axis, which is perpendicular to the symmetry axis. The total angular momentum J is shown with components of the orbital angular momentum, L, and spin, S. The projection of the orbital angular momentum onto the symmetry axis is defined as Ω and the projection of S is known as Λ. The projection of the total angular momentum (J) onto the symmetry axis is given by K, where $K = \Omega + \Lambda$.

Referring to Fig. 1.6, each particular Nilsson level is specified as

$$K^{\pi}[Nn_z\Lambda], \tag{1.6}$$

where K^{π} is the projection of total angular momentum, J, on the symmetry axis, N is the major harmonic oscillator number, n_z is the z-component of N, Λ is the projection of the orbital angular momentum on the symmetry axis, and the parity is defined as $\pi = (-1)^{\ell}$. The Nilsson levels are conveniently displayed on what is known as a Nilsson diagram that shows the $K^{\pi}[Nn_z\Lambda]$ levels as a function of the quadrupole deformation, ε_2. Fig. 1.7 shows the Nilsson diagram for the potential and parameters used for interpretation in Chapter 4.

1.4.2 Rotational Model

Deformed nuclei exhibit rotational structure due to their axial symmetry, and as a consequence, the projection K on the symmetry axis is a constant of the motion and there

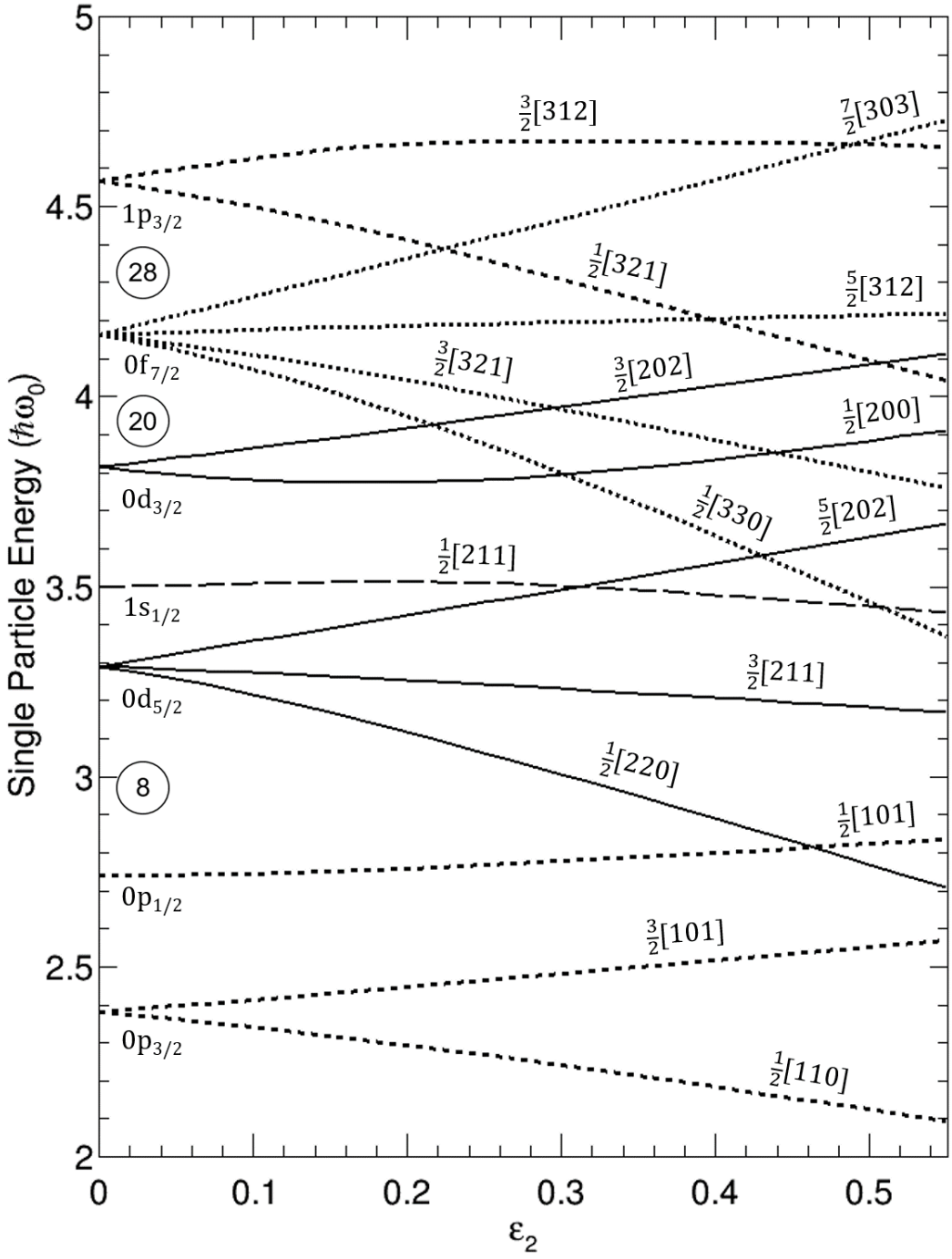

Figure 1.7: Nilsson diagram showing the orbitals up to N=28. The shell model orbitals are labeled along with their Nilsson levels.

are no rotations about the symmetry axis [22]. The quantum number K represents the angular momentum of the intrinsic system and has a fixed value for a rotational band; this is often referred to as the bandhead angular momentum. Because deformed nuclei rotate, one can determine which nuclei are deformed based upon whether or not a rotational band is present.

Additionally, rotational nuclei exhibit regularities in their energy spectra and intensity relations between transitions within a band. The rotational Hamiltonian can be written as

$$H_{rot} = \frac{\hbar^2}{2\mathscr{I}}\hat{R}^2, \tag{1.7}$$

where $\hbar$ is the reduced Planck's constant, $\mathscr{I}$ is the moment of inertia, and $\hat{R}$ is the rotational angular momentum operator. For pure rotational excitations, $\hat{R}$ is equivalent to the total angular momentum operator, $\hat{J}$. For an even-even nucleus with $K = 0$, the rotational energy, at leading order, then takes the form,

$$E_J = \frac{\hbar^2}{2\mathscr{I}}J(J+1), \tag{1.8}$$

where E_J is the level energy and J is the spin of the level. For small values of J, the rotational energy can be written as an expansion in terms of $J(J+1)$ given by

$$E_J = AJ(J+1) + BJ^2(J+1)^2 + CJ^3(J+1)^3 + ..., \tag{1.9}$$

where $A = \frac{\hbar^2}{2\mathscr{I}}$, and B, C, ... are higher order corrections to A that describe the dependence of the moment of inertia on J. The relationships shown above are valid for even-even nuclei where the corresponding values for J^π are 0^+, 2^+, 4^+, 6^+, ... and so on.

In the case of an odd-A nucleus where $K \neq 0$, the Hamiltonian for the nucleus can be written as a function of intrinsic and rotational variables as

$$H = H_{sp} + H_{coll}, \tag{1.10}$$

where H_{sp} is the deformed single-particle Nilsson Hamiltonian and H_{coll} is the Hamiltonian describing collective motion. The collective Hamiltonian has components that describe the rotational motion, the recoil, and the Coriolis coupling,

$$H_{coll} = H_{rot} + H_{cor}, \tag{1.11}$$

where H_{rot} is the rotational Hamiltonian and H_{cor} is the Hamiltonian describing the coupling between the odd particle and the collective motion of the core. The rotational Hamiltonian takes the form

$$H_{rot} = \frac{\hbar^2}{2\mathscr{I}}[(\hat{J}^2 + J_3^2) + (j_1^2 + j_2^2)], \tag{1.12}$$

where the first term represents the general form of the rotational Hamiltonian given in Eqn. 1.7 and the second term corresponds to the recoil. The rotational and recoil terms act only on the rotor. The Coriolis coupling Hamiltonian describes the coupling of the valence particle to the rotor and has the form,

$$H_{cor} = -\frac{\hbar^2}{2\mathscr{I}}(J_+ j_- + J_- j_+), \tag{1.13}$$

where $J_\pm$ and $j_\pm$ are the ladder operators for the total and single particle angular momenta, respectively. H_{cor} has matrix elements that take the form

$$\langle \Omega K | H_{cor} | \overline{\Omega K} \rangle = -\frac{\hbar^2}{2\mathscr{I}} \sqrt{(J \mp K)(J \pm \overline{K} + 1)} \times \langle \Omega | j_\pm | \overline{\Omega} \rangle \delta_{K,\overline{K}\pm 1} \delta_{\Omega,\overline{\Omega}\pm 1}. \tag{1.14}$$

For the $j_\pm$ operator, the Nilsson wave function is used to calculate the matrix elements. The total rotational energy then takes the form

$$E_{JK} = \frac{\hbar^2}{2\mathscr{I}} J(J+1) + \Delta E_{rot}, \tag{1.15}$$

where ΔE_{rot} is the additional rotational energy arising from the particle coupling to the rotating core and is given by

$$\Delta E_{rot} = (-1)^{J+K} A_{2K} \frac{(J+K)!}{(J-K)!}. \tag{1.16}$$

The term A_{2K} represents the Coriolis interaction strength and describes how the valence particle couples to the core [22] and has the form $A_{2K} = \langle K|h_{2K}|\overline{K}\rangle$, where h_{2K} is the intrinsic rotational Hamiltonian, which is given by $h_{2K} = -\frac{\hbar^2}{2\mathscr{I}} j_{\pm}$. The matrix elements for A_{2K} can then be written as

$$A_{2K} = \langle K|h_{2K}|\overline{K}\rangle = -\frac{\hbar^2}{2\mathscr{I}} \frac{\langle K|j_{\pm}|\overline{K}\rangle}{E_K - E_{\overline{K}}}. \tag{1.17}$$

The rotational energy can also be written as a power series expansion in terms of $J(J+1)$ as

$$\begin{aligned} E_{JK} = {} & AJ(J+1) + BJ^2(J+1)^2 + CJ^3(J+1)^3 + ... \\ & + (-1)^{J+K} \frac{(J+K)!}{(J-K)!} (A_{2K} + B_{2K} J(J+1) + C_{2K} J^2(J+1)^2 + ...), \end{aligned} \tag{1.18}$$

where B_{2K} and C_{2K} are higher order corrections to the Coriolis coupling term A_{2K}.

There are two coupling schemes that portray the different limits of a particle coupled to a rotor: the strong coupling limit and the decoupled limit. In the strong coupling limit, the valence particle follows the rotation of the even mass core and the Coriolis coupling is small compared to the single-particle energies. This limit usually corresponds to larger deformations. In the decoupled limit, the Coriolis force is so large that the coupling to the deformed core can be neglected and the total angular momentum and single-particle angular momentum are parallel to one another.

1.5 Experimental Techniques

In order to describe the structure of the $_{12}$Mg isotopes in the "island of inversion," several techniques have been used. This section will describe the process and selection rules for β-decay and γ-ray decay.

1.5.1 β-Decay

The β-decay process, mentioned earlier, is a weak-decay process involving the conversion of a neutron (proton) into a proton (neutron) while maintaining a constant mass number (A). There are three β-decay processes, which are outlined below:

$$\begin{aligned} \beta^- \quad &: \quad {}^A_Z X_N \rightarrow {}^A_{Z+1} Y_{N-1} + \beta^- + \overline{\nu_e} + Q_{\beta^-} \\ \beta^+ \quad &: \quad {}^A_Z X_N \rightarrow {}^A_{Z-1} Y_{N+1} + \beta^+ + \nu_e + Q_{\beta^+} \\ \text{Electron Capture} \quad &: \quad {}^A_Z X_N + e^- \rightarrow {}^A_{Z+1} Y_{N-1} + \beta^- + \overline{\nu_e} + Q_{EC}, \end{aligned} \tag{1.19}$$

where e^- is an orbital electron, $\beta^\pm$ is a beta particle (either a positron or an electron), ν_e is an electron neutrino, $\overline{\nu_e}$ is an electron anti-neutrino, and Q_{β^-}, Q_{β^+}, and Q_{EC} are the β-decay Q-values, which signify the amount of energy released in a particular β-decay and represent the difference in masses between the parent (initial) state and the daughter (final) state. When $Q > 0$, the decay is energetically possible. Neutron-rich nuclei undergo β^- decay, which converts a neutron into a proton, and a β^- particle and an anti-neutrino are emitted. The energy from the decay of a parent nucleus is shared between the daughter nucleus, the β-particle, and the anti-neutrino. The anti-neutrino emitted from the decay is undetected, but the β-decay electron can be experimentally detected since it loses energy as it passes through a material.

One important property of β-decay (or any nuclear decay process) is the decay rate, which is defined as

$$\frac{dN}{dt} = -\lambda N, \tag{1.20}$$

where λ is the decay constant and N is the number of β-decaying nuclei. For a given time, t, this quantity is given by

$$N(t) = N_0 e^{-\lambda t}, \tag{1.21}$$

where N_0 is the number of nuclei at t=0. The decay constant is related to the β-decay half-life, which is a key quantity for β-decay classifications. The half-life, $t_{1/2}$, is the amount of time needed for half of the radioactive isotope to decay, and can be expressed as

$$t_{1/2} = \frac{ln(2)}{\lambda}. \tag{1.22}$$

The β-decay process is governed by certain selection rules and the selectivity of the process and the fact that the total angular momentum must be conserved between the initial and final states, makes it a useful spectroscopic tool. The intrinsic spins of the β-particle and anti-neutrino are both $S = 1/2$. When the particles are anti-aligned, their total spin is $S = 0$ and the decay is called a Fermi decay. When the spins are parallel, the particles have total spin $s = 1$ and the decay is a Gamow-Teller decay. The change in orbital angular momentum, $\Delta\ell$, is an important quantity for classification, as is the change in parity, $\Delta\pi$, which goes as $\Delta\pi = (-1)^{\Delta\ell}$. An "allowed" decay occurs when the particles are emitted with zero orbital angular momentum ($\ell = 0$). "Forbidden" decays occur for higher values of ℓ. Although the term "forbidden" suggests that the decays will not occur, forbidden decays do occur, but with lower probability than allowed decays; the probability decreases by a factor of 10^4 for each degree of forbiddenness [25]. The selection rules for β-decay are summarized in Table 1.1.

Table 1.1: Classification of β-decay transition selection rules. Table reproduced from [25].

Transition Type	log fT	ℓ	$\Delta\pi$	Fermi ΔJ	Gamow-Teller ΔJ
Superallowed	2.9-3.7	0	No	0	0
Allowed	4.4-6.0	0	No	0	0,1
First Forbidden	6-10	1	Yes	0, 1	0, 1, 2
Second Forbidden	10-13	2	No	1, 2	1, 2, 3
Third Forbidden	>15	3	Yes	2, 3	2, 3, 4

β-decay can occur directly to more than one final state in the daughter nucleus and branching ratios can be used to compare decay rates to different states in the daughter. The decay constant, λ, is actually a sum of partial decay constants given by

$$\lambda = \sum_i \lambda_i, \tag{1.23}$$

where λ_i is the partial decay constant to a specific final state and

$$\lambda_i = BR_i\lambda, \tag{1.24}$$

where BR_i is the branching ratio to a state i. The partial half-life, T_i, can then be written as

$$T_i = \frac{ln(2)}{\lambda_i}. \tag{1.25}$$

The fT values in Table 1.1 are related to the total half-life and provide a method for comparing the β-decay probabilities. The f is the Fermi function that is related to the shape of the β spectrum and T represents the partial half-life for the decay to a specific state in the daughter. The fT values, more commonly quoted as $log(fT)$, can be used to approximately determine the level of forbiddenness in a β-decay transition. The $log(fT)$ ranges in Table 1.1 are approximate and should not be considered absolute limits.

Table 1.2: Classification of γ-ray decay selection rules for multi-polarities up to 3. Table reproduced from [25].

Radiation Type	Name	$\lambda = \Delta$J	$\Delta\pi$
E1	Electric Dipole	1	Yes
M1	Magnetic Dipole	1	No
E2	Electric Quadrupole	2	No
M2	Magnetic Quadrupole	2	Yes
E3	Electric Octupole	3	Yes
M3	Magnetic Octupole	3	No

1.5.2 γ-decay

Following β-decay or a reaction, the daughter nucleus will likely be in an excited state and will decay via γ-ray decay. The emitted γ-ray de-excites to the ground state of the nucleus through one or more intermediate transitions between states in the nucleus. These transitions have certain selection rules that require the spin and parity to be conserved. A transition from initial state, i, to final state, f, has a certain amount of angular momentum, λ, called the multipolarity. The allowed values of λ are

$$|(J_i - J_f)| \leq \lambda \leq (J_i + J_f). \tag{1.26}$$

As γ-rays have intrinsic spin of one, $\lambda = 0$ transitions are forbidden. The γ-ray decay selection rules and types are summarized in Table 1.2.

1.6 Status and Motivation

The focus of this dissertation is the study of the A=33 isobars in the N=20 "island of inversion." The bulk of the work was done on ^{33}Mg via a β-decay experiment and an

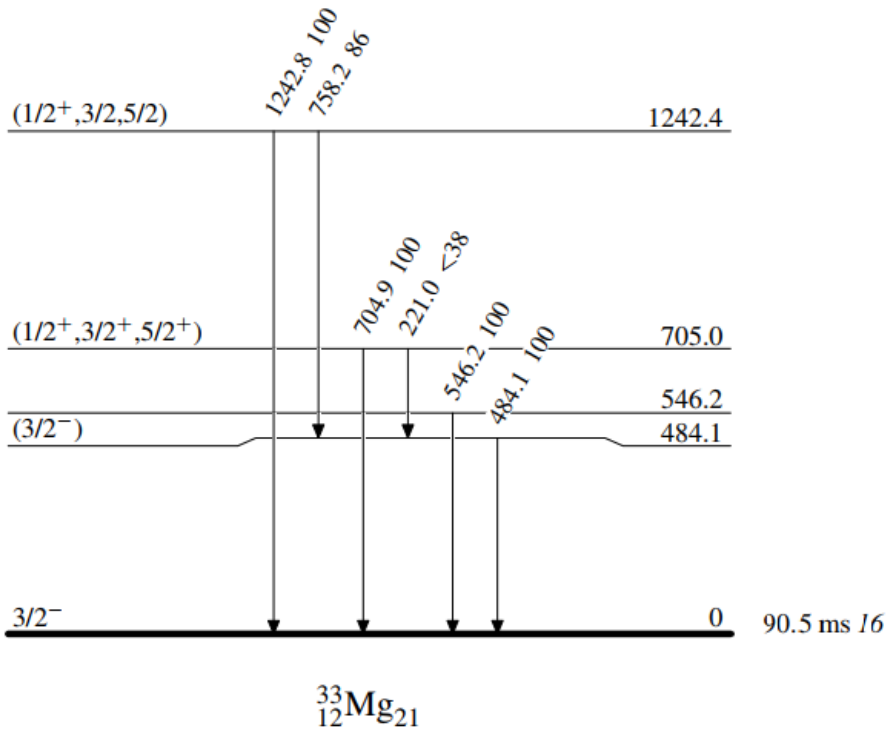

Figure 1.8: The adopted level scheme for ^{33}Mg from the literature. Figure taken from [1].

in-beam γ-ray spectroscopy experiment to populate rotational bands. A brief overview of previous measurements will be provided, followed by an overview of the current work.

The first observation of ^{33}Mg was in 1984 following a β-decay study where ^{33}Mg was identified and its half-life and several γ-ray transitions were observed [26]. In the following years, several mass and β-decay studies were completed [27–33] to obtain accurate mass (mass excess) measurements and to study the decay properties. Laser spectroscopy and nuclear magnetic resonance techniques were used to determine the magnetic moment for ^{33}Mg, which was found to be μ = -0.7456(5)μ_N [34]. A Coulomb excitation measurement of ^{33}Mg on a gold target was also completed [35] in which a $B(E2\uparrow)$ was determined.

The adopted level scheme for ^{33}Mg from the literature is shown in Fig. 1.8. The 484.1 (1) keV transition was strongly observed to de-excite to the ground state [26, 29, 35–

Table 1.3: Previously reported γ-rays in ^{33}Mg. If uncertainties are not listed, they were not given in the original paper.

Year	Reaction	Energy (keV)	Reference
1984	β-decay of ^{33}Na	484.9 (10), 546.5 (10), 704.3 (10), 1242.6(18)	[26]
2001	β-decay of ^{33}Na	221.0 (1), 297.9(1), 484.1(1), 546.2(1), 704.9(1), 758.2(1), 1242.8(2)	[29]
2002	Coulex on ^{197}Au	485 (1)	[35]
2006	^{1}H(^{33}Mg,^{33}Mgγ'),(^{34}Mg,^{33}Mgγ)	299.4 (11), 483.6 (17), 561 (17)	[37, 38]
2009	^{9}Be(^{36}Si, ^{33}Mgγ)X	490, 1250	[36]

38] establishing a 484.1 keV level. The 546.2 (1) keV transition was observed via β-decay studies to de-excite to the ground state as well [26, 29]. An additional level at 705.0 keV was placed in the level scheme with a 704.9 (1) keV γ-ray de-exciting to the ground state [26, 29] and a 221.0 (1) keV was observed to be in coincidence with the 484.1 keV g.s. transition [29]. A level at 1242.4 keV was also placed with a ground state transition at 1242.8 (2) keV and a 758.2 (1) keV being in coincidence with the 484.1 keV g.s. transition [29]. The proposed J^{π} values for the 484.1 keV, 705.0 keV, and 1242.4 keV levels are ($3/2^{-}$), ($1/2^{+}$, $3/2^{+}$, $5/2^{+}$), and ($1/2^{+}$, $3/2^{+}$, $5/2^{+}$), respectively. The 546.2 keV level has no proposed J^{π} assignment. The γ-rays from ^{33}Mg are summarized in Table 1.3.

While much is known about the γ-rays in ^{33}Mg, collective properties, such as rotational bands, have not been observed, neither for ^{33}Mg nor the other isotopes in the "island of inversion." In the even-even isotopes, such as ^{32,34}Mg, the 2^{+} state and occasionally the 4^{+} state, have been observed, but the presence of rotational band structures have not been firmly established. Without this information, the evolution of deformation in this region cannot be well understood and the need for these studies is apparent.

1.6.1 Motivation for the Current Work

The motivation for the current work was to more fully understand the structure of ^{33}Mg and its implications for the "island of inversion." In order to approach this, two experiments were performed, which will be discussed in the following chapter. The first measurement was a multi-fragmentation, in-beam γ-ray spectroscopy experiment used to study the collective nature of the $_{12}$Mg isotopes in the "island of inversion". Rotational bands are key signatures of deformed shapes and the presence of rotational structure in these isotopes would confirm their deformation and aid our understanding of the extent of deformation in the "island of inversion." The second study used β-delayed γ-ray spectroscopy to study the decay properties of ^{33}Na to ^{33}Mg and of ^{33}Mg to ^{33}Al in order to complement the work from the previous study.

1.7 Organization of Dissertation

An introduction to the concepts of single-particle structure and collective structure, as well as the interplay between the two was given in this chapter. The models used for the two measurements are discussed in this chapter along with the motivation. Details of the experimental setup and detector calibrations are presented in Chapter 2. Chapter 3 provides a discussion of the results from the NSCL experiment e14063 β-decay experiment as well as implications for the observed levels in ^{33}Mg and ^{33}Al. The results from NSCL experiment e11029 are presented in Chapter 4 along with leading order calculations in the rotational and Nilsson models. Finally, Chapter 5 includes a summary of the current work, a discussion of the implications the two measurements have on the structure of ^{33}Mg and provides some discussion of potential future studies.

2 Experimental Techniques

In order to probe neutron-rich nuclei in and around the "island of inversion", two experiments were performed at the National Superconducting Cyclotron Laboratory (NSCL) at Michigan State University. The first of these experiments, NSCL experiment e14063, investigated the β-decay of $_{10}$Ne to $_{16}$S nuclei in the $N = 20$ to $N = 28$ region by utilizing the Beta Counting System (BCS), consisting of 3 PIN detectors, a planar germanium double sided strip detector (GeDSSD), and the Segmented Germanium Array (SeGA) in the S2 vault. The second of these experiments, NSCL experiment e11029, involved prompt in-beam γ-ray spectroscopy and utilized the S800 spectrometer in the S3 vault and the Gamma-Ray Energy Tracking In-beam Nuclear Array (GRETINA). This Chapter focuses on the experimental details of these studies. Production and separation of the short-lived isotopes produced via fragmentation is discussed, along with the details of the end-station detectors, detector calibrations, and particle identification (PID).

2.1 Isotope Production

2.1.1 NSCL Overview - CCF, A1900

Primary, stable beams at the NSCL are produced in an electron cyclotron resonance (ECR) ion source. Ions are extracted from the ECR and injected into the K500 cyclotron, part of the Coupled Cyclotron Facility (CCF), which consists of the K500 and K1200 cyclotrons. Beam exits the K500 and is transported to the K1200, where it passes through a carbon stripper foil. Charge stripping produces higher charge states, which increases the charge-to-mass (Q/A) ratio of the primary beam. The maximum energy of the primary beam is proportional to the charge-to-mass ratio, and higher charge states allow the K1200 to accelerate the beam to energies on the order of 80 to 170 MeV/nucleon.

After primary beam is produced, it impinges on a production target, typically ^{9}Be with thicknesses on the order of hundreds to thousands of mg/cm^2. In this collision, the

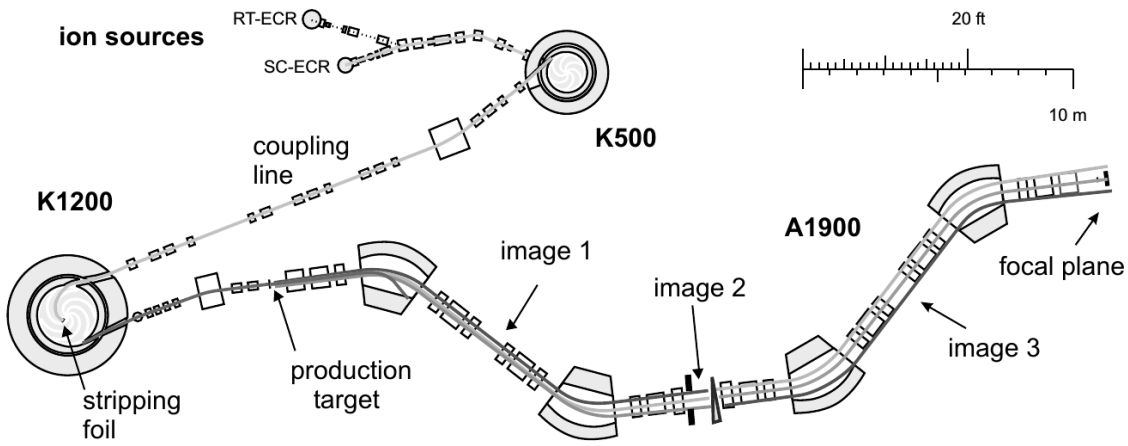

Figure 2.1: Schematic of the NSCL Coupled Cyclotron Facility, showing the K500 and K1200 cyclotrons and the A1900 fragment separator. Figure taken from [39].

projectile nucleus is broken up or 'fragments' to produce nuclei lighter than the primary beam. The fragmentation process results in a beam of radioactive nuclei, and the nuclides of interest are separated from the remaining beam fragments using the A1900 fragment separator [39, 40].

The A1900 consists of four 45° dipole magnets, multiple quadrupole magnets, and slits, all of which are used to separate the beam based upon magnetic rigidity (Bρ) and energy loss and select the desired nucleus. The A1900 consists of two separation stages. In the first stage, fragments from the production target pass through two dipole magnets and are dispersed based upon their magnetic rigidity prior to reaching the intermediate image point (image 2), shown in Figure 2.1. This process selects fragments with nearly the same Bρ, or charge-to-mass ratio. Fragments at the intermediate image are dispersed in momentum and in order to further select the isotopes of interest, the fragments pass through an aluminum wedge-shaped degrader. Energy loss through the degrader is proportional to Z^2, meaning that fragments with different numbers of protons will experience different

energy loss. This means that fragments with the same rigidity entering the wedge will have different rigidities upon exiting. The energy loss relation is given by the Bethe formula [41],

$$-\frac{dE}{dx} = \frac{4\pi e^4 Z^2}{m_0 v^2} n_{abs} z_{abs} \left(\ln \frac{2m_0 v^2}{I} - \ln\left(1 - \frac{v^2}{c^2}\right) - \frac{v^2}{c^2} \right), \tag{2.1}$$

where e and m_0 are the charge and the rest mass of the electron, Z is the atomic number of the beam particle, v is the velocity of the beam, and n_{abs}, z_{abs}, and I are the number density, atomic number, and ionization potential of the wedge material, respectively.

In the second stage of separation, the fragments are further dispersed based upon their Bρ values after exiting the wedge degrader. To isolate the fragment of interest, adjustable slits are located at each image and can be adjusted to vary the momentum acceptance (Δp/p) of the separator up to a maximum of 5%. The rate and purity of the secondary beam are determined based upon the type of production target and wedge degrader that are used, as well as the slit settings. The A1900 can accommodate experiments that utilize a cocktail beam, or a very selective, pure beam. Following the A1900, the secondary beam is then delivered to the target area.

2.1.2 Overview of NSCL Experiments

For both NSCL experiments e14063 and e11029, a ^{48}Ca primary beam was used. Upon exiting the K500, the beam was at an 8^+ charge state and an energy of 12.23 MeV/nucleon. The primary beam underwent charge stripping to a 20^+ charge state and was accelerated through the K1200 to 140 MeV/nucleon. Upon exiting the K1200, the primary beam fragmented on a ^{9}Be target. In the case of NSCL experiment e14063, which was conducted in March 2015, the production target had a thickness of 775 mg/cm^2 and the resulting beam was a cocktail secondary beam of neutron-rich Ne, Na, Mg, Al, Si, S, and P isotopes, centered on ^{36}Mg. The cocktail was transported through the A1900 using the full 5% momentum acceptance (Δp/p) with an aluminum wedge degrader thickness

of 300 mg/cm^2 and delivered to the Beta Counting Station (BCS) located in the S2 vault. NSCL experiment e11029 took place in June 2013 and utilized an 846 mg/cm^2 ^{9}Be target to produce a secondary beam of ^{46}Ar. Secondary fragments were separated through the A1900 with a momentum acceptance of 1% with a 300 mg/cm^2 aluminum wedge degrader, with greater than 95% purity and an energy of 102 MeV/nucleon and transported to the S800 Spectrograph in the S3 vault. Further details about the end-station detectors, calibrations, and particle identification (PID) will be discussed in the following sections.

2.2 E14063 - S2 Vault

This section will describe the experimental setup for the e14063 experiment. To begin, an overview of the experiment is given followed by a discussion of the detector suite. In each subsection, the detectors, electronics, readout, and calibrations are discussed.

2.2.1 Detector Overview

The detector suite in the NSCL Beta Counting System, setup in the S2 vault, consisted of a Germanium Double Sided Strip detector (GeDSSD), described in Section 2.2.3, surrounded by sixteen detectors from the Segmented Germanium Array (SeGA), described in Section 2.2.4. The SeGA detectors were placed around the GeDSSD with eight detectors on each side. Upstream from the GeDSSD was a set of three silicon PIN detectors, also described in Section 2.2.3. Figures 2.2 and 2.3 show a schematic and photograph, respectively, of the experimental setup at the time of the experiment.

Incoming ions from the fragmentation of the primary beam implanted into the GeDSSD, where they stopped and then subsequently decayed. The implant and decay events were detected in the GeDSSD. γ-rays, either prompt or beta-delayed, were detected in the SeGA array, and the Si PIN detectors were used for time-of-flight and energy loss information. The following sections will describe the detectors of the BCS, the electronics

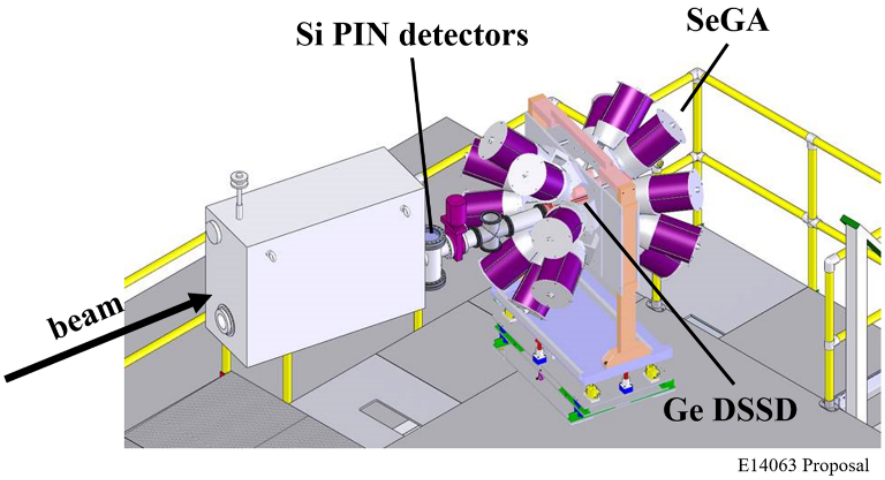

Figure 2.2: Engineering layout of the S2 vault target area showing the location of the PIN detectors, DSSD, and SeGA configuration.

and readout for the experiment, and the calibrations required in order to analyze the decay of ^{32}Na, ^{33}Na, and ^{33}Mg.

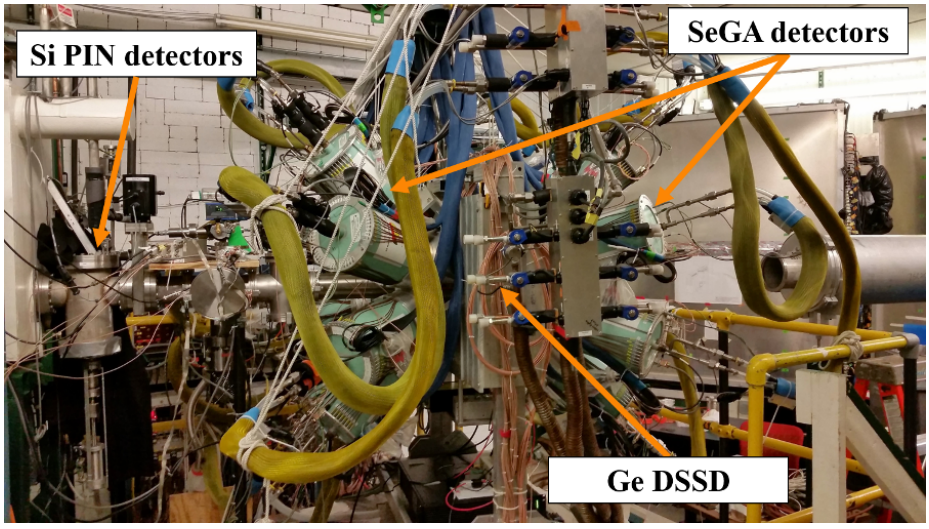

Figure 2.3: Photograph of the experimental setup showing the location of the 3 Si PIN detectors, the GeDSSD, and SeGA.

2.2.2 NSCL Digital Data Acquisition System (DDAS)

For this experiment, the detector signals were read out using the NSCL Digital Data Acquisition System (DDAS) [42, 43]. DDAS was originally designed to be used in conjunction with SeGA but has since been updated and expanded to be used for a wide variety of detector arrays, including the BCS. DDAS is a modular system comprised of Pixie-16 modules manufactured by XIA LLC. The benefit of using DDAS over analog systems is that the energy resolution is better than traditional analog electronic systems, the acquisition deadtime is nearly zero, lower energy thresholds can be set, the dynamic range is much larger, and perhaps more importantly, the digitized signals from the Pixie modules can be recorded for offline pulse-shape analysis.

2.2.3 β Counting System

The central detector in the BCS is the GeDSSD, which is a 1-cm-thick, 9-cm-diameter high purity germanium crystal that is electronically segmented into sixteen 5 mm strips on each face, sixteen vertical strips on the front and sixteen horizontal strips on the back, creating 256 pixels in total. Each strip was readout through a low-gain and a high-gain pre-amplifier in order to detect both implant and β-decay events. The low-gain pre-amplifier was used for detecting implant events with energies up to 30 GeV, while the high-gain pre-amplifier, with a range of 0 to 15 MeV, is better suited for the detection of β-decay events [44]. The implantation rate in the detector was approximately 100 Hz, which was limited due to the exotic secondary beam setting. Fragments were continuously implanted in the detector during a data run, but the highly segmented nature of the GeDSSD allowed each implantation event to be correlated with its subsequent β-decays on an event-by-event basis. A schematic representation of the implant and decay process is shown in Fig. 2.4.

Upstream from the GeDSSD were three silicon PIN detectors, which consist of an intrinsic semiconductor (I) sandwiched between a p-type (P) and a n-type (N)

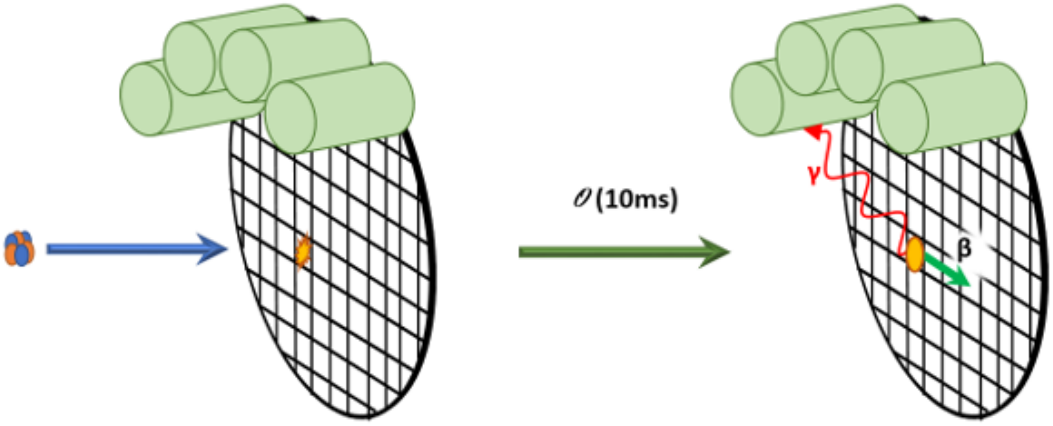

Figure 2.4: Fragments implant into a pixel of the GeDSSD and after a certain amount of time (on the order of 10 ms), the implants decay and de-excite via γ-rays. The decays are detected in the GeDSSD while γ-rays are detected in SeGA, which is depicted with green cylinders.

semiconductor [41].The thicknesses of the detectors was 500 μm for PIN01, 500 μm for PIN02, and 300 μm for PIN03. The first two PIN detectors served as TOF stop signal relative to the TOF start signal from the plastic scintillator at image 2 of the A1900 and for energy loss information used for particle identification (PIN01, PIN02). The third PIN detector was used to veto light particles (PIN03) such as protons and α-particles.

2.2.3.1 Electronics

Signals from the 32 strips of the GeDSSD were input into four Pixie-16 modules and were recorded with DDAS. The four were arranged to correspond to the front low-gain, front high-gain, back low-gain, and back high-gain. Readout of the GeDSSD required an energy signal on both the front and back strips of the detector. Thresholds were set on each strip and when a signal above that threshold occurred on the front and the back, the event was taken as either an implant or a decay, based upon the energy deposited. The time and

Table 2.1: Summary of the TAC settings for the e14063 experiment.

TAC#	Start	Stop
1	image 2 north scintillator	image 2 south scintillator
2	PIN01	image 2 north scintillator
3	PIN01	image 2 south scintillator
4	PIN01	cyclotron RF
5	PIN02	image 2 north scintillator

energy for each event was read out when the triggering condition was met. The triggering condition for an event to be identified as an implant was a front-back coincidence in the low-gain pre-amplifier signals. Likewise, a decay event required a front-back coincidence in the high-gain pre-amplifier signals. Signal traces were recorded for a portion of the e14063 data but were not analyzed in this work. Details about the software correlation of implant and decay events is presented in Section 2.2.5.

Each silicon PIN detector had both energy and time signals. The energy signal from the PIN detectors was input into the Pixie-16 modules. The timing signal went into a Tennelec 241S fast-timing amplifier. PIN01 and PIN02 had lower gain settings than PIN03 since the latter was used as a veto and the former were used for implant energy and timing signals. After amplification, the signals were input in a Canberra 454 Quad Constant Fraction Discriminator (CFD) and then delayed by 100 ns. The output signal went to an ORTEC 566 Time-to-Amplitude Converter (TAC). A total of five TACs were used for timing measurements, where four of the five measured the time-of-flight of the

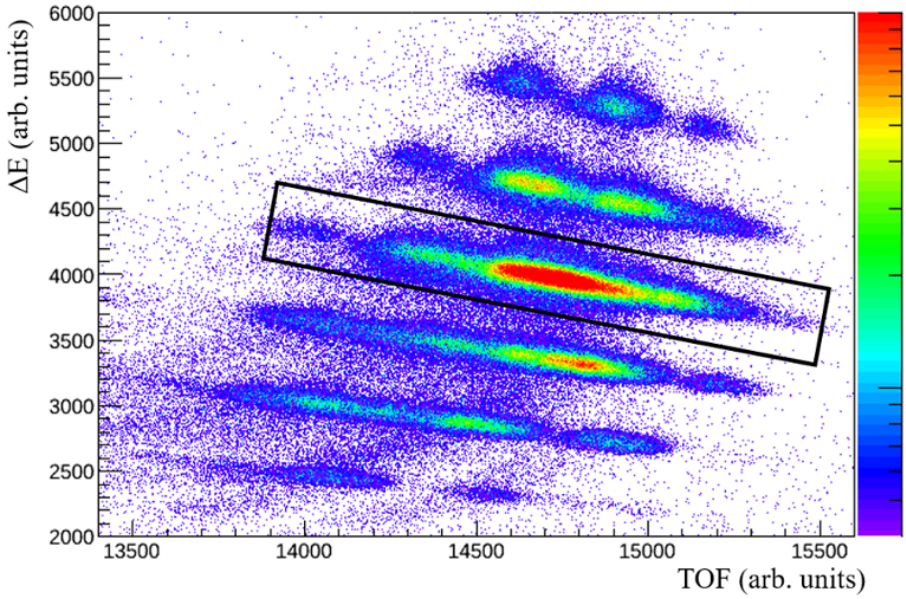

Figure 2.5: The PID prior to TOF and ΔE corrections. Each semi-horizontal band represents an isotopic chain, but no clear separation of isotopes within each chain is visible.

beam fragments. Table 2.1 summarizes the TAC settings for this experiment. The output signals from each of the five TACs were readout by Pixie-16 modules.

2.2.3.2 Calibrations

As described in Section 2.2.3, the silicon PIN detectors were used for time-of-flight and energy loss (ΔE) information, which was used to identify the incoming fragments. The energy loss of fragments traveling through one of the PIN detectors is proportional to Z^2 and the time-of-flight is proportional to A. In order to measure the time-of-flight, two detectors separated by some distance are required. In this case, the plastic scintillator at the dispersive image (I2) of the A1900 and one of the first two PIN (PIN01, PIN02) detectors was used. The scintillator located at image 2 is a position sensitive thin plastic scintillator with photo-multiplier tubes (PMTs) coupled to each end, which are denoted as north or

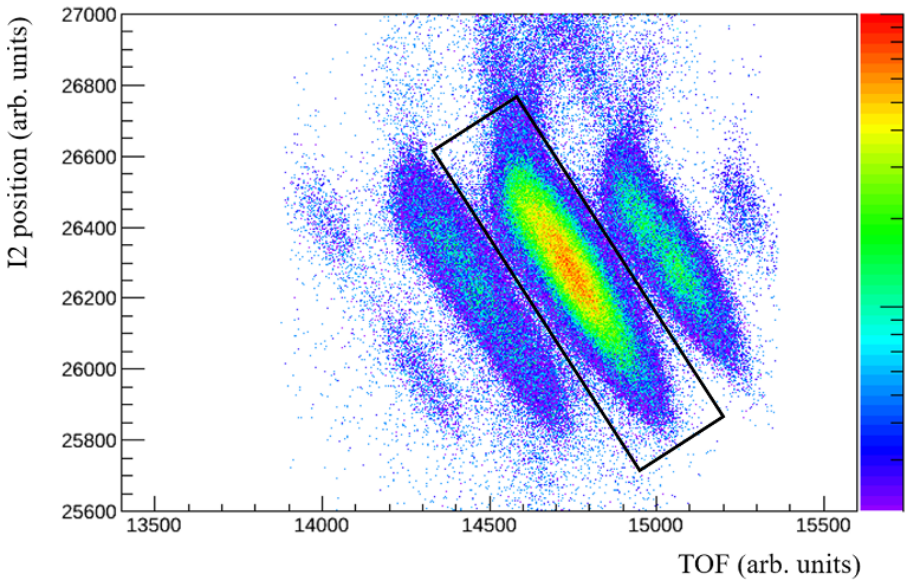

Figure 2.6: The position along the I2 scintillator vs. time-of-flight for a gate on one of the bands in Fig. 2.5. The gate drawn in the current figure is used for the next stage in the time-of-flight corrections.

south. Fragments passing through image 2 are dispersed and will have a different position in the I2 scintillator based upon their magnetic rigidity. The time-of-flight measurement uses the signal from PIN01 as the start and the delayed I2 plastic scintillator signal (see Fig. 2.1) as the stop. Plotting ΔE vs. TOF yields isotopic information about the fragments in the experiment. However, because the momentum acceptance of the A1900 was so large (5%), the time-of-flight for each mass varied substantially. The overlapping momentum distributions for each isotope were smeared together in the time-of-flight so that clear isotopic separation was not available without a momentum correction to the time-of-flight and energy loss measurements.

Since the I2 scintillator is read out by two PMTs, which are located on either end of the plastic, the position of a fragment passing through the plastic can be determined from

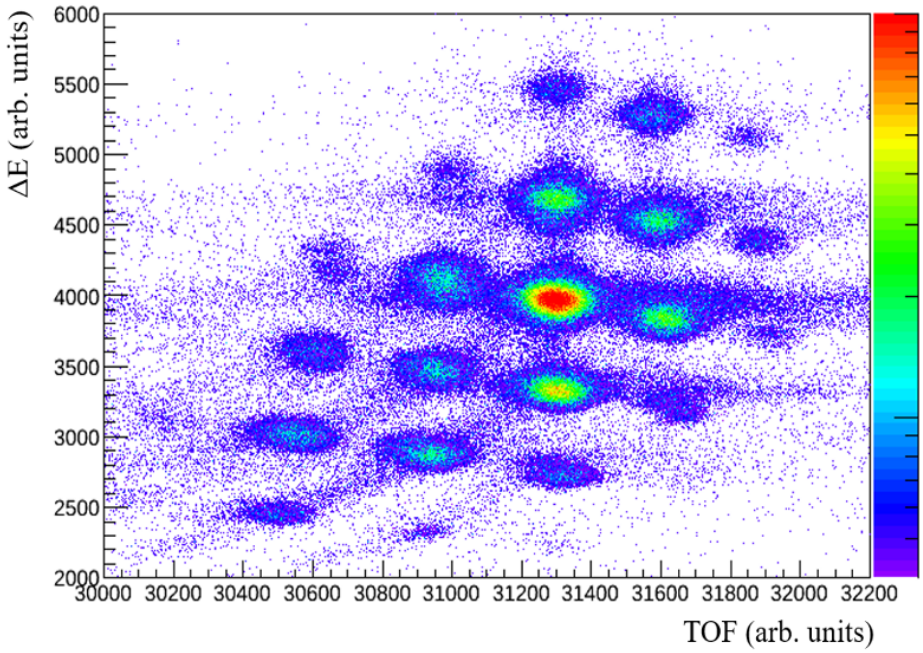

Figure 2.7: The updated PID following the time-of-flight correction. Clear separation between isotopes is now shown.

the difference in the timing signals between the north PMT and the south PMT. Position information is used to correct for the momentum dependence of the time-of-flight and energy loss because it takes into account the different distances the fragments travel and the velocity of the fragments. The PID prior to TOF and ΔE corrections is shown in Fig. 2.5. Each band corresponds to a single Z, but isotopic separation is not visible. The correction to the time-of-flight utilized a gate (shown in Fig. 2.5) on one of the isotopic chains, then using that gate, the distribution of isotopes within the Z band can be seen by plotting the position along the I2 scintillator versus the time-of-flight. Fig. 2.6 shows the I2 position of the isotopes within the gate drawn in Fig. 2.5. Each band in Fig. 2.6 corresponds to a different isotope having the same Z. To produce clear separation between isotopes in the PID, the slope of the bands was corrected to make them vertical such that each band

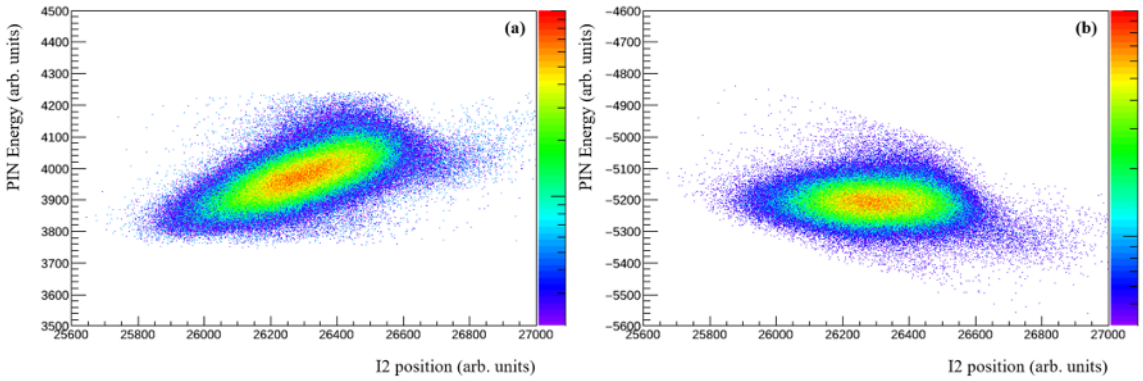

Figure 2.8: The PIN energy vs. position along the I2 scintillator for a gate on the most intense isotope in Fig. 2.7 before (a) and after (b) corrections.

had approximately a single time-of-flight. In practice, a gate was drawn around the most intense band in Fig. 2.6 and the slope of the isotope band was extracted from a linear fit. The time-of-flight was corrected using

$$TOF_{corrected} = TOF_{uncorrected} + 0.63 \times I2_{position}, \tag{2.2}$$

where $\mathrm{TOF}_{corrected}$ and $\mathrm{TOF}_{uncorrected}$ are the corrected and raw TOF values from PIN01 to the scintillator at I2, 0.63 is the slope of the isotope band from Fig. 2.6, and the $\mathrm{I2}_{position}$ is the position of the isotope in the I2 scintillator. The resulting PID is shown in Fig. 2.7 and is vastly improved from Fig. 2.5.

In addition to the time-of-flight correction, the energy loss was also corrected to account for the velocity dependence of the ΔE signal. Starting with the TOF corrected PID, a gate was placed around the most intense isotope. The PIN01 energy is plotted with respect to the isotope position in the I2 scintillator and because the gated isotope has some velocity dependence, it does not appear horizontally. This is shown in Fig. 2.8(a). Much like with the TOF correction, the distribution for the single isotope is fit to a line and the slope of the line is applied as a correction to the PIN01 energy using

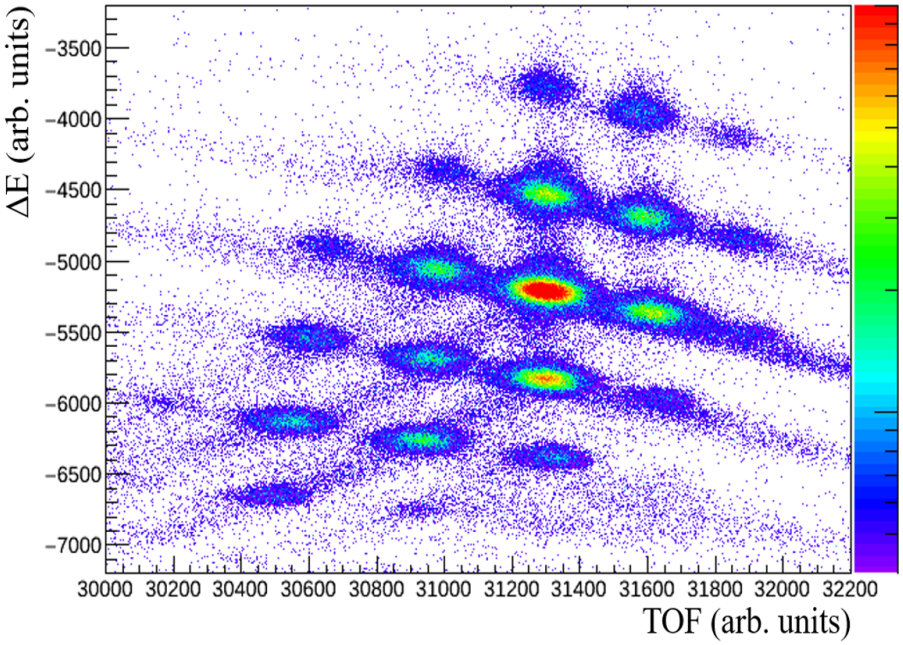

Figure 2.9: The PID from the E14063 experiment after time-of-flight and energy-loss corrections were completed.

$$PIN01_{corrected} = PIN01_{uncorrected} - 0.35 \times I2_{position}, \tag{2.3}$$

where $\mathrm{PIN01}_{corrected}$ and $\mathrm{PIN01}_{uncorrected}$ are the corrected and raw PIN01 energy values, -0.35 is the slope of the isotope gate from Fig. 2.8, and the $\mathrm{I2}_{position}$ is the position of the isotope in the I2 scintillator. Fig. 2.8(b) shows the PIN energy vs. TOF for the gated isotope after correcting the velocity dependence of the energy loss. The full PID for the e14063 experiment is shown in Fig. 2.9 after all of the corrections were applied.

2.2.4 Segmented Germanium Array (SeGA)

Prompt, isomeric, and β-delayed γ-rays were detected in the Segmented Germanium Array (SeGA) [45], which surrounded the GeDSSD in two rings of eight detectors each,

or the “betaSeGA” configuration. Each SeGA detector consists of a single HPGe crystal that is electronically segmented into 32 components. The segmentation, however, was not utilized for this measurement due to the fact that the implants stopped in the GeDSSD and Doppler correction was not required. The following two sections will describe the SeGA electronics, readout, and calibration.

2.2.4.1 Electronics

Each of the 32 segments has its own electronic readout in addition to a central contact readout that records the total energy deposited in the detector. However, for this experiment only the central contact of each of the sixteen detectors was read out. The central contact signal for each detector was input into a Pixie-16 module and read out by DDAS. SeGA readout was self-triggered and all energy signals above threshold were recorded with a timestamp.

2.2.4.2 Calibrations

Energy calibration runs were performed at the beginning of the experiment using a NIST-calibrated standard reference material (SRM) source, which is primarily composed of ^{125}Sb, ^{154}Eu, and ^{155}Eu. Fig. 2.10 shows γ-rays from the SRM source identified and labeled with their respective energies. For each SeGA detector, all of the peaks identified in Fig. 2.10 were fit using a Gaussian plus a linear background. The peak positions were compared to their literature values and a quadratic fit was performed on the channel vs. energy data. Of the 84 data runs in this experiment, runs 16-17 were SRM runs and were used for the calibration. An energy residual is the difference between the literature value for the peaks in the SRM source minus the fit values for the peaks after the calibration is applied. The residuals for all sixteen detectors for the calibration runs are shown in Fig. 2.11. The residuals obtained for each detector are less than ±0.4 keV, which is used as the error on the energy calibration. The error associated with the γ-ray energies for the

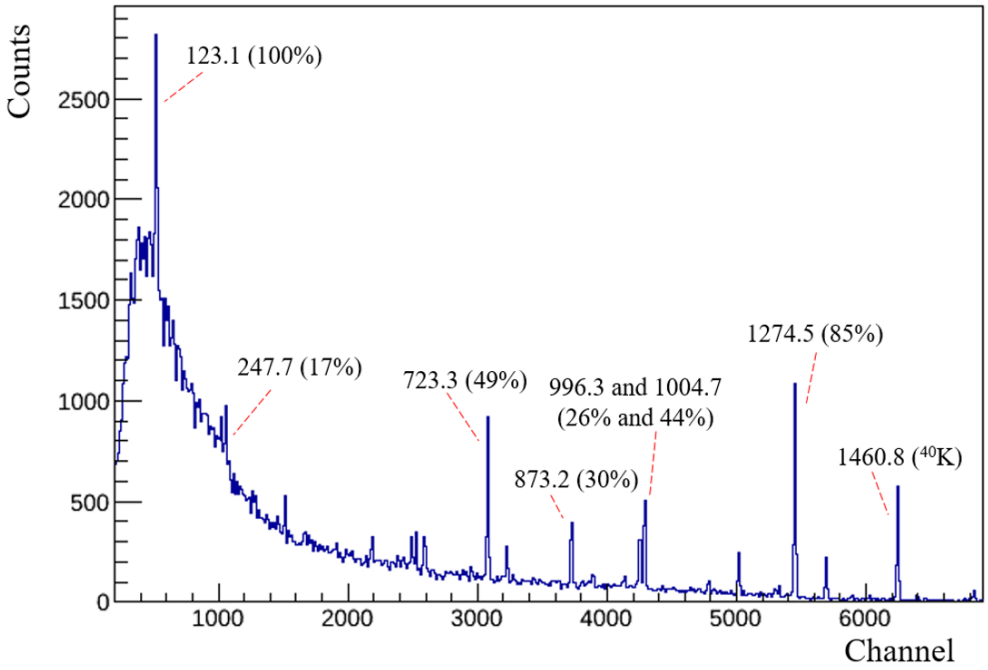

Figure 2.10: The identified γ-ray peaks in the SRM source in SeGA module #12.

e14063 experiment was determined using the error on the calibration added in quadrature with the error in the centroid of the peak.

As the calibration runs were performed at the beginning of the experiment, it was necessary to check the gain stability of SeGA throughout the experiment. This was done by fitting the 511 keV and 1460 keV background transition with a Gaussian plus a linear background for several runs throughout the experiment. The energy, FWHM, and resolution remained consistent throughout the experiment and Table 2.2 summarizes the energy calibration and resolution stability for the SeGA array.

The energy calibration for the SeGA detectors was required in order to extract accurate energies for the γ-rays coming from the nuclei of interest. The efficiency of the array was also needed in order to extract both the absolute and relative intensities of the γ-ray transitions. The efficiency used in the current work was taken from Ref. [46], and

Table 2.2: Resolution of the 511 keV and 1460 keV peaks for random runs throughout the experiment.

Run#	E_γ (keV)	σ (keV)	FWHM (keV)	Resolution (%)
16-17	510.9	1.6	3.7	0.7
36	510.7	1.5	3.6	0.7
41	510.8	1.5	3.4	0.7
50	510.7	1.5	3.6	0.7
58	510.9	1.6	3.8	0.7
63	510.8	1.6	3.8	0.7
71	510.5	1.6	3.8	0.7
77	510.9	1.7	3.9	0.8
80	511.1	1.6	3.8	0.7
83	511.2	1.6	3.8	0.7
ALL	510.7	1.6	3.9	0.8
16-17	1460.1	1.4	3.4	0.2
36	1459.6	1.4	3.4	0.2
41	1459.8	1.4	3.4	0.2
50	1459.7	1.4	3.3	0.2
58	1460.1	1.4	3.4	0.2
63	1459.8	1.4	3.4	0.2
71	1459.0	1.5	3.5	0.2
77	1459.9	1.5	3.6	0.2
80	1460.4	1.5	3.6	0.2
83	1460.8	1.5	3.5	0.2
ALL	1459.6	1.6	3.7	0.3

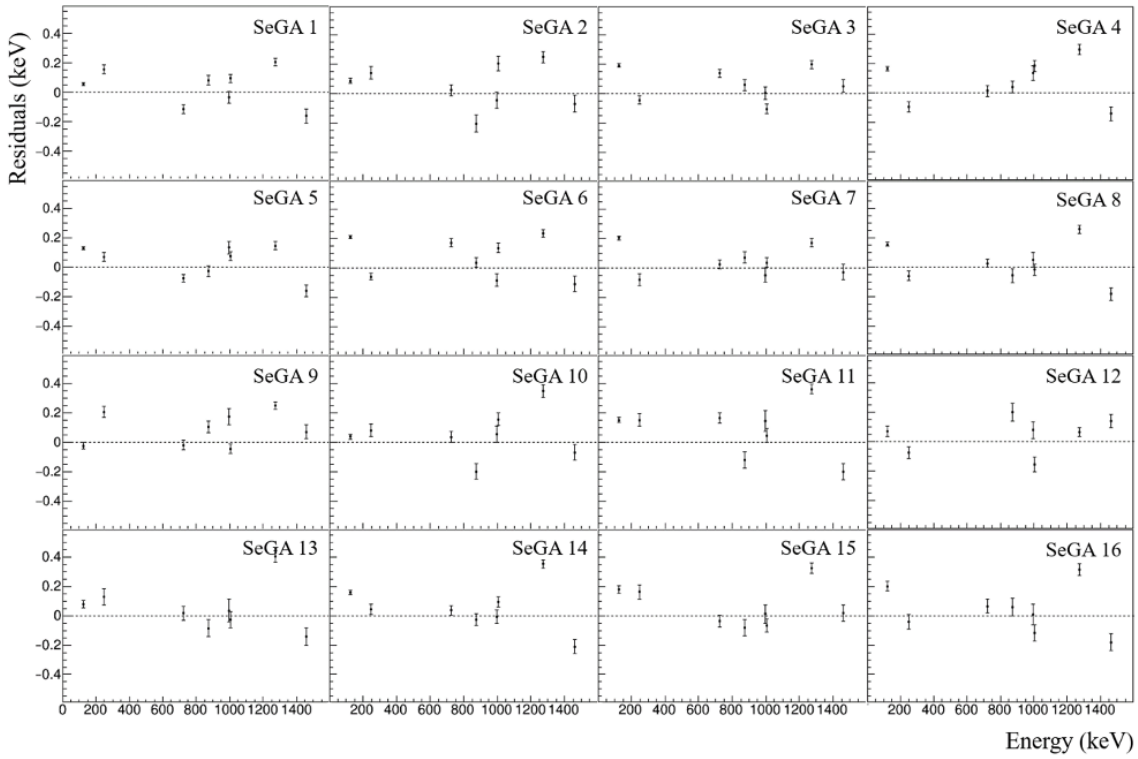

Figure 2.11: The energy residuals from the calibration of SeGA using the SRM source.

is summarized here. The same SRM source was used for the efficiency calibration and was placed at different locations relative to the SeGA array and GeDSSD, such as between the two rings of the SeGA detectors. The lines in the SRM source were fit in the range of 42 keV to 1597 keV for each source position and since the SRM source is NIST-calibrated, the absolute efficiencies were determined. A GEANT4 simulation of the detector suite was made and run using γ-ray from transitions in the SRM source as the input. The SRM transitions were simulated at each source position and the results from the simulation and experiment were then compared. Agreement between the two suggested that the detectors were all modeled correctly in the simulation. The validated simulation was then used to obtain the absolute γ-ray efficiencies for a source in the middle of the GeDSSD, which is

where the majority of the implants would be located. The efficiency for the array can be described as a sixth order polynomial of the form,

$$\epsilon[E_\gamma](\%) = 100 \times 10^{a(x)^6+b(x)^5+c(x)^4+d(x)^3+e(x)^2+f(x)+g}, \tag{2.4}$$

where a, b, c, d, e, f, and g are constants and $x = log_{10}(E_\gamma)$. The values for the constants are -0.23, 4.2, -32.8, 135.3, -312.9, 383.9, and -196.0, respectively. A 5% uncertainty was assigned to all efficiency values regardless of energy, which is representative of discrepancies between the simulation and physical setup. Fig. 2.12 shows the log-log efficiency curve used for the current work based upon Eqn. 2.4 and the constants listed above. For further details of the GEANT4 simulation and efficiency determination, see Ref. [46].

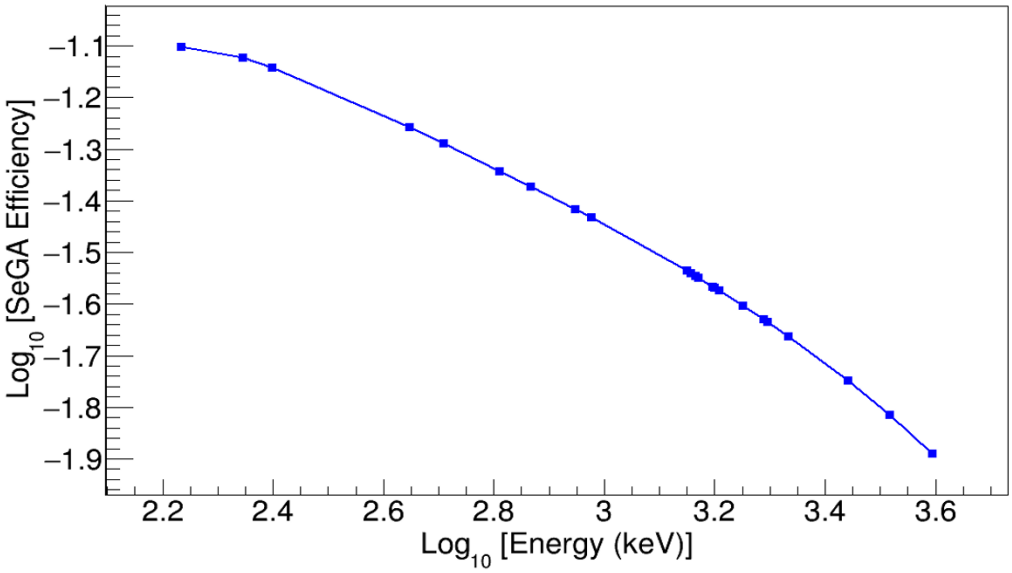

Figure 2.12: The efficiency curve the for SeGA array from the method described in Ref. [46].

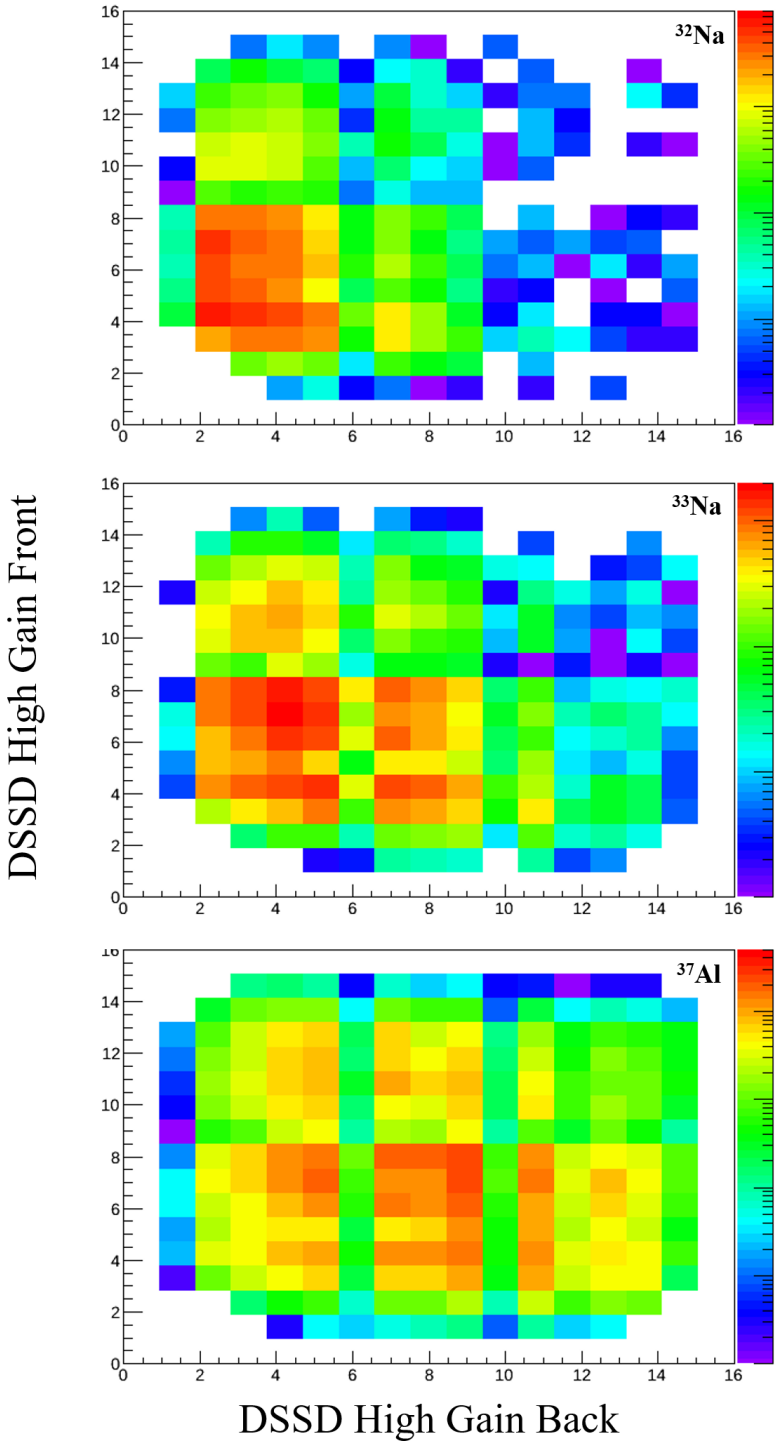

Figure 2.13: The DSSD decay distribution for the decay of ^{32}Na, ^{33}Na, and ^{37}Al.

2.2.5 Implant-Decay Correlations

Beam fragments were continuously implanted into the GeDSSD and because of this, β-decay spectroscopy techniques need a reliable method for correlating implantation events with their subsequent β-decays. The correlation method makes use of both position and time information.

An event was identified as an implant when there was a valid signal in the two upstream PIN detectors (PIN01, PIN02) and a low-gain signal on at least one strip on both the front and back of the GeDSSD. Implant events also required the absence of signals in PIN03 and the high-gain GeDSSD signals. The pixel with the maximum energy deposited on the front and back was identified as the location of the implantation. An event was defined as a decay when a high-gain signal was detected on at least one strip of the front and back of the GeDSSD and no other signals from the PIN detectors or the low-gain strip signals of the GeDSSD were detected. The distributions of ^{32}Na, ^{33}Na, and ^{37}Al decays are shown in Fig. 2.13 to provide an idea of how the decays (and thus implants) are spread out in the 256 pixels of the GeDSSD.

Once an event was identified as a decay, both time and position information were checked to correlate the decay with the appropriate implant event. The position of the decay was checked to determine when the last implantation event occurred within that pixel. The correlation position search included the decay pixel and the eight nearest neighbors. If an implant had occurred one of the nearest neighbors, then the pixel was checked to see if back-to-back implants had occurred in the pixel within a short time. After the implant pixel was determined and the correlation position check was satisfied, the time between the implant and decay was checked to see if the event had occurred within a pre-defined window known as the correlation time. The correlation time was set for each isotope by taking some multiple of the half-life (usually 2 or 3 times the half-life). After

satisfying both the time and position checks, the decay was correlated with the appropriate implantation event.

2.3 E11029 - S3 Vault

This section will describe the experimental setup for the e111029 experiment. To begin, an overview of the experiment is given followed by a discussion of the detector suite. In each subsection, the electronics, readout, and calibrations are discussed.

2.3.1 Overview

In the second experiment discussed in this Chapter, a secondary ^{46}Ar beam was delivered to the S3 vault and impinged on a 267 mg/cm^2 ^{9}Be target located at the target position of the S800 spectrograph [47, 48] where it fragmented a second time. The fragments were identified on an ion-by-ion basis in the focal plane of the S800 and the emitted γ-rays were detected in GRETINA. The S800 is a high-resolution, high-acceptance magnetic spectrograph consisting of an analysis line and the spectrograph itself. The analysis line, which starts at the object (located downstream of the A1900) and ends at the S800 target location (see Figure 2.14), focuses the incoming secondary beam on the reaction target, located at the S800 target location. The analysis line has two modes: focused mode and dispersion-matching mode; in this experiment focused mode was used. In focused mode, the analysis line and reaction target are achromatic, which causes the beam to be spread-out, or dispersed (chromatic) in the focal plane along the x-direction. This mode has a momentum acceptance of ±2% for the incoming beam and fragments must be tracked from the S800 target to the focal plane in order to recover the energy resolution lost due to momentum spread. This mode provides the highest acceptance [47].

The reaction recoils were detected in the S800 focal plane detector suite [48], which provides particle identification (PID) and trajectory information, to identify reaction recoils. The focal plane detector suite utilizes two cathode readout drift chambers

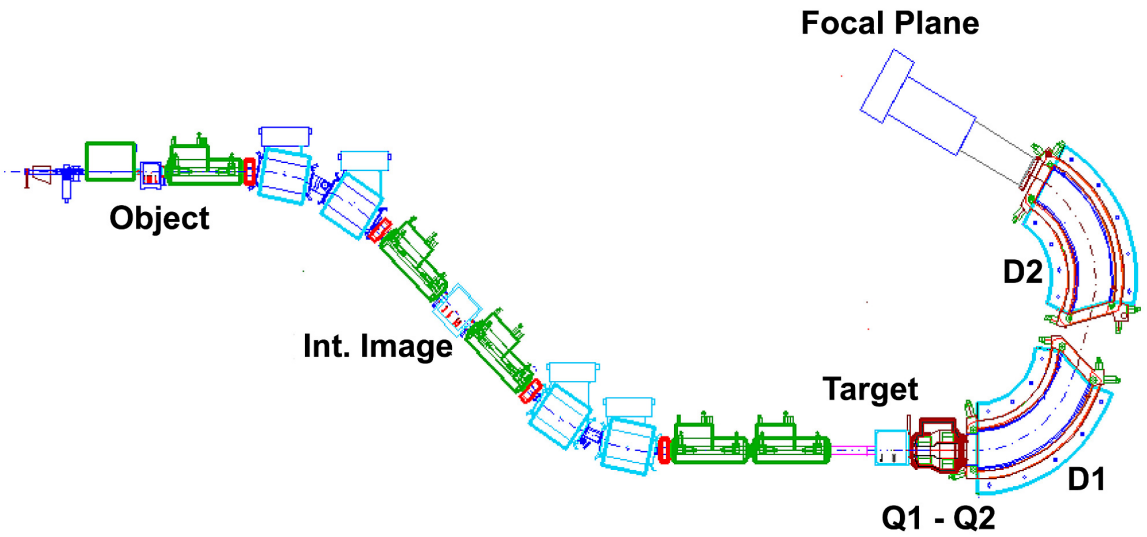

Figure 2.14: Schematic of the S800 spectrograph and analysis line. Figure taken from [50].

(CRDCs), a segmented ionization chamber (IC), a thin scintillator, and an array of sodium-doped cesium-iodide scintillators (CsI(Na)) coupled to photomultiplier tubes (PMTs), known as a "hodoscope" [49]. A schematic of the focal plane detector suite is shown in Fig. 2.15. The S800 focal plane detectors are described in Section 2.3.2, the calibrations are described in Sections 2.3.2.1, 2.3.2.2, and 2.3.2.3, and Section 2.3.3 describes the GRETINA detectors and calibrations.

2.3.2 S800 Focal Plane Detector Suite

Fragments entering the S800 focal plane are measured in a series of detectors, shown in Figure 2.15. Fragments first enter the two CRDCs, which are separated by one meter and are used to determine the trajectory of the reaction products. Individually, each CRDC measures the recoil position in the dispersive (x) and non-dispersive (y) directions with a position resolution of 0.5 mm in both directions. The CRDCs are position-sensitive

detectors filled with 80% CF_4(freon) and 20% C_4H_{10} (isobutane) gas at a pressure of 50 torr. They cover an active area of 30 cm in the non-dispersive direction by 59 cm in the dispersive direction and have an active thickness of 1.5 cm [48]. Nuclei passing through the detector volume ionize the gas and dissociate electrons, which drift toward the anode wire (along the x-direction) and induce charge on the cathode pads. There is a total of 224 cathode pads in each CRDC, each with a width of 2.54 mm. The drift time, which relates to the y position, is determined using the time difference between the thin scintillator in the focal plane and the anode wire. The 224 cathode pads must be gain-matched prior to extracting the trajectory of the fragments, and the drift time must be calibrated. This will be discussed in Section 2.3.2.1.

The ionization chamber, located immediately after the second CRDC, is used to identify the Z of reaction products based upon their energy loss through the detector volume. The ion chamber is filled with P10 gas (90% argon, 10% methane), usually at a pressure of 300 torr and consists of 16 stacked-parallel plate ionization chambers, each of which is read out individually. Nuclei passing through the ion chamber ionize the gas creating free electrons and charged gas ions. Free electrons drift toward the nearest anode while the gas ions drift toward the nearest cathode. The amount of gas ionized by the reaction recoil represents the energy loss of the recoil. The energy loss is summed across the 16 pads and because the energy loss of a recoil traversing a medium is proportional to Z^2, the ionization chamber measurements can distinguish between particles of different charge. The gain-matching procedure for the ion chamber will be discussed in Section 2.3.2.2.

Following the ionization chamber, a thin scintillator is used to obtain the time-of-flight (TOF) stop signal for the reaction recoils. The TOF start came from the radio frequency (RF) of the cyclotrons. The best timing resolution comes from scintillator-scintillator timing (much like the case of NSCL experiment e14063), but due to the beam rates in

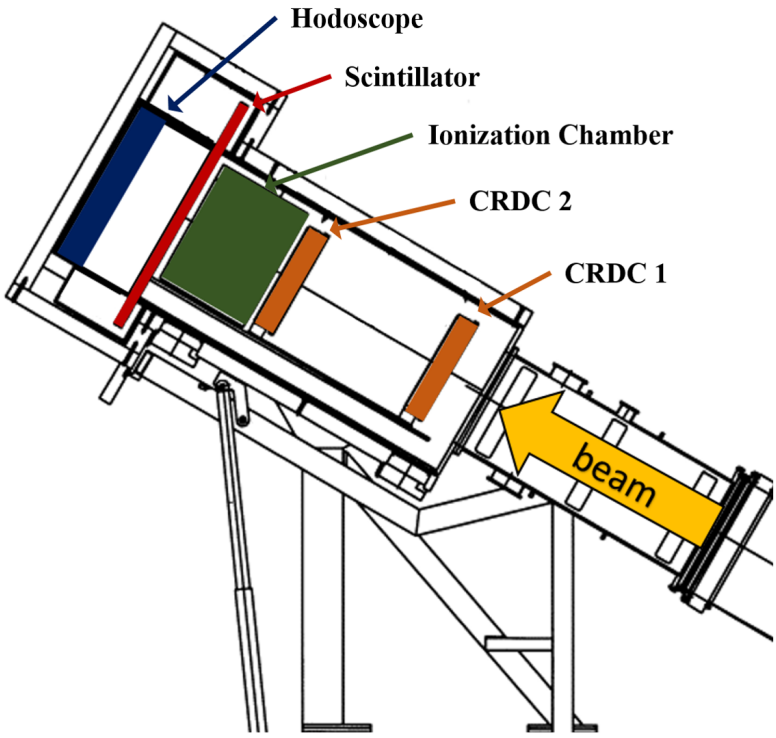

Figure 2.15: Schematic of the S800 focal plane detector suite showing the CRDCs, ionization chamber, scintillator, and CsI Hodoscope. (Modified from [48]).

this experiment, the RF timing was used. Reaction recoils were stopped in the CsI(Na) hodoscope array, located downstream of the scintillator and the total kinetic energy of the implanted nuclei was measured. The hodoscope is composed of 32 closely packed (7.6 cm $\times$ 7.6 cm $\times$ 5.1 cm) Na-doped CsI crystals coupled to photo-multiplier tubes (PMTs). The crystals are arranged in an 8$\times$4 array that covers an active area of 60 cm in the dispersive direction by 30 cm in the non-dispersive direction [49]. Figure 2.16 shows a schematic of the hodoscope array and its location in the S800 focal plane. The calibration of the hodoscope array will be discussed in Section 2.3.2.3.

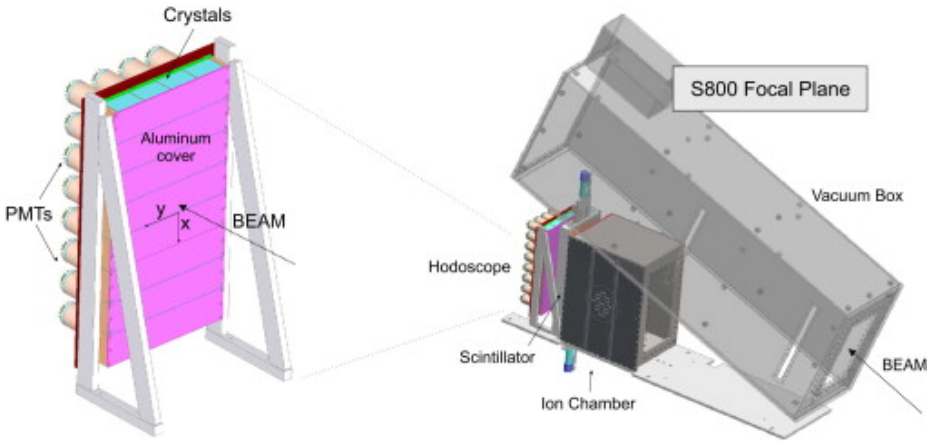

Figure 2.16: A schematic of the S800 focal plane, including the IC and hodoscope. Figure taken from [49].

2.3.2.1 CRDC Calibrations

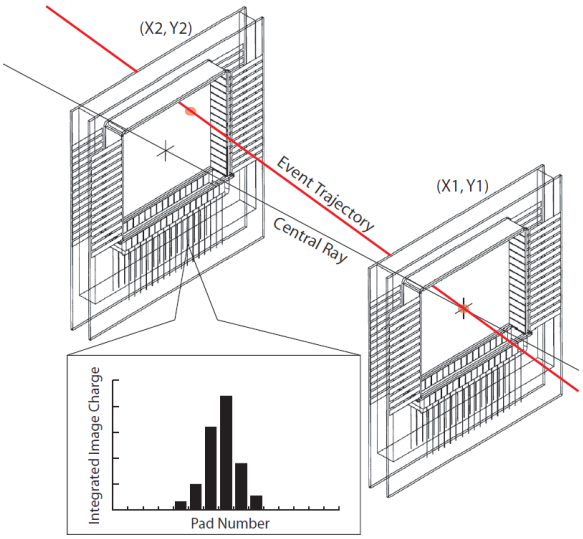

Figure 2.17: A schematic of a fragment passing through the CRDCs. The signal induced on the cathode is shown. Figure taken from [50].

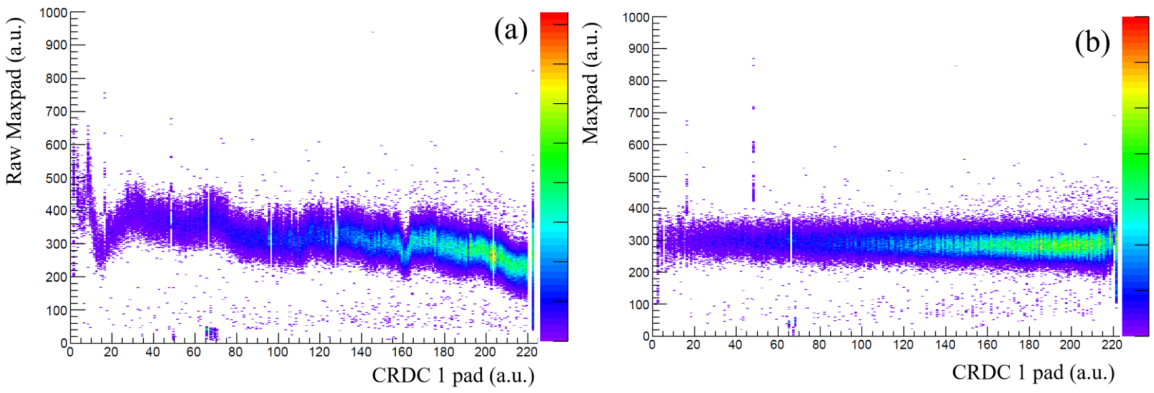

Figure 2.18: Raw CRDC pad distribution (a) and calibrated pad distribution(b). The calibrated pad distribution is uniform across the 224 pads.

The charge from each of the 224 cathode pads of a given CRDC is read out individually and the centroid of the charge distribution of the cathode pad position yields the x-coordinate of the interaction. A schematic of this process is shown in Figure 2.17, where a track in the CRDCs induces a Gaussian-like charge distribution on the pads. Prior to extracting the CRDC x-position of the fragments, the pad distribution was gain-matched because in order to extract the position reliably, the behavior of the pads should be as uniform as possible across the detector volume. The raw distribution across the 224 pads was not uniform and the position could not be determined until after the pads were gain-matched. Gates were placed on different isotopes in the PID and channel 115 in the raw CRDC spectrum (Fig. 2.18(a)) was arbitrarily used as the matching channel. The gains for all subsequent channels were matched to channel 115. This process was done for several isotopes with a range of Z to ensure that the calibration was valid for all isotopes. The raw and gain-matched CRDC pad distribution is shown in Figure 2.18.

Changes in the gas temperature and pressure cause the electron drift time to vary throughout the experiment. In order to determine the drift time (y-position relationship), a tungsten mask with known patterns of holes and lines was placed in front of each CRDC

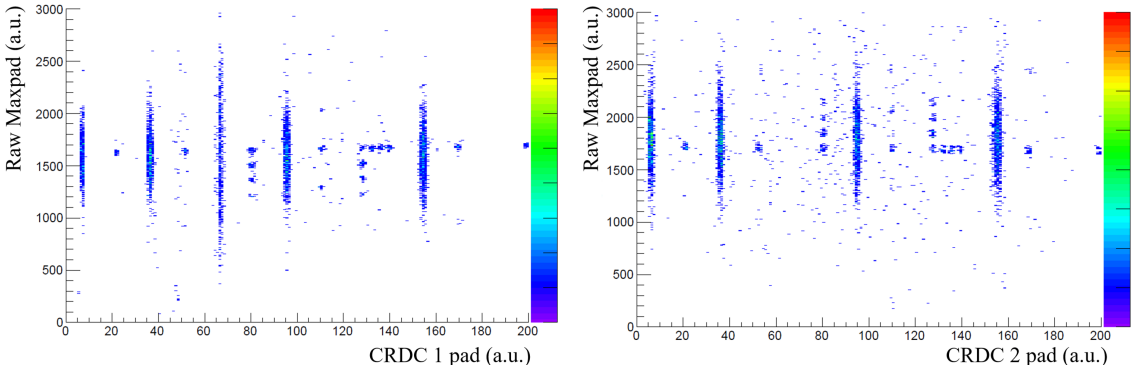

Figure 2.19: The CRDC1 mask data and the CRDC2 mask data.

periodically throughout the experiment. The pad position and drift time were mapped to their physical dimension within the CRDC volume using the mask runs. When a projectile passed through each hole or line, that known location was associated with a pad position and drift time. The mask data for CRDC1 and CRDC2 are shown in Figure 2.19. Utilizing enough of these patterns of lines and holes, the calibration between drift time to y-position was mapped and the position of a projectile within the CRDCs was determined.

The (x, y) coordinates are determined on an event-by-event basis for both CRDCs and the trajectory of the event in the focal plane is calculated. This yields the focal plane trajectory variables x_{fp}, y_{fp}, a_{fp}, and b_{fp}, where x_{fp} and y_{fp} are the focal plane positions and a_{fp} and b_{fp} are the focal plane angles. The position measurements allow the trajectory to be reconstructed on an event-by-event basis back to the target position. The trajectory reconstruction is achieved by inverse mapping the magnetic fields of the S800 dipoles from the focal plane $(x_{fp}, y_{fp}, a_{fp}, b_{fp})$ to the target position. Using the measured magnetic fields of the magnets, an analytical code called COSY INFINITY [51] constructs a transfer matrix that transforms the parameters of the beam at the target to the focal plane. In practice, the S800 Spectrograph Inverse Map Server [52] is used to obtain the transfer map used for transforming trajectories from the focal plane to the target position for a given $B\rho$.

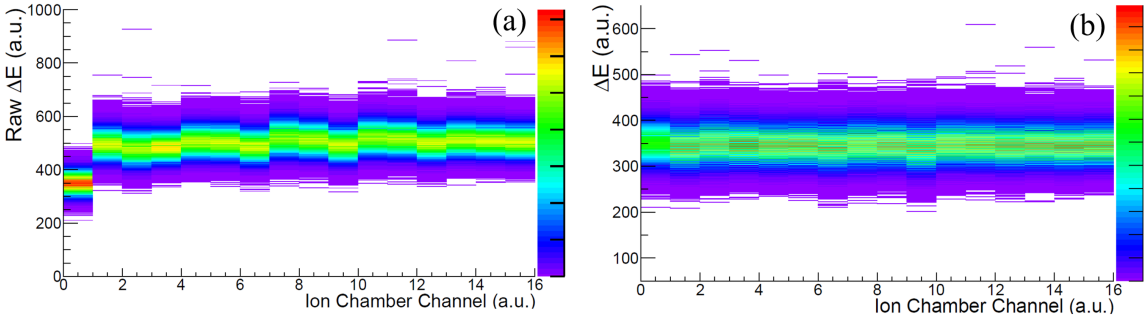

Figure 2.20: The raw (a) and gain-matched (b) ion chamber channels.

2.3.2.2 Ion Chamber Calibrations

The sixteen pads of the ion chamber are segmented along the beam-direction. The charge was collected on an event-by-event, pad-by-pad basis. The energy loss across the pads was obtained by summing the signal across the pads. Pad 0 was chosen, arbitrarily, as the channel to which the remaining pads were gain matched. Each pad had an approximately Gaussian charge distribution and the centroid value for each pad was compared with the match channel to obtain a centroid ratio. The gain-matched charge on each pad was calculated by multiplication of the raw charge on the pad with the centroid ratio. Figure 2.20 shows the raw pad distribution on the left and the corrected pad distribution on the right.

The energy loss from the ionization chamber and time-of-flight from the scintillator (and cyclotron RF) was used for identification of the fragments detected in the focal plane. Isotope chains were identified via the energy loss (ΔE) and time-of-flight (TOF) of each event, as shown in Figure 2.21. The ΔE-TOF signals yield resolution in the atomic number (Z), but not the mass resolution (A) needed to gate on individual isotopes. In order to obtain isotopic resolution, the CsI hodoscope was used to provide a total kinetic energy measurement. Kinetic energy measurements were only available for a portion of the e11029

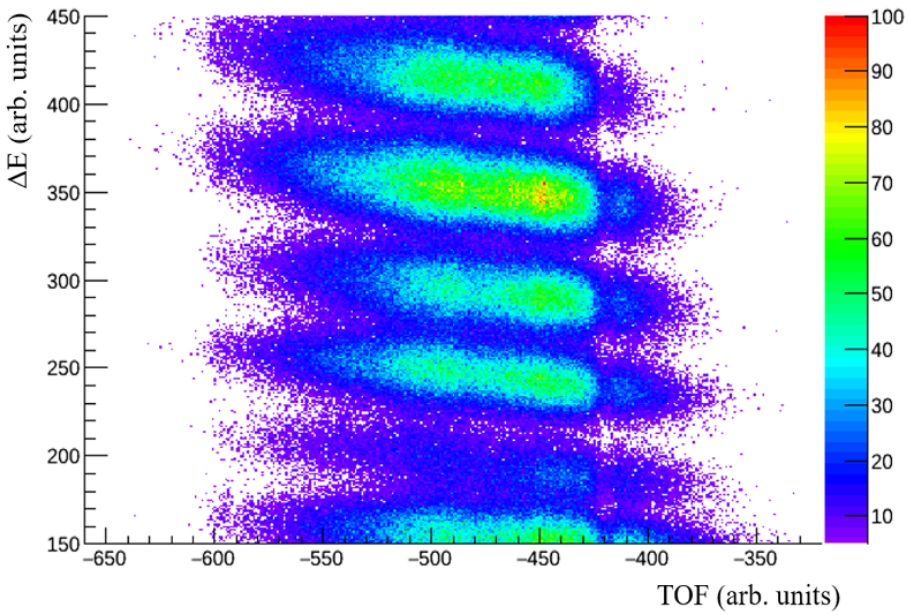

Figure 2.21: Energy loss as a function of the time-of-flight of the fragments, where each band corresponds to a chain of isotopes.

dataset because the hodoscope gains were not optimized until it was realized that the RF timing would not provide mass resolution and that the hodoscope would be required for a clean PID.

2.3.2.3 Hodoscope Calibrations

As previously mentioned, the CsI hodoscope is an 8 × 4 array of CsI(Na) crystals. Since the beam was dispersive in the focal plane and the grid of 32 crystals was separated spatially, each crystal detected different portions of the beam based upon where the fragments were located within the focal plane. The more central scintillators measured more of the beam fragments than the edge scintillators. The hodoscope calibration was the most involved among the S800 focal plane detectors and had two stages: a slope

correction and a gain correction for each crystal. For both stages, a single isotope chain from Figure 2.21 was used.

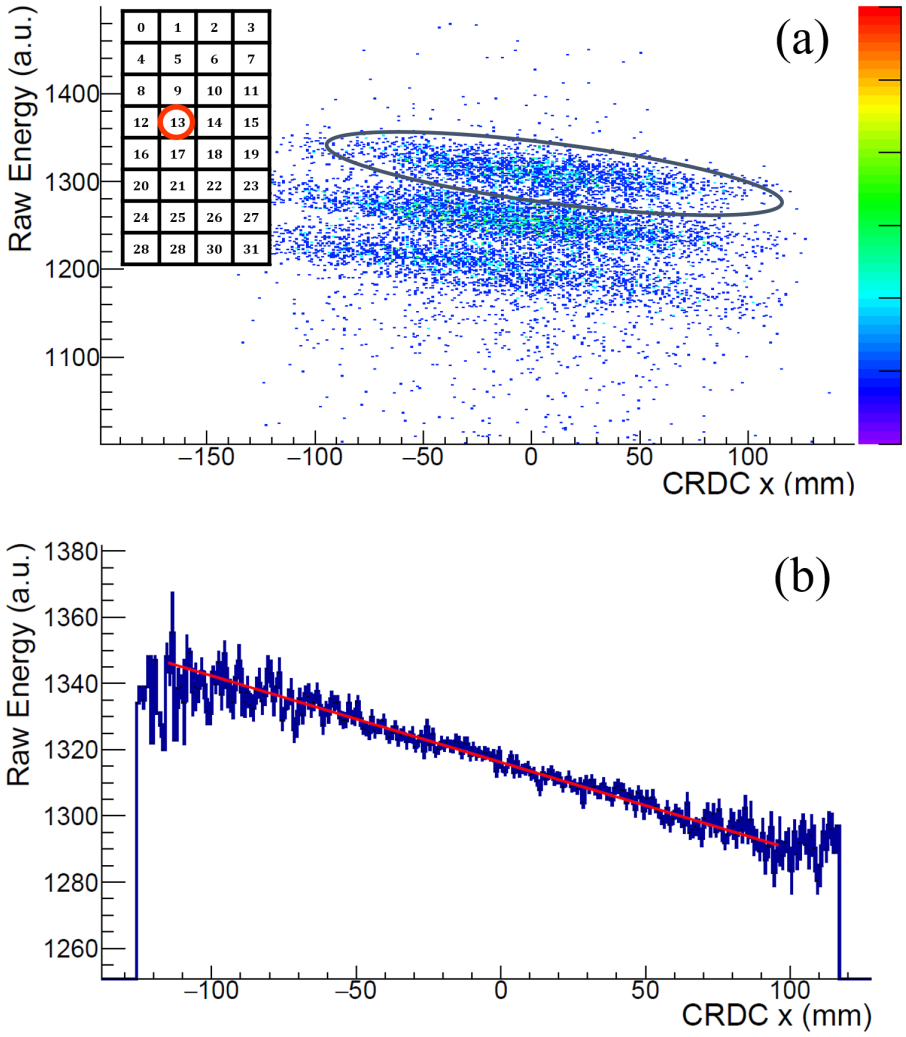

Figure 2.22: Hodoscope crystal 13 raw amplitude versus CRDC x for a particle gate on Mg (a). The three regions have an increasing slant to them due to the energy dependence on CRDC x. The gate drawn on the top-most band is used for the next stage of the calibration. The profile of the gated region from (a) with a linear fit (b).

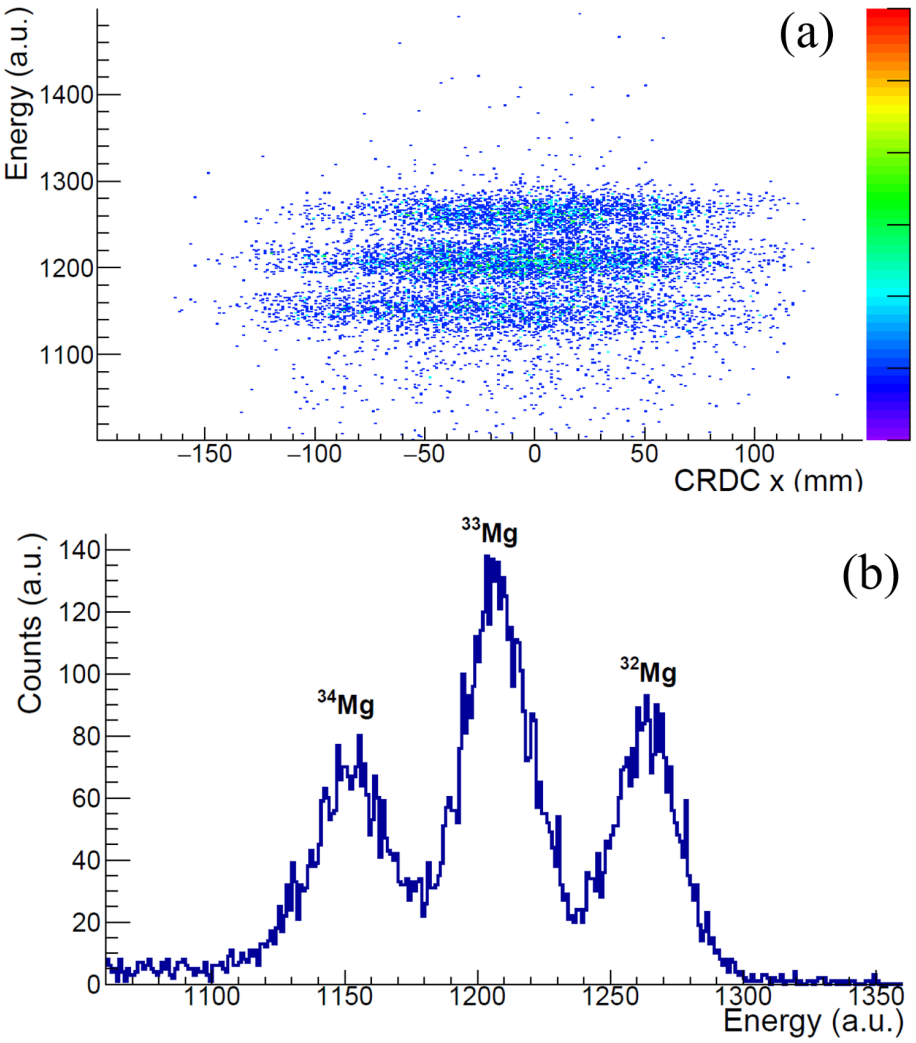

Figure 2.23: Hodoscope crystal 13 amplitude versus CRDC x for a particle gate on Mg, showing three distinct Mg isotopes (a) and the y-projection (b).

In the first stage of the calibration, the crystal signals were corrected to remove any position (x) dependence from the energy signals. The raw hodoscope spectrum gated on the $Z = 12$ chain for a representative central crystal (13) within the array is shown in Figure 2.22(a). The projection of a single band within the raw spectrum (Figure 2.22(b))

was fit to a line and the slope was extracted as the x-correction. The corrected hodoscope energy, shown in Figure 2.23, was calculated as

$$calibrated[i] = raw[i] - x_{corr} \times CRDC_x \tag{2.5}$$

where x_{corr} is the slope of the projected band and CRDC_x is the CRDC x-position. Fig. 2.23 now shows the three magnesium isotopes with no x-dependence.

For the second stage of the calibration, the same gate on the Mg isotopic chain from Fig. 2.21 was used. The hodoscope intensity distribution should be smooth as a function of CRDC x for a given isotope, and this constrains which isotopes appear in the 32 different crystals. For the Mg chain, four isotopes are observed (the three bands are visible in Figs. 2.22 and 2.23). In order to determine the gain in each crystal, the corrected hodoscope energy was produced and the number of isotopes appearing is counted and their intensities determined. For crystal 13, which is shown in Fig. 2.23 (b), three Mg isotopes are observed. Each crystal was gain-matched to crystal 13 in order to align the peaks in each crystal that corresponded to the Mg isotopes. The peaks were fit with a Gaussian and after gain matching, each Mg isotope had the same total kinetic energy (E) within each crystal and the total kinetic energy was extracted. The total kinetic energy from the hodoscope and the energy loss from the ionization chamber were used to obtain a particle identification (PID) with both atomic number and mass resolution, as shown in Fig. 2.24.

Data that did not have the hodoscope measurement were analyzed using ΔE-TOF information and time-of-flight gates for PID. From the data that did have the hodoscope measurement, a gate was placed around each individual Mg isotope and the projection into the time-of-flight was analyzed to determine which isotopes dominated in a particular region in the time-of-flight. Fig. 2.25 shows the projections for ^{31}Mg shown in blue, ^{32}Mg shown in magenta, ^{33}Mg shown in red, and ^{34}Mg shown in green. While the time-of-flight for each isotope does overlap, regions were chosen in such a way as to avoid as

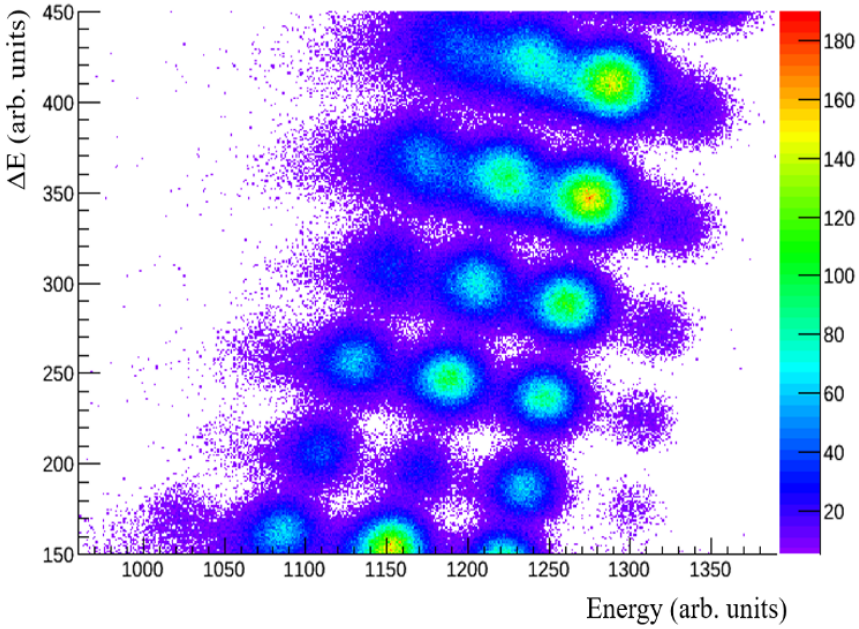

Figure 2.24: Total kinetic energy of the particle with respect to the energy loss in the ion chamber. Both atomic number and mass resolution are present.

much contamination from neighboring isotopes as possible. Data without the hodoscope measurement identified isotopes using the PID from Fig. 2.21 and cuts on the time-of-flight regions. The TOF gate used for ^{33}Mg was -540 to -508.

2.3.3 GRETINA

Prompt γ-rays were detected by seven GRETINA modules that surrounded the S800 target position. Each module was placed at 90° with respect to the beam direction in order to minimize beam-induced backgrounds from light particles produced in the high-intensity secondary fragmentation, which are forward focused in the laboratory frame. Figure 2.26 shows the seven detectors placed at 90° angles, surrounding the S800 target. The high segmentation and digital pulse-shape processing of GRETINA allows the interaction energies and positions to be measured with sub-segment resolution. Utilizing the γ-ray

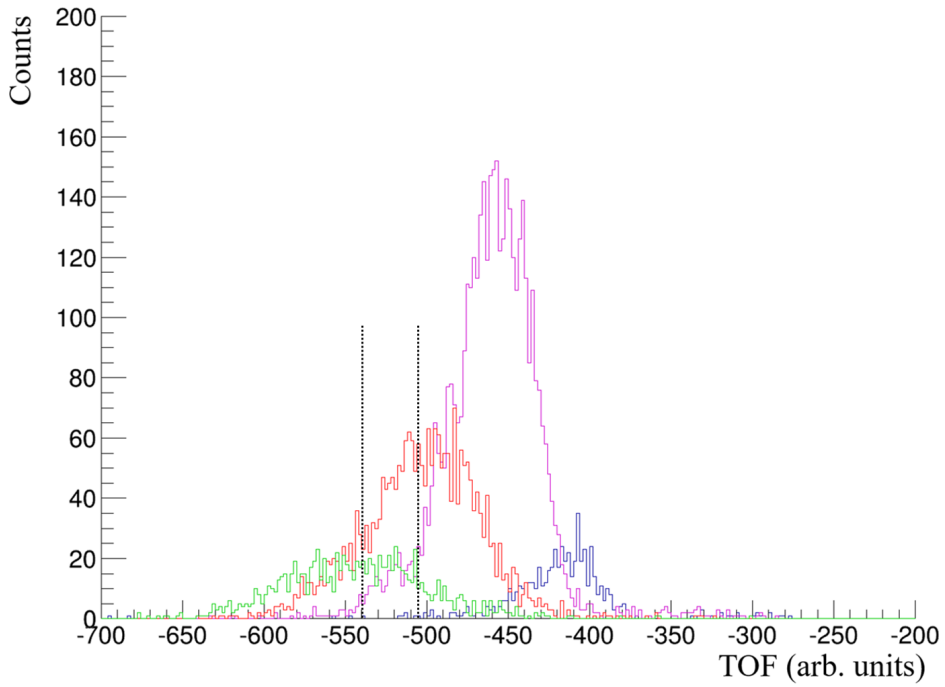

Figure 2.25: The time-of-flight projections for the Mg isotopic chain. The blue line corresponds to ^{31}Mg, the magenta to ^{32}Mg, the red to ^{33}Mg, and the green to ^{34}Mg. The TOF gate for ^{33}Mg is indicated with dashed black lines.

trajectories from GRETINA and particle trajectories from the S800, γ-rays emitted from the fragmentation products (with $v/c = 0.4$) were Doppler reconstructed on an event-by-event basis, achieving an energy resolution (FWHM) of $\sim$2%. A GEANT4 simulation of the GRETINA response excluding the photopeaks using the UCGretina code [53], combined with a smooth double-exponential function, was used to fit the background to allow accurate determination of γ-ray yields without constraining the peak shape. These yields were efficiency corrected based upon the GEANT4 simulated array efficiencies including the Lorentz boost.

At the time of the experiment, GRETINA consisted of seven modules, each being composed of four closely packed high-purity germanium (HPGe) crystals. The 28 crystals

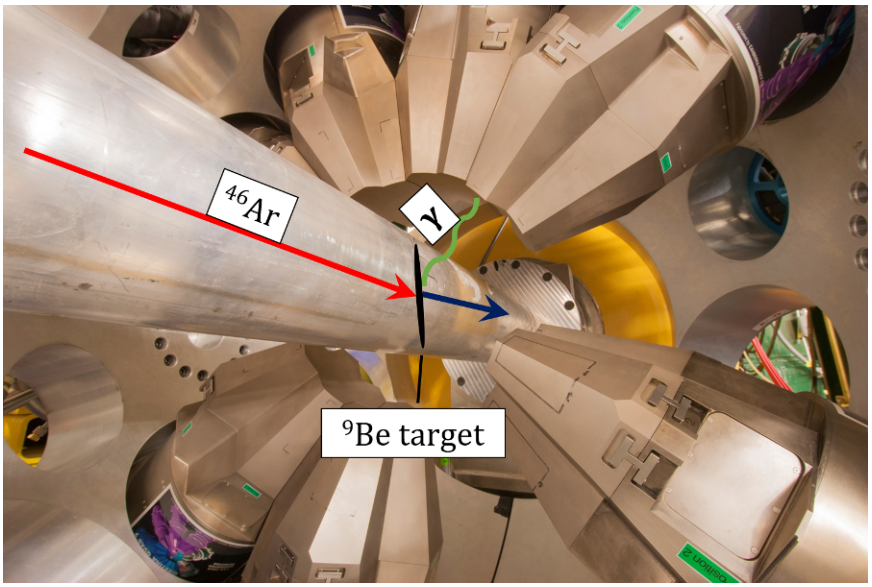

Figure 2.26: The GRETINA detector array at the target position of the S800. Detectors are located at 90° angles with respect to the target. Photo courtesy of Shumpei Noji.

were electronically segmented into 36 segments each. In order to maximize the resolution of the array, digital pulse shape analysis was used to obtain sub-segment position resolution. The modules are highly segmented and therefore the positions and energies of the γ-ray interaction points can be measured, and γ-rays tracked. Because the fragmented beam was traveling at approximately 40% the speed of light ($\beta = 0.4$), the detected γ-rays required Doppler correction. The γ-ray interaction points, and reaction recoil trajectory information from the S800 were used to correct the Doppler broadening and shift of the emitted γ-rays on an event-by-event basis.

The Doppler correction formula describes the correction made to the broadened and shifted γ-rays,

$$E_\gamma^0 = \gamma(1 - \beta\cos\theta)E_\gamma, \tag{2.6}$$

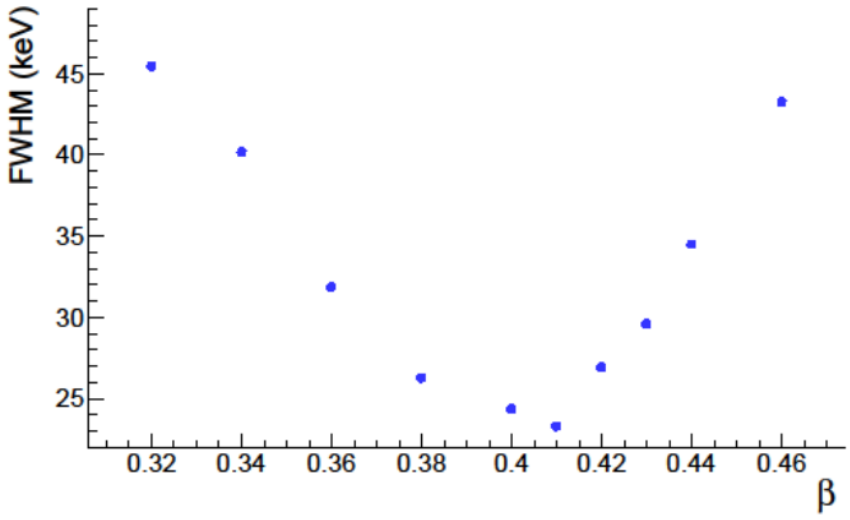

Figure 2.27: The FWHM of the 484.1 keV peak in ^{33}Mg versus β. The optimal β for the data is the minimum FWHM, corresponding to 0.41c.

where θ is the angle between the particle and the emitted γ-ray, $\beta = v/c$, where v is the velocity of the beam, E_γ is the γ energy measured in the laboratory frame, and $\gamma = 1/\sqrt{1-\beta^2}$. In order to determine β, one of the γ-rays in ^{33}Mg was fit using a Lorentzian distribution and β was varied between 32% and 46% the speed of light. Fig 2.27 shows the full-width-at-half-maximum (FWHM) of the γ-ray with respect to β. The optimized β of the data corresponds to the smallest FWHM, which is 0.41. This value is reasonable based on the Bρ of the incoming beam and LISE++ calculations [54].

Calibration of the energy and efficiency of the GRETINA detectors was performed using ^{56}Co, ^{60}Co, ^{152}Eu, and ^{226}Ra sources at the beginning of the experiment and ^{226}Ra and ^{152}Eu at the end of the experiment to check the consistency of the calibration. In NSCL e11029, the energy calibration was determined at the beginning of the experiment for each crystal, and the calibrated energies were output by the decomposition algorithm.

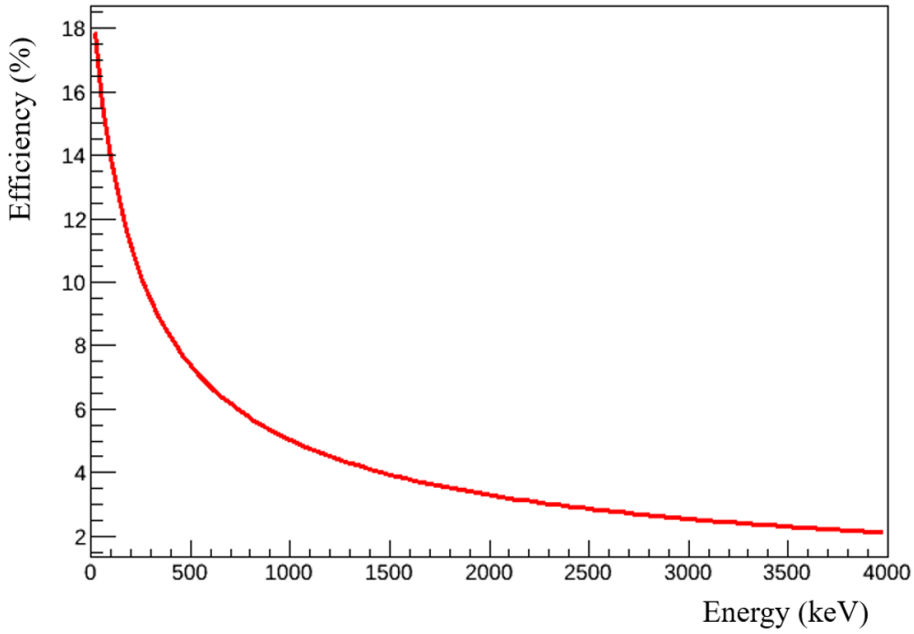

Figure 2.28: GRETINA efficiency as a function of energy from 0 to 4 MeV.

The calibration procedure was essentially identical to that described for SeGA in NSCL experiment e14063.

The absolute efficiency of GRETINA for seven quads is given by

$$\varepsilon_{absolute}(\%) = a \times exp(-b \times log(E + c)), \tag{2.7}$$

where E is the γ-ray energy in keV and a, b, and c are constants with values of 614.0, 0.68, and 160.0, respectively. The absolute efficiency curve is shown in Fig. 2.28. The absolute efficiency measurement was not done in the current work, instead the functional form shown above was used. The absolute efficiency was originally determined with the use of a ^{152}Eu source and a GEANT4 simulation of the array. The procedure is similar to what was described in Section 2.2.4.2 for the SeGA array. The efficiencies of γ-rays emitted in-beam are determined based on the previously mentioned GEANT4 simulation

of the array including the Lorentz boost. The boosted efficiency depends on the γ-ray energy and will be shown in Chapter 4 along with the experimental results.

2.3.4 Data Acquisition and Electronics

Data acquisition for the S800 consisted of analog electronics, and all detector signals were readout in a standard VME framework. The S800 trigger was derived from the thin plastic scintillator. Particle single events were readout when the plastic scintillator had a signal. Readout of GRETINA was done via the custom digital data acquisition system associated with the array. The GRETINA trigger was a signal in coincidence with the S800 trigger (particle singles), which also caused readout. In addition to particle-γ coincidences, down-scaled particle-singles were also recorded.

3 E14063 Results and Discussion

The previous chapters have described the techniques of β-decay and β-delayed γ-ray spectroscopy, as well as the experimental details of the set-up for NSCL experiment e14063. Results from this experiment are presented in this chapter.

From the implant-delay correlation, as described in Chapter 2, β-decay curves and β-delayed γ-ray spectra were obtained. The β-decay half-lives were determined by fitting the decay curve using the Bateman equations. γ-ray transitions were identified in the γ-ray singles spectrum based upon γ-ray coincidences and half-life information from the γ-gated decay curves. $\gamma - \gamma$ matrices were constructed from events with γ-multiplicities of at least two, allowing analysis of γ-ray coincidence information.

NSCL experiment e14063 included more than 20 neutron-rich isotopes in the N=20 to N=28 region of the neon, sodium, magnesium, aluminum, silicon, and phosphorus isotopes. This chapter presents the results, including β-decay half-lives, β-delayed γ-ray information, level schemes, and decay schemes for the β-decay of $^{32-33}$Na and ^{33}Mg with specific focus on the A=33 isobars, which complement the results obtained in the e11029 experiment, presented in Chapter 5.

3.1 β decay of ^{32}Na to ^{32}Mg

The β-decay of ^{32}Na has been studied since the early 1980's [26] and was used in the current work to benchmark the analysis codes against collaborators at Florida State University and against the literature before moving to the A=33 case. The results from the decay of ^{32}Na to its descendants is presented here.

3.1.1 γ-rays, $\gamma - \gamma$ Coincidences, and Level Scheme

The β-delayed γ-ray spectrum for decays detected within 100 ms of the implantation of a ^{32}Na ion is shown in Fig. 3.1. γ-ray transitions were associated with the daughter

Table 3.1: Experimentally observed γ-rays from the β-decay of ^{32}Na.

Energy (keV)	$I_{absolute}$ (%)	Decay	Isotope
170.3 (4)	3.3 (4)	β-n	^{31}Mg
221.0 (4)	6.5 (6)	β-n	^{31}Mg
884.8 (4)	47.0 (34)	β	^{32}Mg
1434.9 (4)	2.1 (5)	β	^{32}Mg
1481.3 (4)	4.2 (7)	β-2n	^{30}Mg
1780.7 (4)	6.6 (9)	β	^{32}Mg
1971.2 (4)	2.8 (6)	β	^{32}Mg
2149.7 (4)	21.1 (21)	β	^{32}Mg

nucleus ^{32}Mg (labeled in black) based upon γ-gated β-decay curves and observed $\gamma - \gamma$ coincidences. In addition to transitions in the daughter, several transitions were observed in the grand-daughter (following ^{32}Mg $\rightarrow$^{32}Al decay) (green circle) and the β-delayed one-neutron and two-neutron decay of ^{32}Na to ^{31}Mg and ^{30}Mg (purple diamonds and gray squares), respectively. The transitions arising from the decay of ^{32}Na are shown in Table 3.1 along with their respective intensities. All remaining γ-rays arose from transitions in neighboring isotopes; these transitions arise from the accidental correlation of the decay with other nuclei and are marked with yellow triangles.

The 884.8, 1434.9, 1780.7, 1971.2, and 2149.7 keV transitions are well-known and were previously placed in the level scheme for ^{32}Mg. The 170.3 and 221.0 keV γ-rays correspond to transitions in ^{31}Mg following β-1n decay and the 1481.3 keV transition to ^{30}Mg following β-2n decay. This experiment was not sensitive to neutrons so all neutron-delayed β-decay branching ratios are lower limits. Based upon the absolute intensities of the 170.3 and 221.0 keV transitions, the β-1n branching fraction to ^{31}Mg had a lower limit

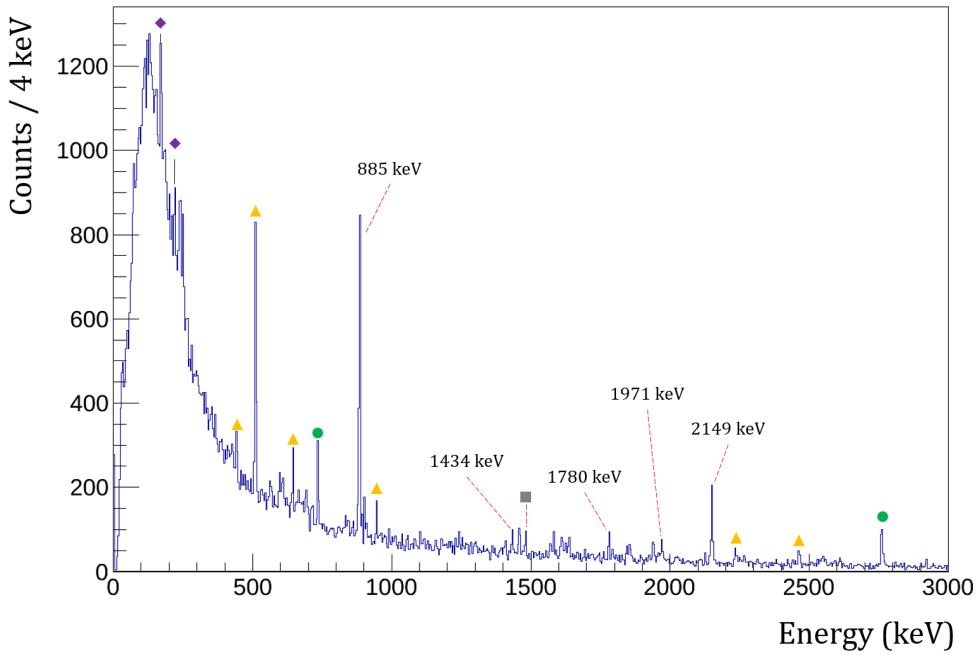

Figure 3.1: The γ-ray singles spectrum for ^{32}Mg from the β-decay of ^{32}Na. Transitions from the daughter, ^{32}Mg, are labeled in black with red lines, transitions from the grand-daughter, ^{32}Al, are indicated with green circles, transitions arising from β-delayed neutron decays are shown with purple diamonds (^{31}Mg) and gray squares (^{30}Mg), and the yellow triangles indicate background lines from neighboring isotopes.

of 8.7 (27)%. Likewise, from the absolute intensity of the 1481.3 keV transition, the β-2n branching fraction to ^{30}Mg had a lower limit of 3.8 (6)%. The literature branching fractions from experiments that measured neutrons are 24 (7)% and 8.3 (21)% for the β-1n and β-2n decays, respectively [26, 55–57]. The 170.3 keV transition has also been observed in ^{32}Mg in past experiments but considering the literature β-1n branching fraction and the literature branching ratio between the 170.3 and the 221.0 keV transitions in ^{31}Mg [26, 57–59], the full intensity of the 170.3 keV transition was attributed to the β-1n decay to ^{31}Mg.

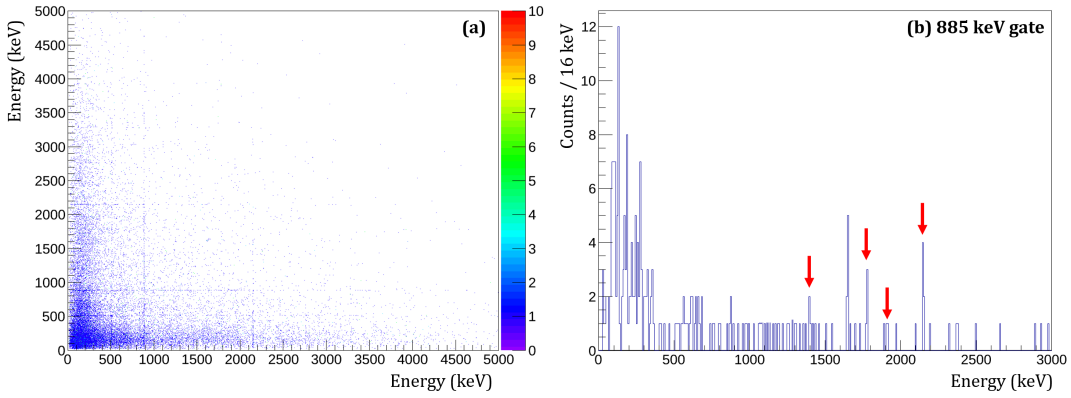

Figure 3.2: The $\gamma-\gamma$ matrix (a) and gated projection (b) for the 885 keV transition in ^{32}Mg. The projection shows coincidences with the 1434 keV, 1971 keV, 1780 keV, and 2149 keV γ-rays.

This resulted in zero intensity for the 170.3 keV transition in ^{32}Mg with an upper limit calculated from propagation of errors. This will be discussed further in Section 3.1.2.

The $\gamma-\gamma$ coincidence matrix and representative gated projection of the 884.8 keV transition are shown in Fig. 3.2. A gate was placed on each transition from the singles spectrum (Fig. 3.1) and the $\gamma-\gamma$ matrix was projected onto one of the energy axes to ascertain the presence of coincidences. Fig. 3.2(b) shows the projection of the 884.8 keV γ-ray. The coincidences are marked with a red arrow. In ^{32}Mg, the 1434.9, 1780.7, 1971.2, and 2149.7 keV transitions are all seen to be in coincidence with the 884.8 keV transition. Gating on the 1434.9, 1780.7, 1971.2, and 2149.7 keV transitions individually also all show coincidence with the 884.8 keV, confirming the relationship.

From the γ-ray singles and $\gamma-\gamma$ analysis, the level scheme for ^{32}Mg was constructed and is shown in Fig. 3.3. Of the five transitions observed in ^{32}Mg, one transition was placed as directly de-exciting to the ground state and the remaining four transitions all de-excite

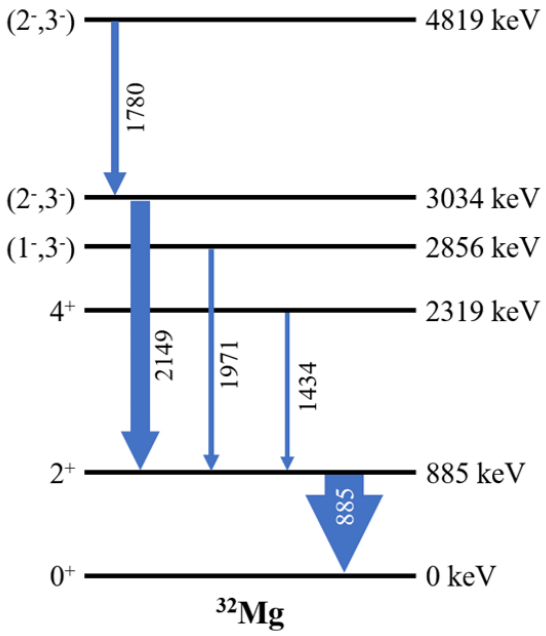

Figure 3.3: The level scheme for ^{32}Mg constructed from γ-ray singles and $\gamma - \gamma$ coincidences.

to the first excited state. The spins and parities shown in the constructed level scheme were taken from the adopted levels in the ENSDF database [1] and from arguments presented in Section 3.1.3. The level scheme from the current work is in good agreement with the literature.

3.1.2 Half-life and Decay Scheme

The β-decay curve observed for decays that occurred within 100 ms of the implantation of a ^{32}Na ion in the GeDSSD is shown in Fig. 3.4. The decay curve was fit using the Bateman equations and a log-likelihood method, considering the β-decay components arising from the daughter (^{32}Mg) and grand-daughter (^{32}Al) decays, and a constant background. The half-lives of ^{32}Mg and ^{32}Al were fixed at the known literature

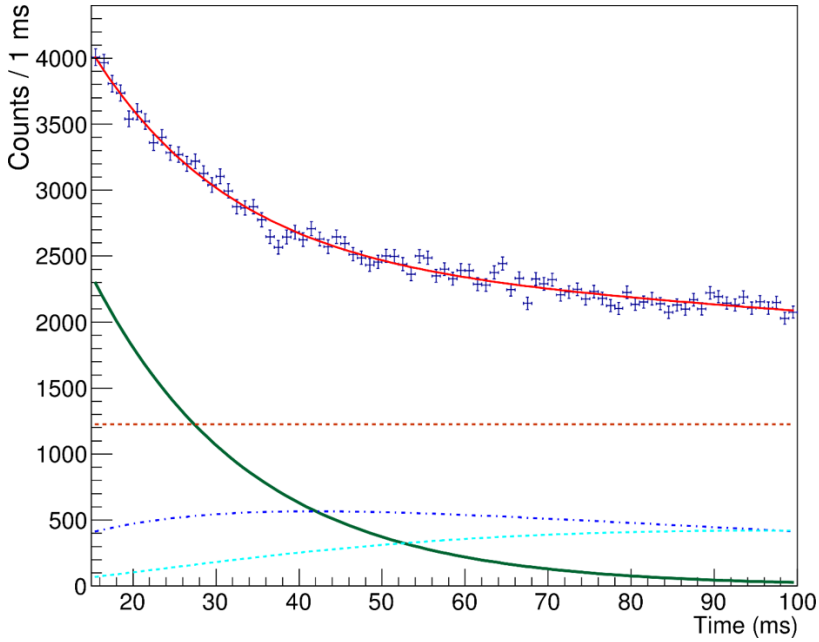

Figure 3.4: The ^{32}Na decay time curve fit with the Bateman equations. The red solid line represents the total fit. The brown hashed line is a linear background component, the blue hashed line is the ^{32}Mg daughter decay (from literature), the teal hashed line is the ^{32}Al grand-daughter decay (from literature), and the solid green curve is the fit for the ^{32}Na decay only.

values of 86 (5) ms and 33.0 (2) ms, respectively [1]. The literature half-lives for the daughter and grand-daughter were varied within their respective error bars to determine their impact on the extracted half-life for ^{32}Na. The half-lives of ^{31}Mg and ^{30}Mg were 232(15) ms and 335(17) ms, respectively, and were not necessary in the fit since their half-lives were longer than the correlation time.

A half-life of 13.1(4) ms was extracted for ^{32}Na using the literature values for each component of the fit. This value is in excellent agreement with the value of 13.2(5) ms adopted in the literature [56, 58]. The γ-gated decay curves for transitions in ^{32}Mg were used to confirm the half-life of ^{32}Na. The decay-curve fit gated on the 884.8

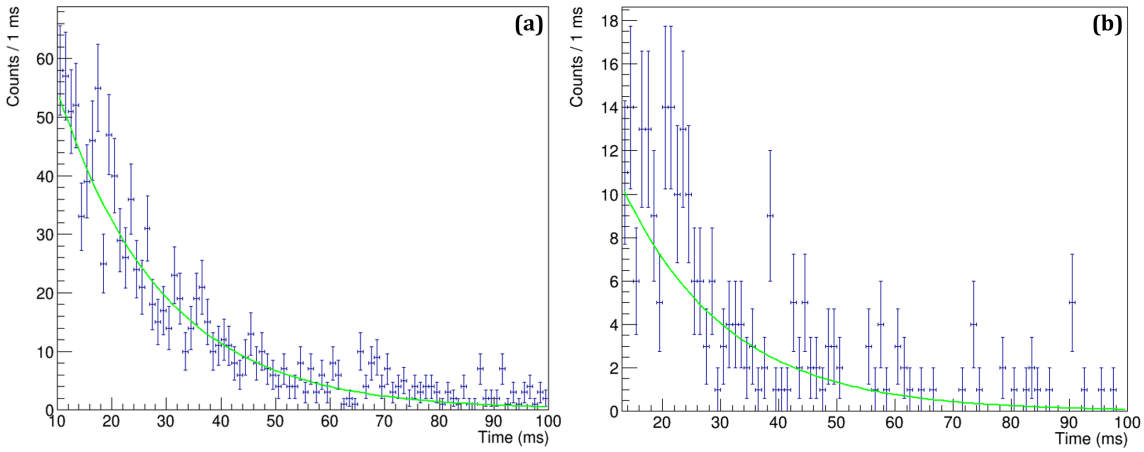

Figure 3.5: The γ-ray gated decay curves along with exponential decay fits for the 885 keV transition (a) and the 2149 keV transition (b). The half-life fits are shown in green and are in good agreement with the values from the literature and this work.

and 2149.7 keV transitions, shown in Fig. 3.5, yield half-life results of 13.3(2) ms and 12.5(22)ms, respectively. The gated decay curves were fit using a log-likelihood method and a constant term was not included in the exponential fit. Error bars in the plots are shown with $\sqrt{N}$ errors for visualization purposes.

Combining the information from the γ-ray singles and $\gamma - \gamma$ analysis, as well as literature arguments, the decay scheme for ^{32}Na was constructed and is shown in Fig. 3.6. The total number of decays in ^{32}Na was extracted by integration under the parent curve (shown in solid green in Fig. 3.4) and was found to be 44184 ± 210 decays. The feeding to each level was calculated such that there was a balance between intensity into and out of each level. Table 3.2 shows a summary of the calculation of the β-decay feedings to each level. Based upon the feeding intensities and level energies, the log(fT) values for each level were calculated using the LOGFT analysis program from the NNDC [1]. The decay scheme summarized in Table 3.2 and shown in Fig. 3.6 assumes the literature values for

Table 3.2: Summary of the decay scheme β-decay feeding intensity parameters and error estimations for ^{32}Na including the experimental β-n branches. The asymmetric error bars on the 885 keV and ground state levels arise from the 171 keV yield that was attributed to the β-1n branch.

E_{Level} (keV)	In	Out	Decays	I_β (%)	log(fT)
4819 ± 2.9	decays	2613 ± 426	2613 ± 426	5.9 ± 1.0	5.37 ± 0.08
3034 ± 2.5	decays + 2613 ± 426	8389 ± 749	5776 ± 826	13.1 ± 1.9	5.26 ± 0.07
2856 ± 1.9	decays	1131 ± 366	1131 ± 366	2.6 ± 0.8	5.99 ± 0.14
2319 ± 2.0	decays	840 ± 317	840 ± 317	1.9 ± 0.7	6.19 ± 0.17
885 ± 1.4	decays + 10360 ± 803	18666 ± 1165	8306^{+1415}_{-1862}	$18.8^{+3.2}_{-4.2}$	$5.36^{+0.08}_{-0.10}$
^{31}Mg (β-1n)	decays			24 ± 7	
^{30}Mg (β-2n)	decays			8.3 ± 2.1	
g.s.	decays + 18666 ± 1165	0		$25.5^{+8.3}_{-8.8}$	$5.32^{+0.14}_{-0.16}$

the β-delayed neutron branches and is referenced to discuss the intensities and log(fT) values for each energy level.

3.1.2.1 Classification Based on log(fT) Values

Both the 4819 keV and 3034 keV levels have tentative J^π assignments of 2^- or 3^-. The decay feeding intensity to these levels is 5.9 (10)% and 13.1 (19)%, respectively, yielding log(fT) values of 5.37 (8) and 5.26 (7), and classifying the decays as *allowed*. The 2856 keV level, with tentative J^π of 1^- or 3^-, has a feeding intensity of 2.6 (8)% and a log(fT) of 5.99 (14), which is on the cusp of being classified as *allowed* or *first forbidden*.

The next three levels of ^{32}Mg have well established J^π values. The 4^+ level at 2319 keV had a feeding intensity of 1.9 (7)% and a log(fT) of 6.19 (17), which again can be classified as *allowed* or *first forbidden*. The 885 keV level is the 2^+ member of the ground state band

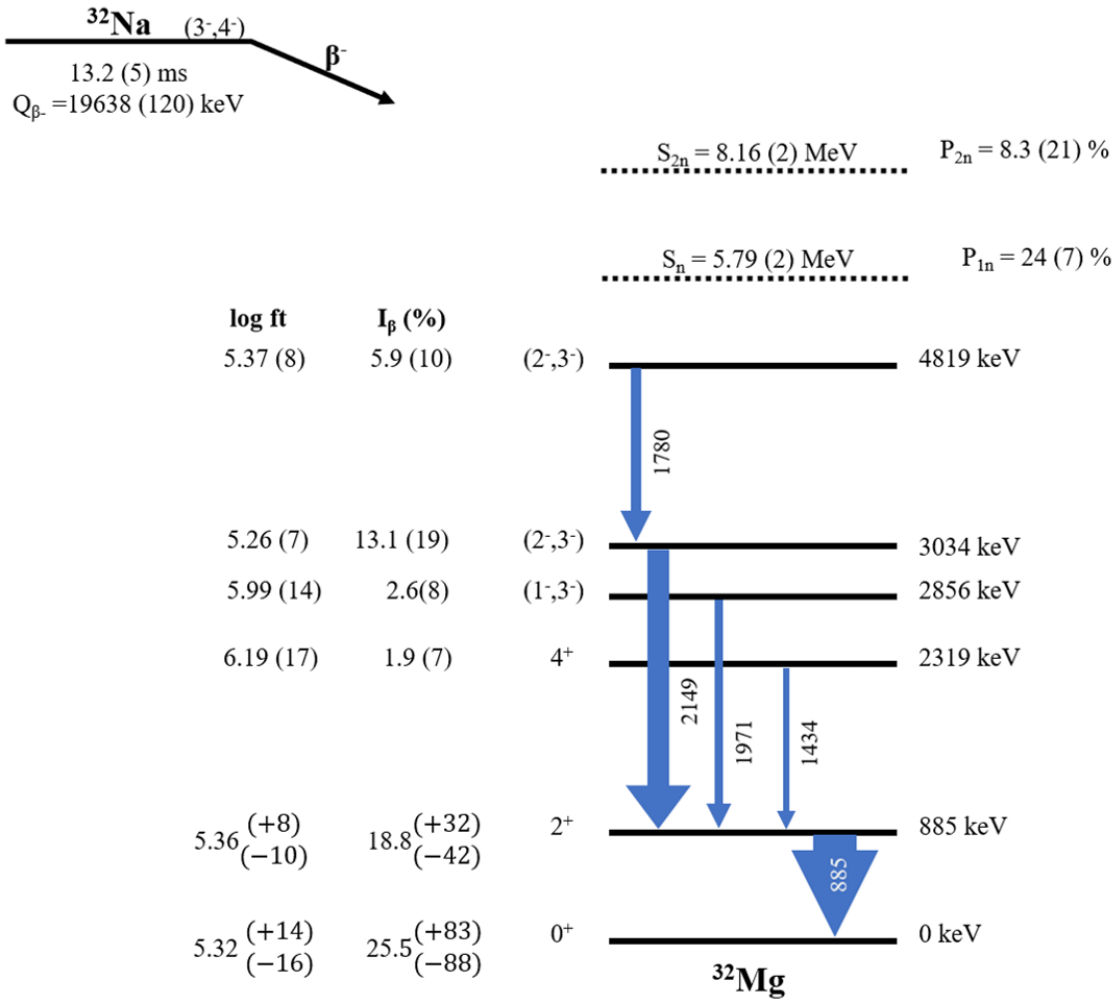

Figure 3.6: The decay scheme for ^{32}Na showing the feeding intensity and log fT values for each level in ^{32}Mg. The neutron branching fractions are shown as the values adopted in the literature [1, 26, 55–57].

and had a feeding intensity of 18.8 $^{+3.2}_{-4.2}$, which yields another *allowed* decay based upon the log(fT) of 5.36 $^{+0.08}_{-0.1}$. As previously mentioned, the asymmetric error bars for this level arise due to the 171 keV transition, which has been observed in the literature [26, 57–59] to be in coincidence with the 885 keV γ-ray, de-exciting from the 1058(2) keV level. The full intensity, in this case, was attributed to ^{31}Mg and the yield attributed to the 885 keV level

in ^{32}Mg was zero with an upper error limit of 1210, which was incorporated into the error propagation for the number of decays to the 885 keV level and thus the feeding intensity and log(fT). Using the β-delayed neutron branches from the literature, the ground state had a feeding intensity of 25.5 $^{+8.3}_{-8.8}$%, which results in a log(fT) of 5.32 $^{+0.14}_{-0.16}$, making it an *allowed* decay.

3.1.3 Discussion of ^{32}Na Ground State and ^{32}Mg Level Scheme

The ^{32}Na ground state has two possible J^π assignments in the evaluated literature data, namely a 3^- or a 4^- [1]. The tentative (3^-,4^-) assignment for the ^{32}Na ground state arose from shell model predictions and comparison to experimental data in the β-delayed neutron decay of ^{32}Na to ^{31}Mg [57]. While this work was not able to definitively make a ground state J^π assignment, the negative parity nature of the ground state was established, and the J was determined to be less than 4, but more likely to be either a 3^- or a 4^-. Based upon the log(fT) values from the current work for the decay to each level in ^{32}Mg, the implications of the tentative J^π assignments for the ^{32}Na ground state are discussed below.

3.1.3.1 The 3^- Case

For the first case, we assume the 3^- assignment for the ground state of ^{32}Na is correct. In that case, using the selection rules, each decay classified as *allowed* by the log(fT) values would exhibit no change in parity and would have ΔJ values of either 0, for a Fermi decay, or in the case of a Gamow-Teller decay, either 0 or ± 1. The possible J^π assignments for these levels based upon the experimental log(fT) values would be 2^-, 3^-, or 4^- . In the case of the two potential *first forbidden* decays, there would be a change in parity and ΔJ would either be 0 or ± 1 for a Fermi decay, or 0, ± 1, or ± 2 for a Gamow-Teller decay. The possible J^π values would be 1^+, 2^+, 3^+, 4^+, or 5^+.

The 4819 keV, 3034 keV, 885 keV, and ground state levels are each classified as *allowed* from their log(fT) values and from selection rules would have J^π values of 2^-,

Table 3.3: Summary of the decay classifications for the levels in ^{32}Mg if the ^{32}Na ground state is a 3^-. The first four columns correspond to classifications based upon the $\log(fT)$ only, while the last three columns correspond to classifications based upon the change in spin and parity. *F* corresponds to a Fermi type decay and *GT* corresponds to a Gamow Teller type.

Classification from $\log(fT)$				Classification from Selection Rules		
E_{level} (keV)	J^π	$\log(fT)$	Classification	ΔJ	$\Delta\pi$	Classification
4819	$(2^-,3^-)$	5.37 (8)	allowed	0,1	no	allowed: F, GT
3034	$(2^-,3^-)$	5.26 (7)	allowed	0,1	no	allowed: F, GT
2856	$(1^-,3^-)$	5.99 (14)	allowed, 1st forbidden	0,2	no	allowed: F, GT (0)
						2nd forbidden: F, GT (2)
2319	4^+	6.19 (17)	allowed, 1st forbidden	1	yes	1st forbidden: F, GT
885	2^+	$5.36\ ^{(8)}_{(10)}$	allowed	1	yes	1st forbidden: F, GT
g.s.	0^+	$5.32\ ^{(14)}_{(16)}$	allowed	3	yes	3rd forbidden: F, GT

3^-, or 4^-. For both the 4819 and 3034 keV levels, this is consistent with the tentative J^π of 2^- or 3^- adopted in the literature [1]. Based on the $\log(fT)$ values for the 885 keV level and the ground state, their possible J^π values are 2^-, 3^-, or 4^-, however, these states are well-known positive parity states having J^π values of 2^+ and 0^+, respectively. Using the known J^π assignments, the 885 keV and ground state could be classified as either *first forbidden* or *third forbidden*, respectively. The 885 keV being classified as *first forbidden* is probable since the $\log(fT)$ value classification ranges do overlap.

The 2856 keV and 2319 keV levels could be classified as either *allowed* or *first forbidden* based on their $\log(fT)$ values, which yields possible negative J^π values of 2^-, 3^-, or 4^- and possible positive J^π values of 1^+, 2^+, 3^+, 4^+, or 5^+. For the 2856 keV level, the adopted, tentative J^π values are 1^- and 3^- and from the current work, the *allowed*

nature of the decay makes the 3^- assignment more likely. The 2319 keV level is another well-established positive parity state (4^+), which is consistent with the current work since the decay could be classified as *first forbidden*. Table 3.3 presents a summary of the classifications for each level.

In summary, the 3^- assignment for the ground state of ^{32}Na is in consistent with the $\log(fT)$ values from the current work and the adopted J^π values for each of the levels in ^{32}Mg, except for the ground state. The inconsistency in the ground state classification arises from the so-called 'Pandemonium effect' [60]. The total β-feeding is spread over all available levels, and γ-intensity emitted from less populated levels will be weak. Our analysis is only sensitive to the strongest branches and often the weaker branches are missed in the analysis. This means that β-feeding intensities to each level are upper limits and thus $\log(fT)$ values are lower limits. The inconsistencies observed in the ground state feeding and $\log(fT)$ arise from the unobserved feeding to less populated states.

3.1.3.2 The 4^- Case

For the second case, we assume that the ground state of ^{32}Na has a 4^- assignment. From the selection rules and using a 4^- as the ground state of the parent, all *allowed* decays would have possible J^π values of 3^-, 4^-, or 5^- and decays classified as *first forbidden* by the $\log(fT)$ values would have J^π values of 2^+, 3^+, 4^+, 5^+, or 6^+. For the decays to the 4819 and 3034 keV levels, classified as *allowed* by the $\log(fT)$ analysis, the possible J^π values from the selections rules are 3^-, 4^-, or 5^-, which is consistent with the adopted levels in the literature since both states were assigned as 3^-.

The 885 keV and ground state levels once again are not consistent with the *allowed* classification from $\log(fT)$ analysis due to their positive parity. These levels would be classified in the same manner described in the previous section. The 2856 keV could be either *allowed* or *first forbidden* based on $\log(fT)$ analysis. The *allowed* classification

Table 3.4: Summary of the decay classifications for the levels in ^{32}Mg if the ^{32}Na ground state is a 4^-. The first four columns correspond to classifications based upon the $\log(fT)$ only, while the last three columns correspond to classifications based upon the change in spin and parity. F corresponds to a Fermi type decay and GT corresponds to a Gamow Teller type.

Classification from $\log(fT)$				Classification from Selection Rules		
E_{level} (keV)	J^π	$\log(fT)$	Classification	ΔJ	$\Delta\pi$	Classification
4819	$(2^-,3^-)$	5.37 (8)	allowed	1,2	no	allowed: GT (1)
						2nd forbidden: F, GT (2)
3034	$(2^-,3^-)$	5.26 (7)	allowed	1,2	no	allowed: GT (1)
						2nd forbidden: F, GT (2)
2856	$(1^-,3^-)$	5.99 (14)	allowed, 1st forbidden	1,3	no	allowed: GT (1)
						3rd forbidden: F, GT (3)
2319	4^+	6.19 (17)	allowed, 1st forbidden	0	yes	1st forbidden: F, GT
885	2^+	$5.36\ ^{8}_{10}$	allowed	2	yes	1st forbidden: GT
						3rd forbidden: F, GT
g.s.	0^+	$5.32\ ^{14}_{16}$	allowed	4	yes	3rd forbidden: F, GT

is more consistent with the adopted levels in ENSDF. Similarly, the 2319 keV would be classified as *first forbidden* since it is known to be a positive parity state. Table 3.4 shows a summary of the classifications for each level.

3.1.3.3 ^{32}Na Ground State Preferred J^π

While both ground state J^π assignments for ^{32}Na show some agreement with the $\log(fT)$ values from the current work, the 3^- assignment is in better agreement with our data. The exception, in this case, is the ground state of ^{32}Mg, which would be required

to be a *3rd forbidden* decay in both cases. Ref. [57] limited the J^π assignments for the ground state of ^{32}Na to $J \leq 4$, but more likely to be a 3^- or 4^-. If the ground state of ^{32}Na happened to be a 2^-, the classifications from the log(fT) values and selection rules would be in complete agreement with the adopted values, including those for the ground state of ^{32}Mg. Thus, we propose that the ground state J^π assignment for ^{32}Na should be 2^- rather than 3^- or 4^- in order to show agreement with the current measurement. However, taking into account the fact that the β-feeding to the ground state of ^{32}Mg is an upper limit due to possible unobserved, less populated levels, we cannot make any definite statement about the J^π assignment for ^{32}Na. Any inconsistency observed in the in the J^π assignment for the ^{32}Mg ground state (based on log(fT) analysis) could be attributed to the Pandemonium effect, which skews the log(fT) classification for the ground state.

3.2 A = 33 Isobars

Included in the NSCL e14063 experiment were the $A = 33$ isobars in the "island of inversion," which includes ^{33}Na, ^{33}Mg, and ^{33}Al. Gating on ^{33}Na yields information about its half-life and decay scheme, as well as information about the γ-ray transitions in the daughter (^{33}Mg) and grand-daughter (^{33}Al). Likewise, gating on ^{33}Mg yields information about its half-life and the transitions in ^{33}Al. This section will focus on the results and discussion for the decay of ^{33}Na and its descendants, as well as the decay of ^{33}Mg to ^{33}Al.

3.2.1 ^{33}Na $\rightarrow$ ^{33}Mg

This section will include the results of the γ-ray, $\gamma - \gamma$ coincidence, and decay curve analysis used to construct the level scheme for ^{33}Mg and decay scheme for ^{33}Na.

3.2.1.1 γ-rays, $\gamma - \gamma$ Coincidences, and Level Scheme

The β-delayed γ-ray spectrum for decays detected within 100 ms for the implantation of a ^{33}Na ion is shown in Fig. 3.7. γ-ray transitions were identified in the daughter nucleus,

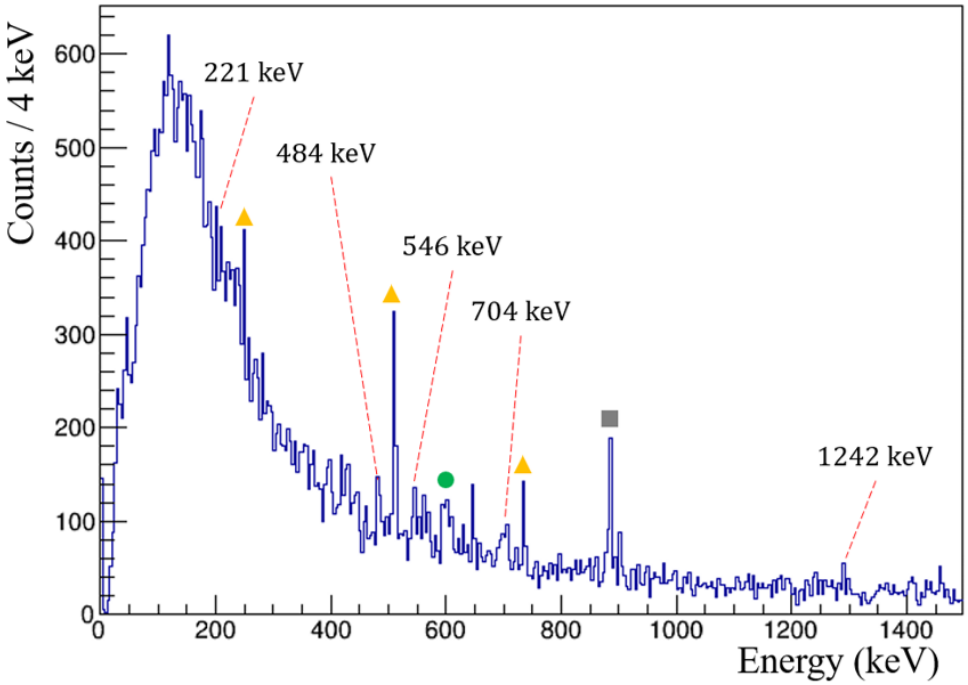

Figure 3.7: The γ-ray singles spectrum in the range of 0 to 1.5 MeV for the decay of ^{33}Na for a correlation time of 100 ms. The transitions labeled in black are γ-rays in ^{33}Mg, transition in the daughter are marked with a green circle, transitions arising from β-n decays are shown with a gray square, and background arising from neighboring isotopes is shown with a yellow triangle.

^{33}Mg, based upon γ-gated β-decay curves, observed $\gamma - \gamma$ coincidences, and the literature. The transitions arising from the decay of ^{33}Na are shown in Table 3.5 along with their respective intensities. In addition to transitions in the daughter, transitions were observed in the grand-daughter and the β-delayed one-neutron and two-neutron daughters, ^{32}Mg and ^{31}Mg, respectively.

The 221.1, 483.7, 545.8, 704.2, and 1242.1 keV transitions are all well-known and previously placed in the level scheme for ^{33}Mg. The 884.6 keV transition corresponds to a transition in ^{32}Mg arising from the β-1n decay of ^{33}Na. The β-2n decay to ^{31}Mg is observed

Table 3.5: Experimentally observed γ-rays from the β-decay of ^{33}Na.

Energy (keV)	$I_{absolute}$ (%)	Decay	Isotope
221.1 (4)	6.2 (10)	β-2n, β	^{31}Mg, ^{33}Mg
483.7 (4)	20.5 (26)	β	^{33}Mg
545.8 (4)	5.9 (12)	β	^{33}Mg
704.2 (4)	14.9 (22)	β	^{33}Mg
884.6 (4)	38.8 (44)	β-n	^{32}Mg
1242.1 (4)	3.8 (12)	β	^{33}Mg

as part of the 221.1 keV yield. The amount of the 221.1 keV yield corresponding to ^{33}Mg was determined by using the literature branching ratio between the 704.2 and 221.1 keV transitions as they de-excite from the same level. This will be discussed in more depth in Section 3.2.1.2.

The $\gamma - \gamma$ coincidence projections for the 221 keV and 484 keV γ-rays are shown in Fig. 3.8(a,b). The 221 keV transition was observed to be in coincidence with the 484 keV transition as shown in Fig. 3.8(b-c). No other coincidences were observed for the transitions in ^{33}Mg. The 484 keV is a well-known transition to the ground state. Both the 221 keV and 704 keV transitions de-excite from the 704.5 (21) level. The 546 keV transition was also previously observed as a ground state transition, and the weakest transition observed in ^{33}Mg was the 1242 keV.

Based upon the γ-ray singles and $\gamma - \gamma$ analysis, the level scheme for ^{33}Mg was constructed and is shown in Fig. 3.9. Of the five transitions observed, all were assigned as transitions to the ground state other than the 221 keV, which was observed to be in coincidence with the 484 keV transition. The spins and parities shown in the constructed level scheme are taken from the adopted levels in the ENSDF database [1]. Ref. [29] limited

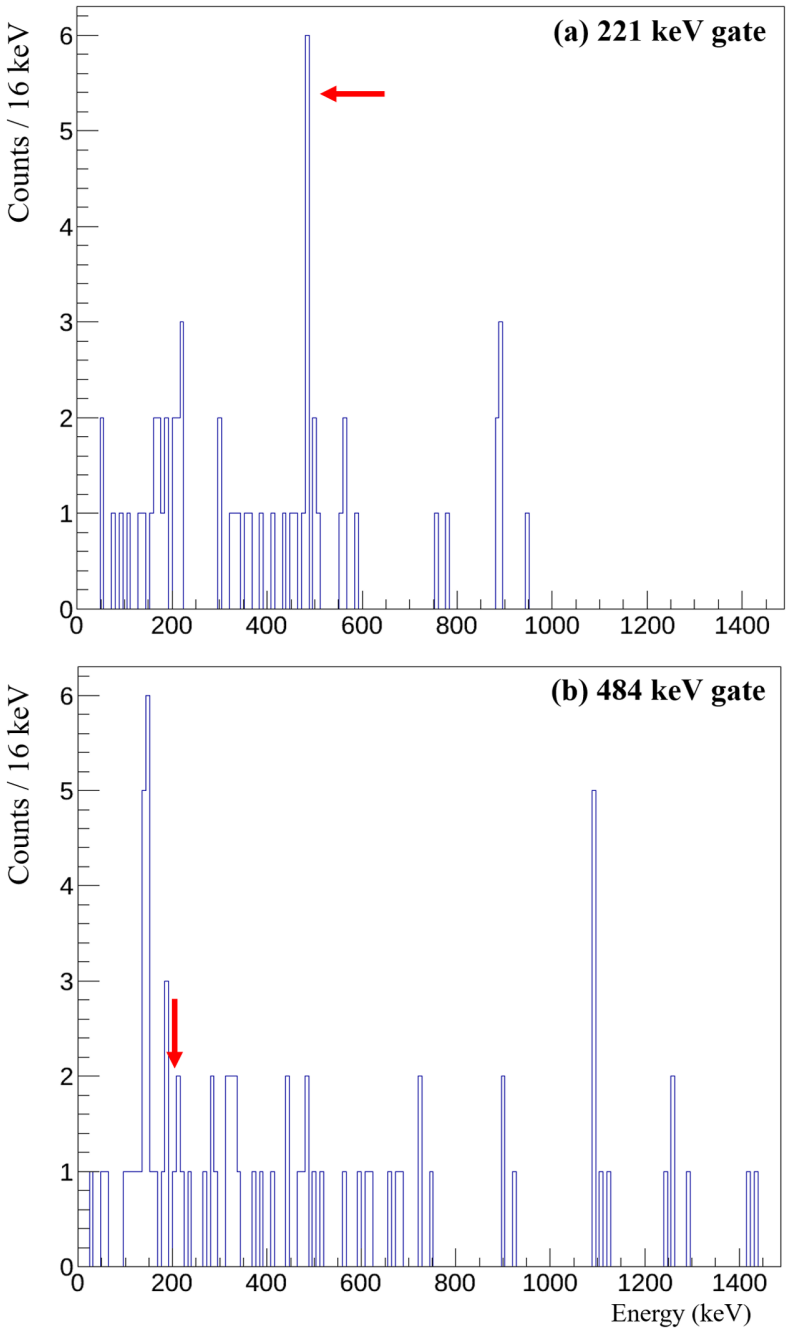

Figure 3.8: The $\gamma - \gamma$ gated projections for the 221 keV (a) and 484 keV (b) transitions in ^{33}Mg.

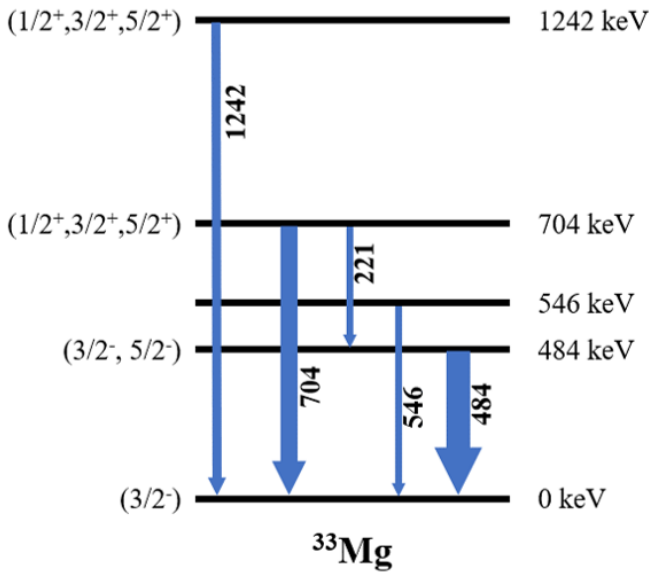

Figure 3.9: The level scheme for ^{33}Mg constructed from γ-ray singles and $\gamma - \gamma$ coincidences.

the J^{π} for the 484 keV level to $3/2^{-}$ based upon shell model calculations, but $\log(fT)$ analysis from their work showed that the level could also have been classified as a $5/2^{-}$. This is in line with arguments from Ref. [35], who stated that the nature of the transition to the ground state was likely of $E2$ nature. The 546 keV level has no proposed J^{π} value in the literature, but possible J^{π} values will be discussed in Section 3.2.1.4. The level scheme from this work is in good agreement with the adopted levels in the literature.

3.2.1.2 Half-life and Decay Scheme

The β-decay curve observed for decays that occurred within 100 ms of the implantation of a ^{33}Na ion in the GeDSSD is shown in Fig. 3.10. The decay curve was using fit in the range of 11 to 100 ms using the Bateman equations and a log-likelihood method. The fit components included the daughter (^{33}Mg), grand-daughter (^{33}Al), β-1n

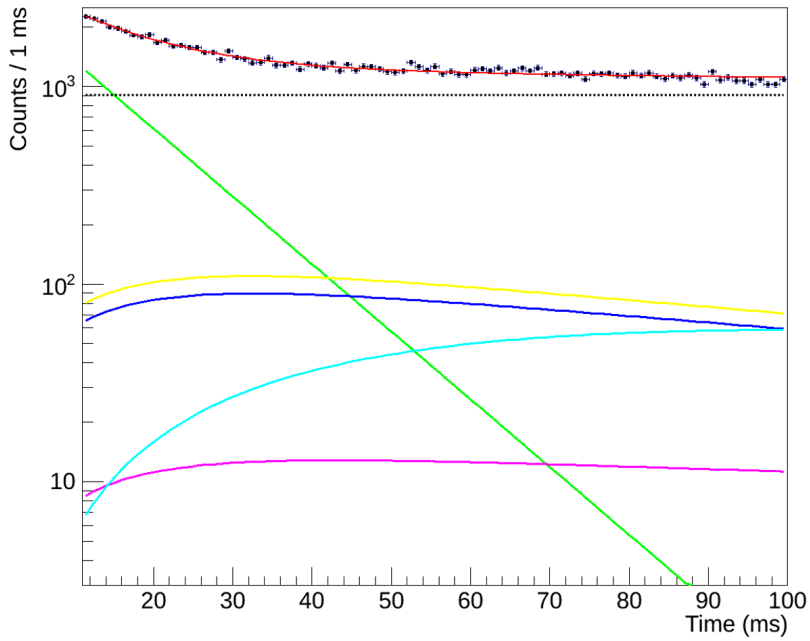

Figure 3.10: The ^{33}Na decay time curve fit with the Bateman equations. The red solid line represents the total fit. The black hashed line is a linear background component, the blue line is the ^{33}Mg daughter decay (from literature), the teal line is the ^{33}Al grand-daughter decay (from literature), the yellow line is the ^{32}Mg β-1n branch, the magenta line is the ^{31}Mg β-2n branch, and the solid green curve is the fit for the ^{33}Na decay only.

(^{32}Mg) and β-2n (^{31}Mg) decays, and a linear background. The literature values were used for the half-lives and parent-neutron branching ratios. The half-lives used were 90.5(16) ms for the daughter (blue), 41.7(2) ms for the grand-daughter (teal), 86(5) ms for the β-1n branch (yellow), and 232(15) ms for the β-2n branch (magenta). The resulting half-life for ^{33}Na was 8.8(4) ms, which is in good agreement with the known half-life of 8.0(4) ms [1]. The γ-gated decay curves for the 484 and 704 keV transitions in ^{33}Mg are shown in Fig. 3.11. The 484 and 704 keV gated decay curves were fit using an exponential with a constant background component and a log-likelihood method, and yield half-life results of 8.3(24) ms and 10.3(39) ms, respectively.

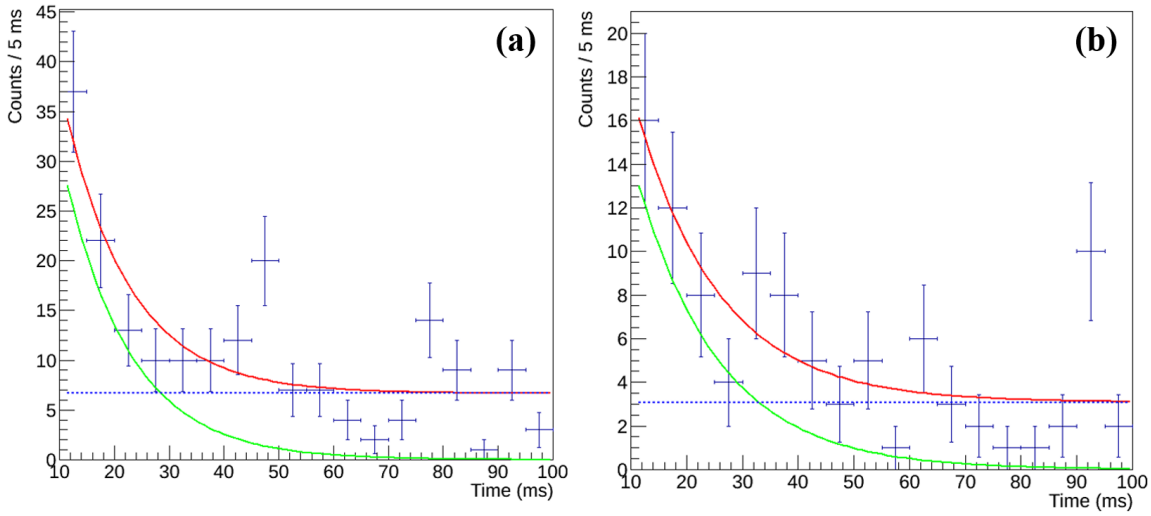

Figure 3.11: The γ-ray gated decay curves along with exponential decay fits for the 484 keV transition (a) and the 704 keV transition (b). The half-life fits are shown in green and are in good agreement with the values from the literature and this work.

From the γ-ray singles, $\gamma - \gamma$ analysis, and literature arguments, the decay scheme for ^{33}Na was constructed and is summarized in Table 3.6. Fig. 3.12 shows the decay scheme for the current work using the literature branching ratios. The total number of ^{33}Na decays was 15781 ± 126, which was obtained via integration of the ^{33}Na parent curve. As with the case of ^{32}Na, the feedings to each level were calculated along with the log(fT) values.

3.2.1.3 Classification Based on log(fT) Values

The 1242 keV and 704 keV levels have feeding intensities of 2.3(17)% and 12.6(14)%, respectively. These feedings result in log(fT) values of 5.94 (16) and 5.26 (9), which fall within the *allowed* decay range. The log(fT) value for the 1242 keV level could also be classified as a *first forbidden* decay. The 546 keV level has no tentative J^{π} values in the literature and its placement has faced some uncertainty. The ENSDF adopted levels place it as a ground state transition, which is what was adopted in the current work. The

Table 3.6: Summary of the decay scheme β-decay feeding intensity parameters and error estimations for ^{33}Na including the literature β-n branches.

E_{Level} (keV)	In	Out	Decays	I_β (%)	log(fT)
1242.1 (17)	decays	362 ± 109	362 ± 109	2.3 ± 0.7	5.94 ± 0.16
704.8 (21)	decays	1987 ± 214	1987 ± 214	12.6 ± 1.4	5.26 ± 0.09
545.8 (24)	decays	560 ± 110	560 ± 110	3.5 ± 0.7	5.84 ± 0.12
483.7 (13)	decays + 580 ± 92	1933 ± 214	1353 ± 233	8.6 ± 1.5	5.46 ± 0.11
^{32}Mg				47.0 ± 6.0	
^{31}Mg				13.0 ± 3.0	
g.s.	decays + 4260 ± 327	0		13.0 ± 6.6	5.33 ± 0.25

feeding intensity to this level was 3.5 (7)%, resulting in an *allowed* decay with a log(fT) of 5.84 (12). The 484 keV level is tentatively a $\frac{3}{2}^-$ or $\frac{5}{2}^-$ state with β feeding intensity of 8.6 (15)%, which is another *allowed* decay with a log(fT) of 5.46 (11).

The β-1n branch to ^{32}Mg is fed via decays and has a strong transition at 885 keV de-exciting. The observed feeding intensity was 23.1(23)% for this experiment. The β-2n decay to ^{31}Mg proved to be more complicated as the only transition that was observed was the 221 keV, for which the bulk of the intensity was associated with ^{33}Mg. In order to determine the intensity of the 221 keV transition in ^{33}Mg, the literature branching ratio between the 221 and 704 keV γ-rays de-exciting the 704 keV level was used [29]. From Ref. [29], the 221 keV yield should be 37.5 (55)% of the 704 keV yield. The experimental yield of the 704 keV was 1410 (193) counts, which means the 221 keV yield should have been 528 (106) counts. The observed experimental yield for the 221 keV γ-ray was 580 (92), therefore, the yield to the 221 keV γ-ray in ^{31}Mg was 52 (140) counts. This yields a feeding intensity of 0.3 (9)%.

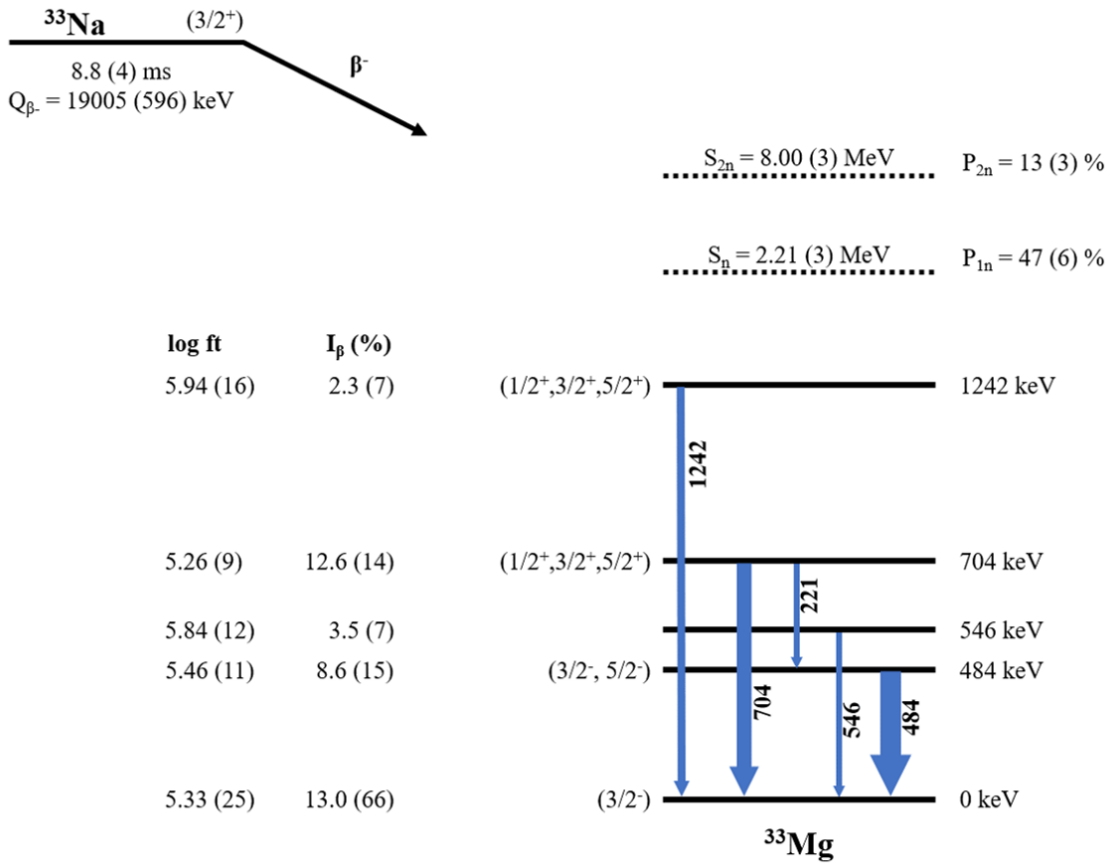

Figure 3.12: The decay scheme for ^{33}Na showing the feeding intensity and log fT values for each level in ^{33}Mg. The neutron branching fractions are shown as the values adopted in the literature [26, 30].

However, since the current work was not sensitive to neutrons, these values are lower limits. Refs. [26, 30] measured neutrons to obtain β-1n and β-2n fractions of 47 (6)% and 13 (3)%, respectively. Using these parent-neutron branching fractions, the feeding intensity to the $\frac{3}{2}^-$ ground state of ^{33}Mg was 13.0 (66)%, resulting in a log(fT) of 5.33(25) making it consistent with an *allowed* decay.

3.2.1.4 Discussion of the ^{33}Na Decay Scheme and ^{33}Mg Level Scheme

The ground state of ^{33}Na has a tentative J^π of $\frac{3}{2}^+$ based upon the systematics of odd Na nuclides and β-feedings from previous measurements [1, 30, 61]. From the selection rules, an *allowed* decay from a $\frac{3}{2}^+$ g.s. would populate J^π values of $\frac{1}{2}^+$, $\frac{3}{2}^+$, or $\frac{5}{2}^+$. Decays classified as *first forbidden* would have potential J^π assignments of $\frac{1}{2}^-$, $\frac{3}{2}^-$, $\frac{5}{2}^-$, or $\frac{7}{2}^-$. From $\log(fT)$ analysis, the 1242 keV level could be classified as *allowed*, and therefore has possible J^π values of $\frac{1}{2}^+$, $\frac{3}{2}^+$, or $\frac{5}{2}^+$. This is consistent with the adopted values in the literature. The 704 keV level is also classified as *allowed* based upon the $\log(fT)$, which is in good agreement with the tentative J^π in the literature. The 546 keV level could be either *allowed* or *first forbidden* based on the $\log(fT)$, so the possible J^π values could be any of the positive or negative parity states mentioned above. Without further information, the 546 keV cannot be given a definite J^π assignment.

The 484 keV and ground state levels are both classified as *allowed* by their $\log(fT)$ values, which means their possible J^π values are $\frac{1}{2}^+$, $\frac{3}{2}^+$, or $\frac{5}{2}^+$. However, since these two levels are fairly well-established negative parity states, decays to these levels would be classified as *1st forbidden*. This is a reasonable classification considering that the $\log(fT)$ ranges are not rigid and when the values are close to the boundaries of the *allowed* and *first forbidden* range, the decay could be of either type. Additionally, accounting for the Pandemonium effect, the inconsistency between $\log(fT)$ analysis and adopted J^π values makes sense because of the possible unobserved intensity attributed to less populated levels. Table 3.7 shows a summary of the classifications for each level.

3.2.2 ^{33}Al

The properties of ^{33}Al, the next of the A=33 isobars, can be studied in two ways. The first is through the direct decay of ^{33}Mg and the second is via the daughter decay of ^{33}Na. Both cases will be discussed in this section. However, due to poor statistics in this region,

Table 3.7: Summary of the decay classifications for the levels in ^{33}Mg when the ^{33}Na ground state is a $\frac{3}{2}^+$. The first four columns correspond to classifications based upon the log(fT) only, while the last three columns correspond to classifications based upon the change in spin and parity. *F* corresponds to a Fermi type decay and *GT* corresponds to a Gamow Teller type.

Classification from log(fT)				Classification from Selection Rules		
E_{level} (keV)	J^π	log(fT)	Classification	ΔJ	$\Delta\pi$	Classification
1242	$(\frac{1}{2}^+, \frac{3}{2}^+, \frac{5}{2}^+)$	5.94 (16)	allowed	0,1,2	no	allowed: F, GT (0,1)
						2nd forbidden: F, GT (2)
704	$(\frac{1}{2}^+, \frac{3}{2}^+, \frac{5}{2}^+)$	5.26 (9)	allowed	0,1,2	no	allowed: F, GT (0,1)
						2nd forbidden: F, GT (2)
546		5.84 (12)	allowed, 1st forbidden			
484	$(\frac{3}{2}^-, \frac{5}{2}^-)$	5.46 (11)	allowed	0,1	yes	1st Forbidden: F, GT
0	$(\frac{3}{2}^-)$	5.33 (25)	allowed	0	yes	1st Forbidden: F, GT

the results are limited to the half-life and γ-ray singles for the direct decay and only γ-ray singles for the ^{33}Na decay.

3.2.2.1 ^{33}Na $\rightarrow$ ^{33}Mg $\rightarrow$ ^{33}Al

Based upon the half-life curve fit shown in Fig. 3.10 and expanded in Fig. 3.13, gates were placed on the decay time between 45 ms and 270 ms where the ^{33}Al curve (teal) is more dominant in order to enhance the γ-rays coming from ^{33}Al. The following transitions were observed to belong to ^{33}Al based upon what is known in the literature [1]: 594.4, 1617.6, 1835.7, 2096.7, 2366.6 keV. Table 3.8 shows the transitions along with their respective intensities. The 1617.6 keV transition was observed as the most intense and although the statistics were not substantial enough to complete a $\gamma - \gamma$ analysis for this case, it was placed as a g.s. transition (shown in Fig. 3.14).

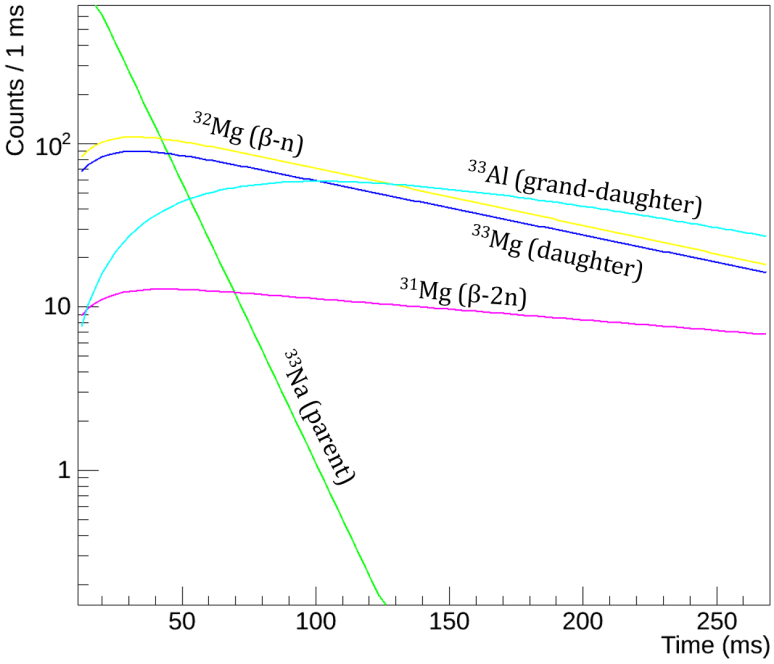

Figure 3.13: An expanded version of Fig. 3.10 to emphasize the regions where certain contributions to the total half-life dominate. The blue line is the ^{33}Mg daughter decay component, the teal line is the ^{33}Al grand-daughter decay, the yellow line is the ^{32}Mg β-1n branch, the magenta line is the ^{31}Mg β-2n branch, and the solid green curve is the fit for the ^{33}Na decay only.

Table 3.8: Experimentally observed γ-rays in ^{33}Al from the β-decay of ^{33}Mg following the decay of ^{33}Na between 45-270 ms.

Energy (keV)	$I_{absolute}$ (%)
594.4 (4)	14.3 (26)
1617.6 (4)	38.8 (61)
1835.7 (4)	23.4 (45)
2096.7 (4)	18.3 (40)
2366.6 (4)	5.2 (21)

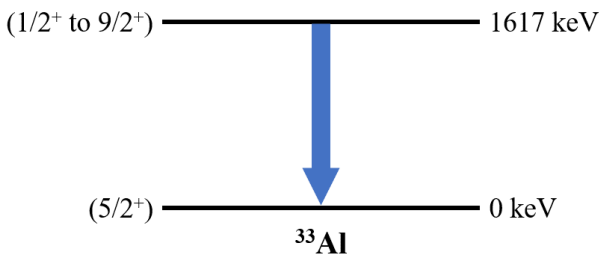

Figure 3.14: The level scheme for ^{33}Al constructed from the intensity of the 1617 keV γ-ray and literature information.

3.2.2.2 ^{33}Mg $\rightarrow$ ^{33}Al

Table 3.9: Experimentally observed γ-rays in ^{33}Al from the β-decay of ^{33}Mg.

Energy (keV)	$I_{absolute}$ (%)
596.3 (4)	13.6 (32)
1616.6 (4)	47.5 (88)
2096.1 (4)	33.2 (74)
2366.2 (4)	5.6 (28)

A gate was placed on ^{33}Mg in the PID in order to directly study the decay to ^{33}Al. The statistics were poor for this case, but the γ-ray singles and decay curve were analyzed. γ-rays resulting from the decay of ^{33}Mg to ^{33}Al are summarized in Table 3.9 and were 596.3, 1616.6, 2096.1, and 2366.2 keV. Each of these transitions was also observed in the decay of ^{33}Na and correspond to the strongest transitions in ^{33}Al. Fig. 3.15 shows the decay time

curve for ^{33}Mg along with the half-life fit. The fit components include the grand-daughter half-life of 41.7 (2) ms (shown in blue), the half-life of ^{32}Al (β-1n) (shown in yellow), and a linear background. The β-1n decay branching fraction was taken from the literature to be 14 (2)% and the ^{32}Al half-life was 33.0 (2) ms [1]. The half-life for ^{33}Mg extracted from the fit was 83.7 (255) ms, which is in agreement with the adopted value of 90.5 (16) ms.

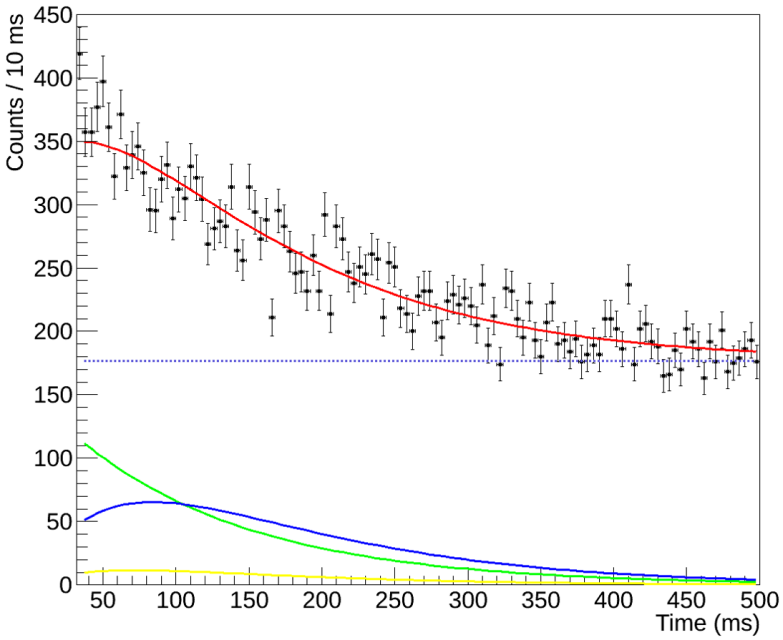

Figure 3.15: The ^{33}Mg decay time curve fit with the Bateman equations. The red solid line represents the total fit. The violet hashed line is a linear background component, the blue line is the ^{33}Al daughter decay (from literature), the yellow line corresponds to the ^{32}Al following β-1n decay, and the solid green curve is the fit for the ^{33}Mg decay only.

Of the four γ-rays observed in ^{33}Al, only the 1616.7 keV transition had enough statistics to be fit as a γ-gated decay curve, which is shown in Fig. 3.16. The fit included a linear background and the resulting half-life was 95.9 (202) ms, which is in agreement

with the literature value for ^{33}Mg. Based upon the intensities of the transitions observed in ^{33}Al, the first excited state at 1617 keV was placed and is shown in Fig. 3.14.

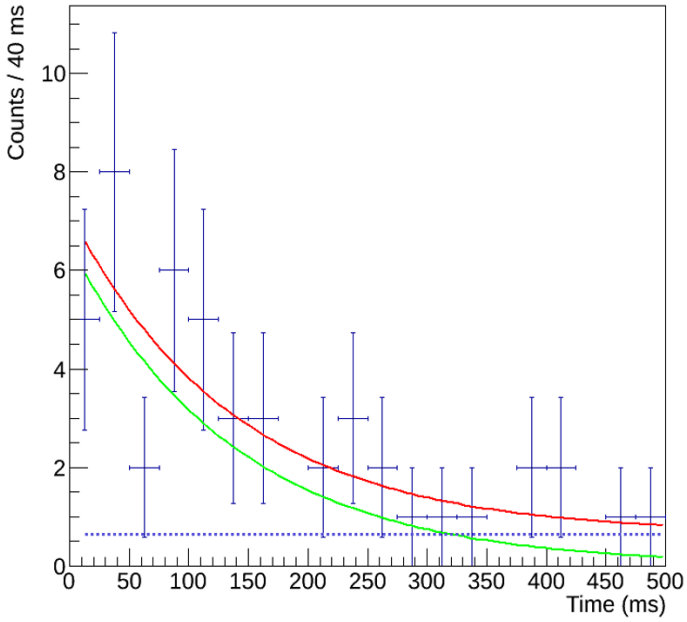

Figure 3.16: The γ-ray gated decay curve along with exponential decay fit for the 1616.7 keV transition in ^{33}Al. The extracted half-life is in good agreement with the literature value.

4 E11029 Results and Discussion

Following the secondary fragmentation of ^{46}Ar, neutron-rich isotopes were identified on an event-by-event basis through their energy loss (ΔE), total kinetic energy (E), and time-of-flight (TOF) as measured in the S800 focal plane detector suite [48, 49], and excited state γ-decays were observed using the γ-ray tracking array GRETINA (Gamma Ray Energy Tracking In-beam Nuclear Array) [62]. The technique adopted in this experiment involves the removal of a large number of nucleons from the secondary beam, which provides a mechanism for populating higher angular momentum (J) states, especially when compared to few nucleon removal reactions. The removal of 13 nucleons from the secondary radioactive beam of ^{46}Ar was used to produce ^{33}Mg. The e11029 experimental setup was described in Chapter 2, along with the details of the S800 Focal Plane Detector calibrations, GRETINA efficiency determination, and Doppler correction procedures. This chapter will focus on the results of this measurement of ^{33}Mg, identification of a low-lying rotational band structure in this isotope, and the interpretation of this structure in the framework of the rotational model.

4.1 γ-ray Analysis

The γ-rays associated with ^{33}Mg were analyzed in a γ-ray singles and $\gamma-\gamma$ coincidence analysis. The energy of each γ-ray was determined by fitting each peak in the singles spectrum with a Lorentzian distribution plus a linear background and coincidences were established from gated projections of the $\gamma-\gamma$ matrix. The intensity of each transition was determined from integration of the peak area followed by a detection efficiency correction. The level scheme was constructed based on all of the available experimental information. This section describes the γ-ray singles and $\gamma-\gamma$ analysis.

The γ-ray singles spectrum observed in GRETINA in coincidence with identified ^{33}Mg residues (using E-ΔE particle identification) is shown in Figure 4.1. As previously

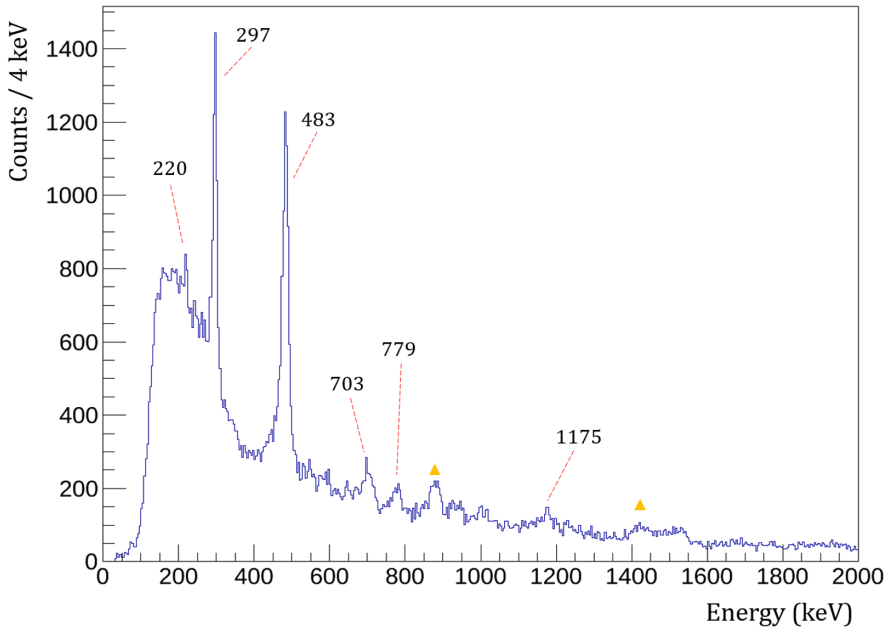

Figure 4.1: The Doppler reconstructed γ-ray singles spectrum of ^{33}Mg detected with GRETINA (using clustering) following the secondary fragmentation of the beam. Transitions in ^{33}Mg are marked with their energies in black; the transitions marked with a yellow triangle correspond to γ-rays in the neighboring isotope, ^{32}Mg. The transition at 1175 keV corresponds to a weak, unplaced transition in ^{33}Mg. The spectrum, shown here, includes data satisfying the E-ΔE gate only.

discussed in Chapter 2, the E-ΔE measurement that was used to cleanly identify ^{33}Mg nuclei was only possible for a portion of the data, and the E-ΔE gate in conjunction with time-of-flight cuts was used in the case where E-ΔE data were not available. However, the ΔE-TOF gates brought in more background from neighboring isotopes, which is visible in Figure 4.2, where data for the E-ΔE and ΔE-TOF methods are compared. The spectrum with contributions from both particle identification methods shows particular enhancement of transitions in ^{32}Mg, which are denoted by yellow triangles. For the remainder of

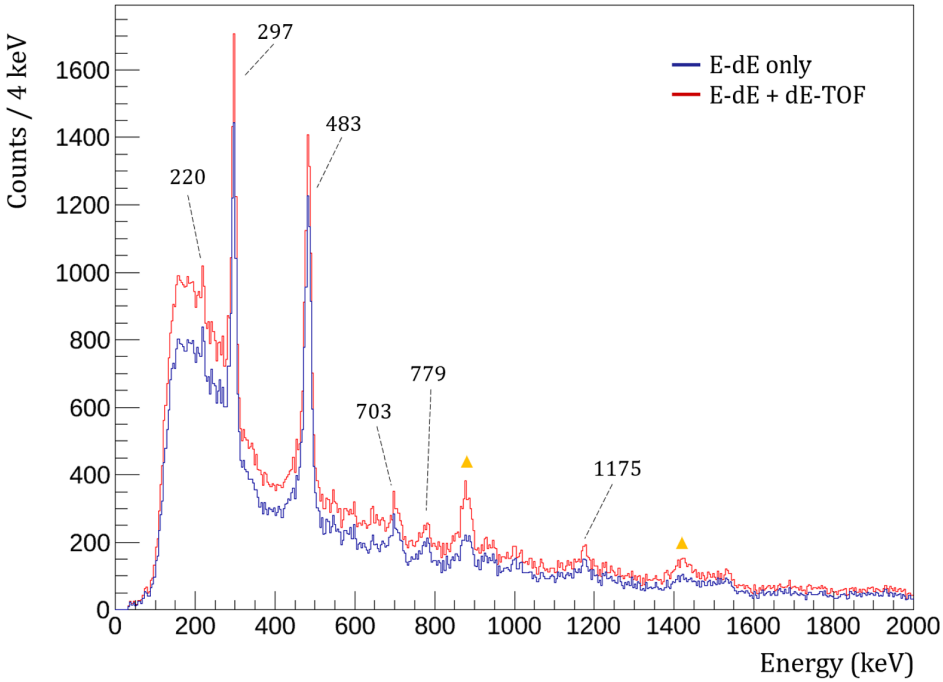

Figure 4.2: The comparison of the γ-ray singles spectra for the E-dE data (blue) and the summed E-ΔE and ΔE-TOF (red) for ^{33}Mg. The background coming from the ^{32}Mg neighbor (yellow triangles) is enhanced for the red spectrum as compared to the blue. This is due to the overlapping time-of-flight distributions for each isotope (see Chapter 2, Section 2.3.2.3).

the analysis described in this chapter, only the E-ΔE gates were used in order to limit contamination from the neighboring isotopes.

In the singles spectrum, two strong transitions are observed at 297(4) and 483(4) keV with three weak transitions at 220(4), 703(4), and 779(4) keV. The 220, 483, and 703 keV transitions correspond to γ-rays observed and placed in our β-decay work as well as in previous works [26, 29, 35–38]. The ground state of ^{33}Mg is well established as a $3/2^-$ [34] based on laser spectroscopy and nuclear magnetic resonance measurements. The 483 keV γ-ray is a known ground state transition as is the 703 keV γ-ray [26, 29]. The 220 keV

has been established in the literature to be in coincidence with the 483 keV transition [29], depopulating the 703 keV state. The 297 keV γ-ray was previously observed very weakly in an early β-decay study [29] but was not placed in the level scheme. The 779 keV was not previously reported.

A weak transition was also observed in the present work at 1175(4) keV but was not placed in the level scheme for ^{33}Mg. No additional transitions in ^{33}Mg were observed above 1.2 MeV. The relative intensity of each peak was determined from integration of the peak area and corrected for the detection efficiency accounting for the Lorentz boost (boosted efficiency). The boosted efficiency for each γ-ray is shown in Table 4.1.

Table 4.1: Boosted efficiency for each γ-ray in ^{33}Mg.

E_γ (keV)	Boosted Efficiency (%)
220	9.4
297	8.3
483	6.6
703	5.4
779	5.1
1175	4.4

A $\gamma - \gamma$ coincidence matrix was constructed for ^{33}Mg for γ-multiplicities of 2 and is shown in Figure 4.3. Gates were placed on each transition from the singles spectrum and the coincidences were established. Figure 4.4 shows the projection of the (a) 297 keV and (b) 483 keV γ-rays. In this work, the 297 keV is shown to be in coincidence with the 483 keV transition, and based on this coincidence relationship, and the observation of a weak transition at 779 keV, a new level is placed at 780(6) keV. The 220 keV was

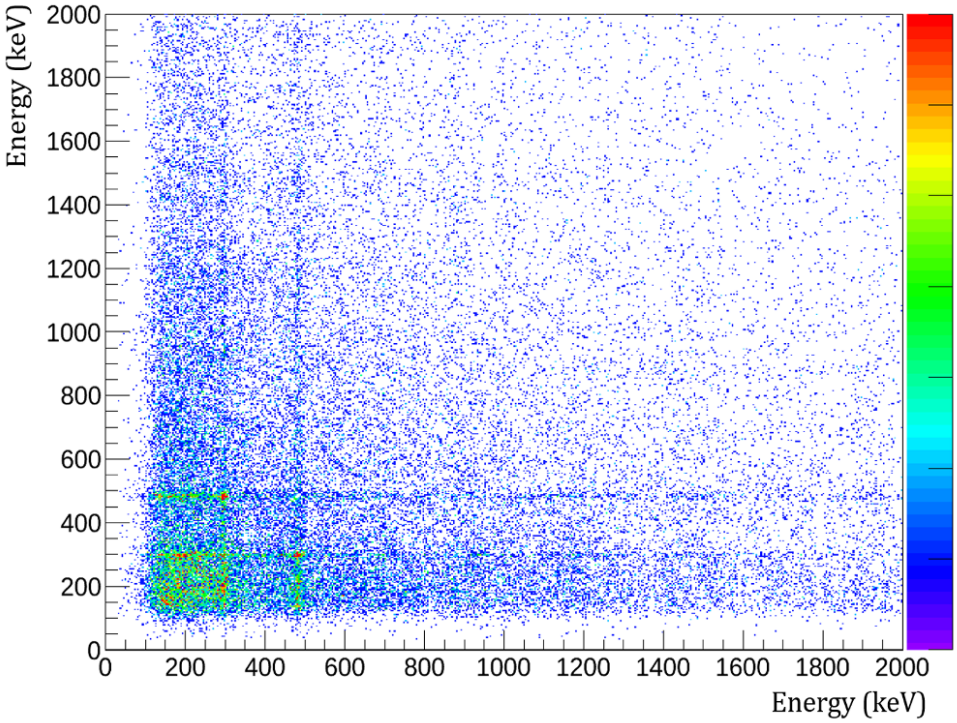

Figure 4.3: The $\gamma - \gamma$ matrix for ^{33}Mg was used to establish coincidences between γ-rays in the singles spectrum.

also observed to be in coincidence with the 483 keV transition, de-exciting from the 703 keV level. This is in good agreement with the adopted level scheme for ^{33}Mg. The previously mentioned weak transition at 1175 keV did not have the statistics and showed no coincidence relations. It could not be placed in the level scheme. The level scheme established in this work is shown in Figure 4.5. The ^{33}Mg experimental level energies, γ-ray energies, and tentative spin assignments (based upon the literature and arguments in the following sections) are summarized in Table 4.2.

The remaining sections of this chapter offer an interpretation of the experimental level scheme, γ-ray intensities, and excitation energies in a leading order rotational

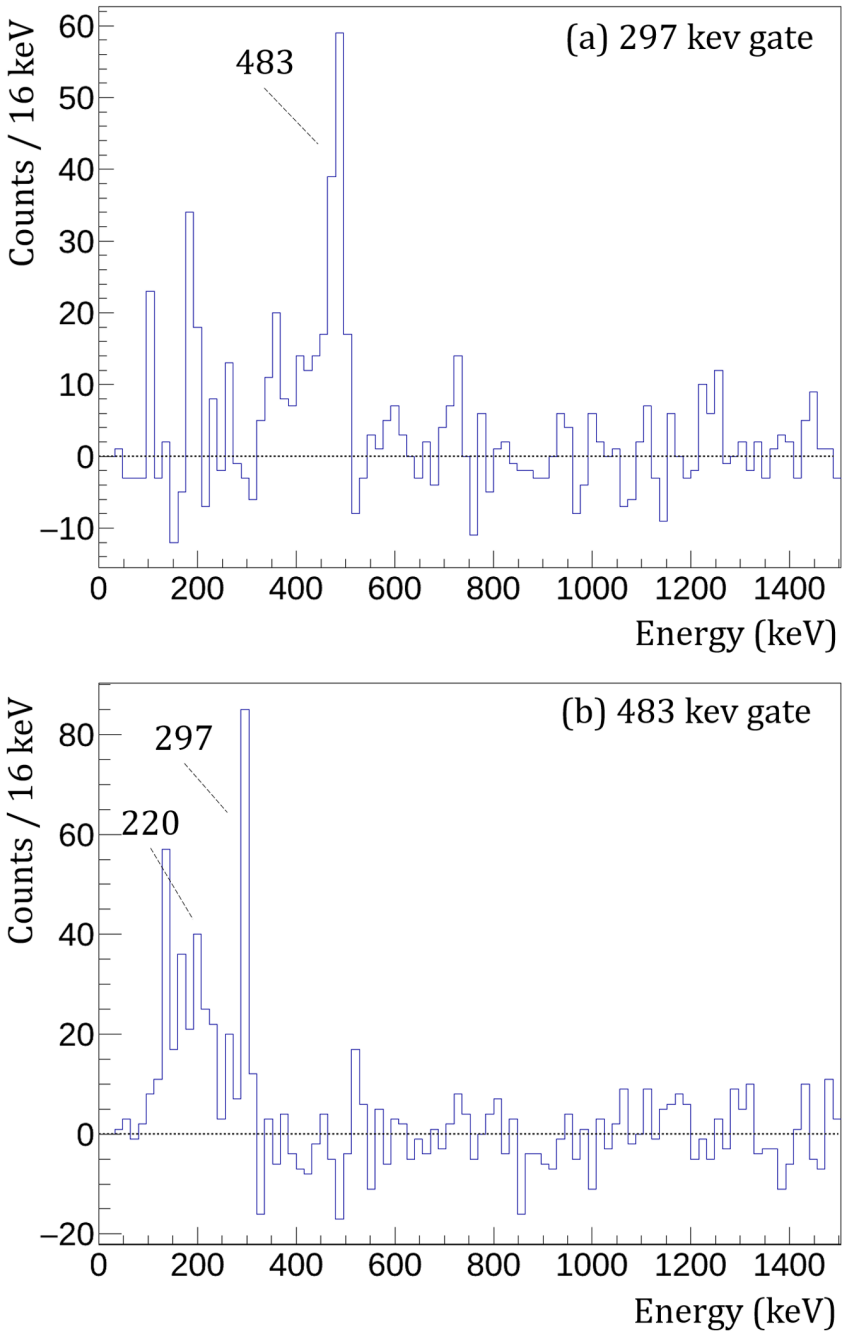

Figure 4.4: The $\gamma - \gamma$ projections of the (a) 297 keV and (b) 483 keV γ-ray transitions. Clear coincidence is observed between the 297 keV and 483 keV transitions. The 483 keV also shows coincidence with the 220 keV transition.

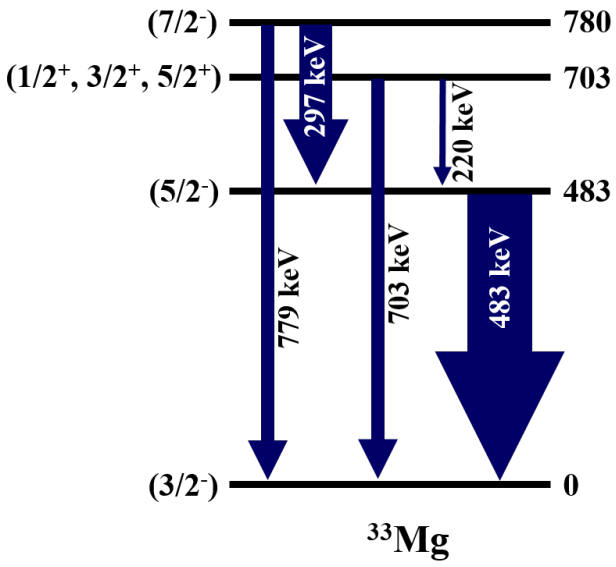

Figure 4.5: The level scheme of ^{33}Mg based upon γ-ray singles, $\gamma - \gamma$ coincidence data, and literature placements. The width of the arrows is representative of the relative intensity of the transition. All γ-ray transitions were measured with 4 keV uncertainty.

framework. Other available experimental observables such as $B(E2)$ and magnetic moment, μ, measurements will also be discussed within this model.

4.2 Discussion of ^{33}Mg Level Scheme

An intuitive way to describe the structure of ^{33}Mg is think of it as a ^{32}Mg core plus a valence neutron (or a ^{34}Mg core plus a valence neutron hole). The low-lying yrast structure in ^{32,34}Mg can be described as a rotational band [36, 63–65] and the extension of this description to the odd system in ^{33}Mg will provide further insight into the deformation in this region. It is well known that rotational bands have certain regularities in their energy spectra and intensity relations that govern transitions within the band. To this end, the low-energy excitation energies, γ-ray intensities, and other available data for ^{33}Mg are compared

Table 4.2: Experimental level information for the low-lying states in ^{33}Mg as populated in the present work. Spin/parity assignments are tentative.

Initial State (keV)	J^π	Final State (keV)	J^π	E_γ (keV)	I_γ (rel. %)
780(6)	$^7/_2^-$	0	$^3/_2^-$	779(4)	12(4)
780(6)	$^7/_2^-$	483(4)	$^5/_2^-$	297(4)	48(13)
703(4)		0	$^3/_2^-$	703(4)	13(4)
703(4)		483(4)	$^5/_2^-$	220(4)	8(2)
483(4)	$^5/_2^-$	0	$^3/_2^-$	483(4)	100
				1175(4)	18(6)

to a leading order rotational interpretation of the nucleus as a neutron strongly coupled to a deformed core.

In deformed, odd-A systems, rotational bands have low-lying states can be classified by $J = K, K+1, K+2, ...$, where J is the spin of a particular level and K is the angular momentum of the bandhead. As introduced in Chapter 1, K is defined as the projection of the total angular momentum onto the nuclear symmetry axis. The relationship between the rotational energy of the odd-neutron and the excitation energy of the deformed core is known as the coupling. There are two extremes that describe how the odd particle couples to the core, known as the strong coupling limit or the decoupled limit. For the current work, we assume ^{33}Mg can be described as a strongly coupled rotational band and compare the experimental observables to this description. This is justified since the rotational energy arising from Coriolis coupling is small compared to the excitation energies observed in ^{32}Mg (the core). Furthermore, the strong coupling limit usually corresponds to larger deformations, which is what has been suggested in this region.

For this analysis, we assume a $K = 3/2$ bandhead, arising from an unpaired neutron in the Nilsson 3/2[321] orbital (see Fig. 1.6). This is in line with the $3/2^-$ ground state adopted from the ground state magnetic moment determination [34, 66]. Building a strongly coupled rotational band on level, the levels at 483 keV and 780 keV correspond to the second and third members of the band and thus are tentatively assigned J^π values of $5/2^-$ and $7/2^-$, respectively. These assumptions are supported by the strong population of these states in the current work, which is expected to favorably populate the yrast levels of ^{33}Mg, as was observed in ^{32}Mg [63]. Additionally, from Ref. [35], the 483 keV is expected to favor an $E2$ type transition, which would make the J^π a $5/2^-$ despite the adopted value of $3/2^-$ from ENSDF. This is also in line with the observations of our β-decay work.

In the following sections, the excitation energies in ^{32,33,34}Mg will be compared to leading order relations in the strong coupling limit. Then, the available electromagnetic observables, specifically the $E2$ to $M1$ γ-ray intensity ratio depopulating the proposed $7/2^-$ state, intrinsic quadrupole moment derived from a measured $B(E2\uparrow)$, and ground state magnetic moment will be tested in the strong coupling limit using leading order relations.

4.2.1 Excitation Energies

The experimental excitation energies provide a first test of the leading order description for ^{33}Mg in the strong coupling limit. To begin, the excitation energies for ^{32,34}Mg are determined at leading order. These relationships were described in Chapter 1, but are included again for completeness. For low-lying states (small J), the rotational energy for an even-even nucleus can be expanded and written as

$$E_J = AJ(J+1) + BJ^2(J+1)^2 + ... \tag{4.1}$$

Within a band, A is equivalent to $\hbar^2/2\mathscr{I}$, where $\mathscr{I}$ is the moment-of-inertia, and B represents a first-order correction describing the dependence of the moment-of-inertia on J.

Table 4.3: Experimental level information for states in ^{32}Mg, ^{33}Mg, and ^{34}Mg.

^{32}Mg		^{33}Mg		^{34}Mg	
J^π	Energy (keV)	J^π	Energy (keV)	J^π	Energy (keV)
0^+	0 (4)	$^3/_2^-$	0 (4)	0^+	0
2^+	886 (4)	$^5/_2^-$	483 (4)	2^+	660 (7)
4^+	2324 (4)	$^7/_2^-$	780 (4)	(4^+)	2120 (22)
6^+	4097 (4)				

Inclusion of B in the present analysis is justified even though it is not a leading order term due to the fact that analysis of the rotational structure of ^{32}Mg (from the current experiment) showed the presence of a variable moment-of-inertia (VMI). That is, the moment-of-inertia for ^{32}Mg varies as a function of J (see Ref. [63] for further details). The purpose in testing the excitation energies is to obtain values for A and B for the core and to compare them to the values found for ^{33}Mg.

Table 4.3 shows a summary of the experimental level information for ^{32}Mg and ^{33}Mg from the current measurement and for ^{34}Mg from previous work. Past experimental data on the rotational nature of ^{32}Mg showed four levels in the ground state rotational band, namely a 0^+ state, a 2^+ state at 886 (4) [63, 65, 67–70], a 4^+ at 2324 (6) [63, 71], and a 6^+ at 4097 (7) [63]. From these energies and spin assignments, the experimental excitation energies were fit using Eq. 4.1. The values and fit are shown in Fig. 4.6, and A and B were found to be 141.5(5) keV and -1.06(1) keV, respectively.

Following the same analysis for the levels in ^{34}Mg, namely a 0^+, a 2^+ at 660 (7) keV [36, 37, 64, 65], and a tentative 4^+ at 2120 (22) keV [36, 64, 65], we obtain

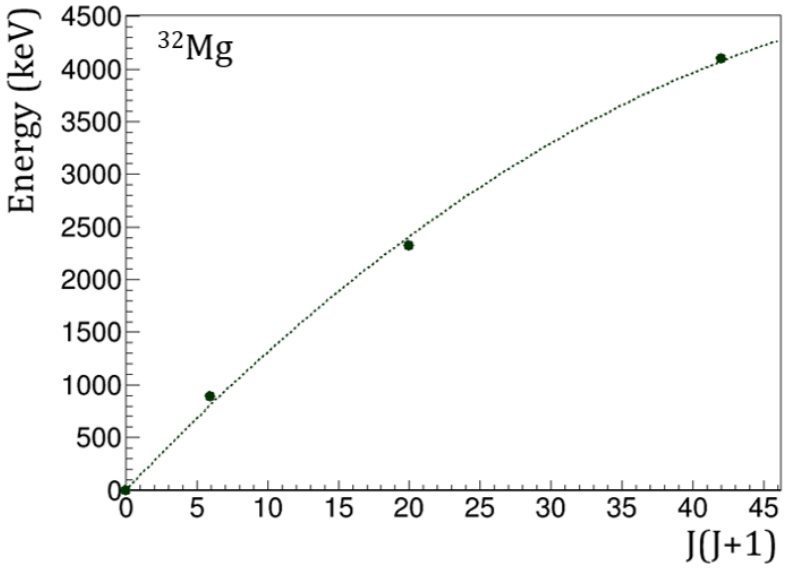

Figure 4.6: The excitation energies as a function of $J(J+1)$ for ^{32}Mg. The results are fit to Eq. 4.1.

A = 111.6 (17) keV and B = -0.27 (11) keV. These smaller values for A and B indicate a slightly larger deformation in ^{34}Mg, but an overall consistent picture of these two nuclei.

In order to consider the odd-A neighbor, ^{33}Mg, an additional term arising from the Coriolis coupling interaction must be added to the rotational energy shown in Eq. 4.1. This term is shown in Eq. 1.16. For a $K = 3/2$ bandhead, the total rotational energy at leading order can be written as

$$E(K,J) = AJ(J+1) + BJ^2(J+1)^2 + (-1)^{J+\frac{3}{2}}(J-\frac{1}{2})(J+\frac{1}{2})(J+\frac{1}{2})A_3, \qquad (4.2)$$

where A_3 represents the Coriolis interaction strength for $K = 3/2$. This functional form is expanded from Eq. 1.18.

With the assumption that the 483 keV and 780 keV levels are the second and third members of the rotational band and using Eq. 4.2, we obtain values of A = 109.9(1) keV,

B = -1.90(4) keV, and A_3 = 1.74(6) keV. The value of A for ^{33}Mg is reduced by 22% from that in ^{32}Mg. This is in good agreement with the expectation of pair-blocking by the odd-neutron reducing the pairing correlations in the core and resulting in a larger moment-of-inertia. As an example of pair-blocking, consider the neutron $0f_{7/2}$ orbital, ^{32}Mg has four pairs available to scatter whereas ^{33}Mg has one neutron occupying the orbital and reduces the number of pairs to three. The reduction from four pairs to three reduces the moment-of-inertia on the order of 20%, which is observed in the current analysis.

Furthermore, the consistency of this picture can be further validated by calculating the expected value for A_3 directly. From the intrinsic rotational Hamiltonian, $A_3 = \langle 3/2|h_3|\overline{3/2}\rangle$ [22]. This can be expanded as

$$A_3 = -A^3 \frac{\langle 3/2|j_+|1/2\rangle\langle 1/2|j_+|\overline{1/2}\rangle\langle\overline{1/2}|j_+|\overline{3/2}\rangle}{(E_{1/2} - E_{3/2})^2}. \tag{4.3}$$

Then using the Nilsson model [21, 72], described in Chapter 1, we can calculate the values of $\langle 3/2|j_+|1/2\rangle$, $\langle 1/2|j_+|\overline{1/2}\rangle$, $\langle\overline{1/2}|j_+|\overline{3/2}\rangle$, $E_{1/2}$, and $E_{3/2}$ at a particular value of the deformation ε_2. For a deformation of ~0.5, $\langle 3/2|j_+|1/2\rangle = \langle\overline{1/2}|j_+|\overline{3/2}\rangle = 3.113$, $\langle 1/2|j_+|\overline{1/2}\rangle = 2.721$, $E_{1/2} = 3.47\hbar\omega_0$, and $E_{3/2} = 3.82\hbar\omega_0$. We obtain $A_3 \approx 1.75$ keV, which agrees well with the A_3 value from the experimental energy levels. The overall agreement with the experimental energy sequences suggests that to leading order, the rotational model provides a reasonable description of the states in ^{33}Mg (with the tentative spin and parity assignments in Table 4.2).

4.2.2 B($E2$), Magnetic Moment, and Intensity Ratio

The strong coupling limit of the rotational model can be used to make predictions about electromagnetic observables such as transition rates and nuclear moments. These quantities provide an additional way to test ^{33}Mg in a leading order rotational framework. The available experimental observables for ^{33}Mg are the ratio of the γ-ray intensities

depopulating the $(7/2^-)$ state, the ground-state magnetic moment, μ [34], and the Q_0 derived from a measured $B(E2)$ [35].

The ratio of the γ-ray intensities between the $E2$ and $M1$ transitions depopulating the candidate $(7/2^-)$ state is denoted as λ. For a $K \neq 1/2$ band, λ can be written in terms of the γ-ray energies (in MeV), the g-factors (g_K and g_R), and the intrinsic quadrupole moment, Q_0 as

$$\lambda = \left[\frac{E_\gamma}{E_{\gamma'}}\right]^5 \frac{(J+1)(J-1+K)(J-1-K)/2K^2(2J+1)}{1+1.148[(g_K-g_R)/Q_0]^2(J+1)(J-1){E_{\gamma'}}^{-2}}, \tag{4.4}$$

where $E_{\gamma'}$ refers to the energy of the $M1(+E2)$ transition, and E_γ to the energy of the $E2$ transition depopulating the same initial state [22], assuming pure $E2$ and $M1$ transitions. Referring to Table 4.2, the intensities of the two transitions de-exciting the 780 keV level yield a $E2$ to $M1$ ratio of $\lambda_{exp} = 0.24 \pm 0.08$.

The ground-state magnetic moment, μ, provides a test of nuclear coupling since it takes into account different g-factors associated with different components of the total angular momentum. It is known from the literature to be -0.7456(5)μ_N based upon laser spectroscopy and nuclear magnetic resonance measurements [34]. From the measured μ, the ground state of ^{33}Mg was determined to be $3/2^-$. The leading order expression for the magnetic moment can be written as [22]

$$\frac{\mu}{J} = g_R + (g_K - g_R)\frac{K^2}{J(J+1)}, \tag{4.5}$$

where g_K and g_R refer to the g-factors describing the motion of the valence particle and core, respectively.

The intrinsic electric quadrupole moment describes the extent that the nuclear charge distribution deviates from spherical symmetry, or in other words, the extent to which the nuclear charge distribution is deformed. To obtain a value for the intrinsic quadrupole moment, we utilize a previous Coulomb excitation measurement of ^{33}Mg on a gold

target [35]. Ref. [35] assumed a $5/2^+$ ground state and an excitation to an observed $7/2^+$ state and an unobserved $9/2^+$ state to obtain a $B(E2\uparrow)$ of 232(107) e^2fm^4. Their uncertainties take into account the possibility that the $9/2^+$ state may decay to the $7/2^+$ state anywhere from 0% to 100% of the time. If instead, we assume a $3/2^-$ ground state for ^{33}Mg, Coulomb excitation should populate the $7/2^-$ state. Using our level scheme, branching ratios, and proposed J^π values, we would expect to observe a Coulomb excitation spectrum with strongly populated 483 keV and 297 keV levels. This is, in fact, consistent with the spectrum from Ref. [35], where the low-energy background is likely obscuring the 297 keV transition. Then, based on the measured B($E2$) value, and the excitation scheme from our work, we can extract a Q_0 value of 0.7(0.16) eb. The intrinsic quadrupole moment can be approximated classically as an ellipsoid [73],

$$Q_0 = q\frac{(\frac{C}{A})^2 - 1}{(\frac{C}{A})^2/3}, \tag{4.6}$$

where the ratio of the major and minor axes of the ellipsoid can be written as $((1+\frac{1}{3})\varepsilon_2)/(1-\frac{2}{3})$, and $q = \frac{2}{5}ZR^2$, with $R = r_0A^{1/3}$ and $r_0 = 1.2$ fm.

In order to determine if the available experimental observables for ^{33}Mg can be described in the strong coupling limit, each observable is calculated as a function of the quadrupole deformation parameter, ε_2. If a consistent range of ε_2 can be found where the calculations agree with the experimental observables, then a consistent picture for ^{33}Mg as a strongly coupled rotational band has emerged.

Prior to calculating λ and μ, the g-factors and Q_0 were calculated. In the Nilsson framework, the g-factor for an odd-A system can be separated into two components: g_K, which accounts for the motion of the odd neutron (in this case), and g_R, which describes the motion of the core. For ^{33}Mg, the odd-neutron g_K factor was calculated as

$$g_K = g_\ell + (g_s - g_\ell)\frac{< s_3 >}{K}, \tag{4.7}$$

Table 4.4: Parameters used to calculate the intensity ratio λ, ground-state magnetic moment (μ), and Q_0 of ^{33}Mg as a function of deformation (ε_2). The experimental values for λ, Q_0 [35], and μ [34] are shown in the last row of the table.

ε_2	$< s_3 >$	g_K	Q_0 (eb)	$\mu(\mu_N)$	λ
0.2	-0.31	-0.79	0.32	-0.53	0.048
0.3	-0.35	-0.89	0.51	-0.62	0.10
0.4	-0.39	0.99	0.74	-0.72	0.18
0.5	-0.41	-1.04	1.01	-0.76	0.31
Experimental			0.7(0.16)	-0.7456(5)	0.24(8)

where g_ℓ is the orbital angular momentum g-factor and is zero for neutrons, g_s is the spin g-factor and is -3.8263 for neutrons, and $< s_3 >$ is the projection of the spin onto the symmetry axis of the nucleus calculated as a function of deformation in a standard Nilsson code [21, 72] (see Table 4.4 for the values of $< s_3 >$). The core g-factor, g_R, is usually approximated by Z/A, but measured values of g_R are typically comparable to, or slightly smaller than this approximation [22]. The Z/A approximation for ^{33}Mg yields a value of 0.36 for g_R; we ultimately consider g_R as an additional parameter that can be varied to optimize agreement with the data.

After calculation of g_K and Q_0, both μ and λ were calculated as functions of deformation. The value for g_R was adjusted to 0.30, and λ, Q_0, and μ all show good agreement within a narrow range of ε_2 when compared to their experimental values. Table 4.4 summarizes the calculated parameters as well as the experimental values.

Fig. 4.7 shows the calculations for λ, Q_0, and μ along with their experimental values (with shaded error bands). Each panel corresponds to one of the experimental observables; the blue dashed lines correspond to the experimental value with shaded error bands and the

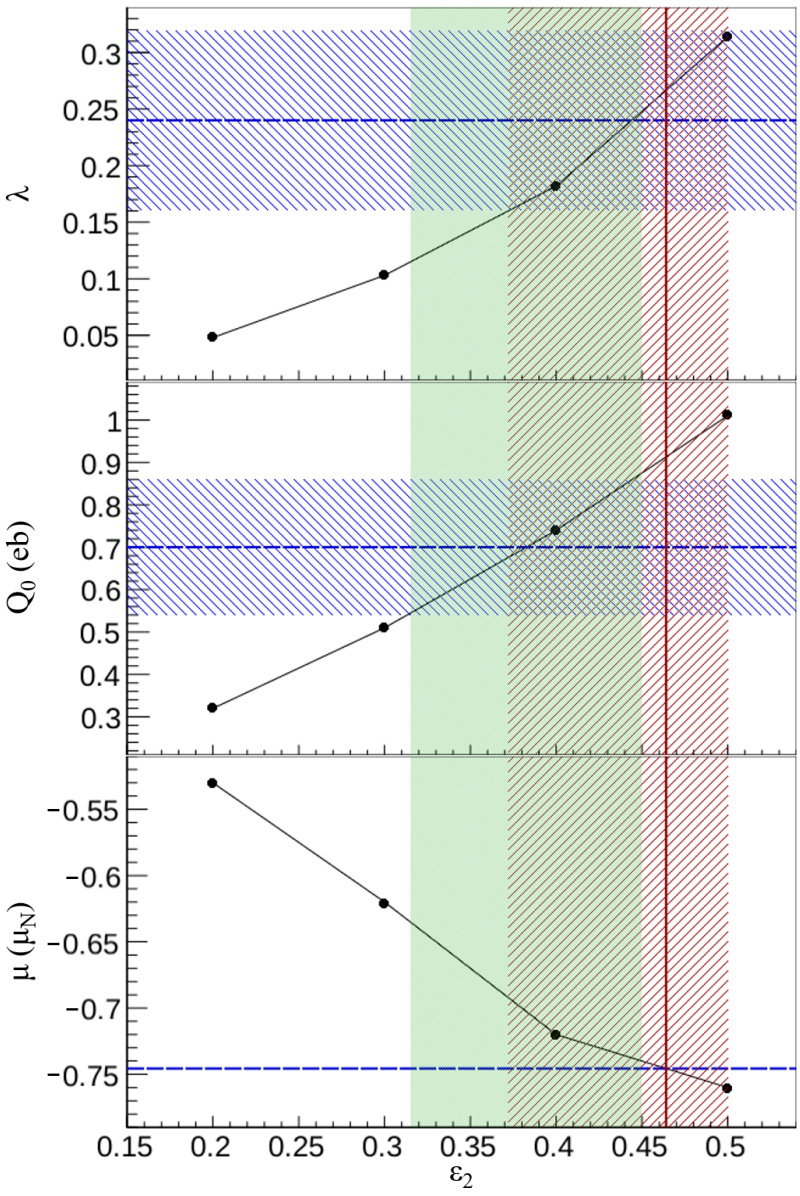

Figure 4.7: The calculations for λ, Q_0, and μ are shown in the three panels. The measured values are denoted with dashed blue lines with shaded error bands. The error band on the experimental value of μ is sufficiently small and appears as a line instead of an error band. The vertical red error band denotes the agreement range for the calculated λ and experimental value and the green vertical band denotes the range where the calculated Q_0 and the experimental value agree.

black points and connected lines represent the calculations. The measured value of μ has good precision and results in a narrow range of ε_2 where the calculation is in agreement with the experiment. This is represented by the solid, red vertical line. In contrast, the experimental values of the intensity ratio (λ_{exp}) and intrinsic quadrupole moment (Q_0) have larger uncertainties and yield wider ranges of deformation where the calculated parameters for λ and Q_0 agree with their experimental values. This is denoted by the vertical, red hashed and solid green bands in Figure 4.7, respectively.

The agreement between these experimental observables and the simple leading order calculations presented here, for a reasonable deformation of 0.4 - 0.5, would seem to suggest that the tentative spins and parities presented in Table 4.2 show a consistent picture, and the low-lying structure populated in ^{33}Mg can be described as a strongly coupled rotational band.

Table 4.5: Calculations for λ, μ, and Q_0 using the effective values $g_{\ell,eff} = -0.1$ and $g_{s,eff} = 0.9\ g_{s,free}$ for the g-factors.

ε_2	$< s_3 >$	$g_{K,eff}$	Q_0 (eb)	$\mu(\mu_N)$	λ
0.2	-0.31	-0.81	0.32	-0.55	0.046
0.3	-0.35	-0.90	0.51	-0.63	0.10
0.4	-0.39	1.00	0.74	-0.72	0.18
0.5	-0.41	-1.04	1.01	-0.76	0.32
Experimental			0.7(0.16)	-0.7456(5)	0.24(8)

The results above were obtained using the free values for both $g_{\ell,free} = 0$ and $g_{s,free} = -3.8263$. Taking into account in-medium effects on the g-factors, we can also reproduce the data by considering the effective values $g_{\ell,eff} = -0.1$ and $g_{s,eff} = 0.9\ g_{s,free}$

which compensate the orbital and spin contributions to the magnetic moments and are in line with the analysis in Refs. [22, 74, 75]. Table 4.5 summarizes the calculations using the effective *g*-factor values. The results are in good agreement with the experimental observables regardless of whether the effective values are used or not.

5 Summary and Outlook

The "island of inversion" isotopes, ^{33}Mg and ^{33}Al, were studied in this dissertation using in-beam γ-spectroscopy and β-decay studies. Low energy yrast states in ^{33}Mg were populated using a two-stage projectile fragmentation technique and γ-rays were observed using GRETINA. The level scheme was constructed using $\gamma - \gamma$ coincidences and γ intensities, and two new γ-ray transitions depopulating a new level at 780(6) keV were placed. Using the newly placed third member of the rotational band and assuming tentative spin assignments built on a $K = 3/2$ bandhead, the experimental excitation energies, $E2/M1$ ratio, magnetic moment, and intrinsic quadrupole moment were compared to leading order approximations in the rotational framework in the strong coupling limit, and a consistent picture emerged.

A β-decay study was also completed for the decay of ^{32}Na, ^{33}Na, and ^{33}Mg. The level scheme for ^{33}Mg was constructed based on $\gamma - \gamma$ coincidences and γ-singles analysis, and the decay scheme for ^{33}Na to states in ^{33}Mg was built and analyzed. Using $\log(fT)$ analysis, tentative J^π values were assigned to each level. The J^π values were in accordance with the adopted levels from the literature. Following the decay of ^{33}Na and ^{33}Mg, ^{33}Al was studied and several γ-ray transitions were observed.

5.1 Discussion of ^{33}Mg Level Schemes

Fig. 5.1 shows a side-by-side comparison of the level schemes resulting from the e11029 (left) and e14063 (right) measurements. The J^π values for the e11029 experiment are those proposed by the current work and the J^π values for e14063 are taken based upon the current $\log(fT)$ analysis and literature arguments. The tentative J^π assignments obtained from our rotational analysis are in agreement with the those from the β-decay measurement. While the adopted J^π (from ENSDF) for the 483 keV level is listed as $\frac{3}{2}^-$ based on shell model calculations from Ref. [29], their $\log(fT)$ analysis is consistent

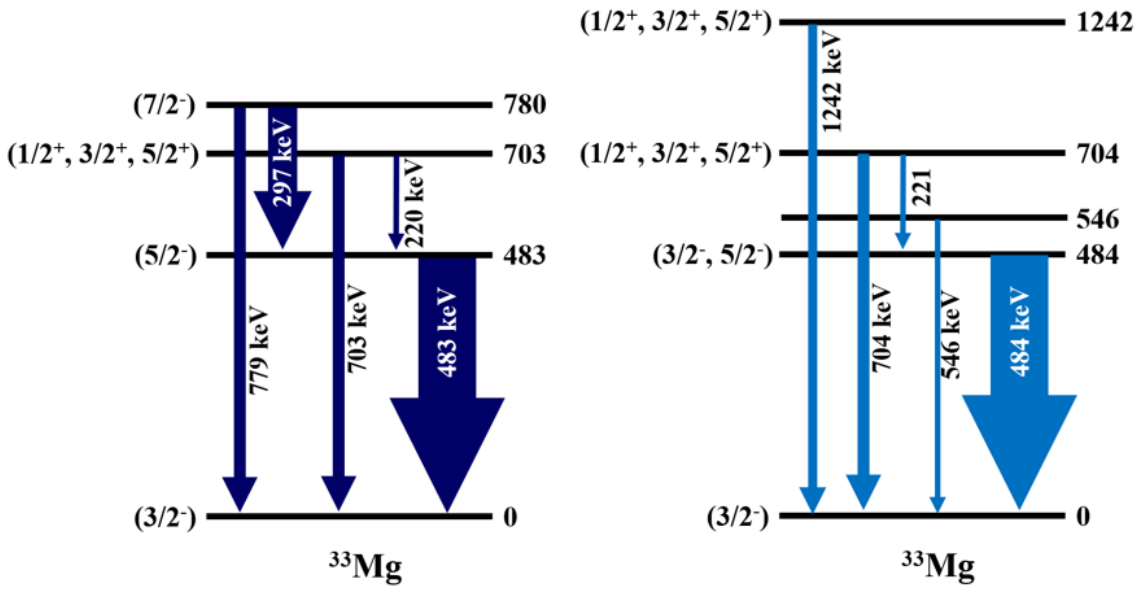

Figure 5.1: The level scheme for ^{33}Mg from the e11029 experiment is shown on the left (dark blue) and for e14063 on the right (light blue).

with a *1st forbidden* transition, which is observed in our work as well. Additionally, considering the comment from Ref. [35] concerning the $E2$ nature of the transition, a J^{π} assignment of $\frac{5}{2}^{-}$ is in better agreement with the literature and what is observed in both of our measurements.

The proposed $\frac{7}{2}^{-}$ 780 keV level was not observed in the β-decay study. The decay to the 780 keV level would exhibit a change in parity and a ΔJ of 2, which, based on selection rules, would classify the decay as *2nd forbidden*. Given our statistics and the probability of observing a *2nd forbidden* decay, it is reasonable that the 780 keV level was not observed in our β-decay experiment.

Overall, the level schemes for ^{33}Mg constructed from each experiment are consistent with one another.

5.2 Future Work

The work presented in this dissertation has provided necessary information about ^{33}Mg, but there is still more that can be said about the "island of inversion." Additional work needs to be done to ascertain firm J^π values for each level in the level scheme in order to provide more concrete assignments and clarify the results of previous decay studies and the proposed J^π values from the current rotational work. J^π values could be obtained from β-decay studies with higher statistics, where the γ-ray detectors were placed at a range of angles in order to perform angular correlation measurements and determine $\Delta\ell$.

Furthermore, additional levels in the rotational band for ^{33}Mg need to be observed to validate the strongly coupled rotational framework that was presented in Chapter 4. Based on the energy relations presented, we predict the $9/2^-$ band member at ~1400 keV, but further experimental effort is required to observe the $9/2^-$ and additional members in the ground-state rotational band. Likewise, rotational studies for other nuclei in the "island of inversion" would enhance our understanding of the deformation in the region. This could be achieved with the same kind of reaction mechanism with more intense beams, or by using Coulomb excitation measurements to populate higher J^π states.

BIBLIOGRAPHY

[1] "National Nuclear Data Center," http://www.nndc.bnl.gov/, accessed: 2017-07-11.

[2] B.A. Brown, "Lecture Notes in Nuclear Structure Physics," (2005).

[3] W. M. Elsasser, J. Phys. le Radium **4 (10)**, 549 (1933).

[4] Maria Mayer, Phys. Rev. **74**, 235 (1948).

[5] Otto Haxel, J. Jensen, Hans Suess, Phys. Rev. **75 (11)**, 1969 (1949).

[6] Maria Goeppert Mayer, Phys. Rev. **75 (12)**, 235 (1948).

[7] "The Nuclear Shell Model," http://oer.physics.manchester.ac.uk/, Accessed: 11-20-2017.

[8] B.A. Brown, Physics **3**, 104 (2010).

[9] C. Thibault, R. Klapisch, C. Rigaud, A.M. Poskanzer, R. Prieels, L. Lessard, and W. Reisdorf, Phys. Rev. C **12**, 644 (1975).

[10] X. Campi, H. Flocard, A.K. Kerman, and S. Koonin, Nucl. Phys. A **251**, 193 (1975).

[11] C. Detraz, M. Langevin, M.C. Goffri-Kouassi, D. Guillemaud, M. Epherre, G. Audi, C. Thibault, and F. Touchard, Nucl. Phys. A **394**, 378 (1983).

[12] E.K. Warburton, J.A. Becker, B.A. Brown, Phys. Rev. C **41**, 1147 (1990).

[13] A. Poves, J. Retamosa, Phys. Lett. B **184**, 311 (1987).

[14] T. Otsuka, R. Fujimoto, Y. Utsuno, B. A. Brown, M. Honma, and T. Mizusaki, Phys. Rev. Lett. **87**, 082502 (2001).

[15] T. Otsuka, T. Suzuki, R. Fujimoto, H. Grawe, and Y. Akaishi, Phys. Rev. Lett. **95**, 232502 (2005).

[16] G. Gamow, Z. Phys. **51**, 204 (1928).

[17] N. Bohr, Nature **137**, 344 (1936).

[18] J. Rainwater, Phys. Rev. **79**, 432 (1950).

[19] A. Bohr, Dan. Mat. Fys. Medd **26 (14)** (1952).

[20] A. Bohr and B. Mottelson, Dan. Mat. Fys. Medd **27(16)** (1953).

[21] S. G. Nilsson, Dan. Mat. Fys. Medd **16**, 29 (1955).

[22] A. Bohr and B. Mottelson, *Nuclear Structure*, Vol. II (W. A. Benjamin, Inc., Advanded Book Program, Reading, 1975).

[23] K. Heyde, *Basic Ideas and Concepts in Nuclear Physics*, 3rd ed. (IoP, 2005).

[24] S.G. Nilsson, I. Ragnarsson, *Shapes and Shells in Nuclear Structure* (Cambridge University Press, Cambridge, 1995).

[25] W.D. Loveland, D.J. Morrissey, and G. T. Seaborg, *Modern Nuclear Chemistry* (John Wiley and Sons, Inc., Hoboken, NJ, 2006).

[26] D. Guillemaud-Mueller, C. Detraz, M. Langevin, F. Naulin, M. de Saint-Simon, C. Thibault, F. Touchard, and M. Epherre, Nucl. Phys. A **426**, 37 (1984).

[27] X. Zhou, X. Tu, J. Wouters, D. Vieira, K. Lbner, H. Seifert, Z. Zhou, and G. Butler, Phys. Lett. B **260**, 285 (1991).

[28] N. Orr, W. Mittig, L. Fifield, M. Lewitowicz, E. Plagnol, Y. Schutz, Z. W. Long, L. Bianchi, A. Gillibert, A. Belozyorov, S. Lukyanov, Y. Penionzhkevich, A. Villari, A. Cunsolo, A. Foti, G. Audi, C. Stephan, and L. Tassan-Got, Phys. Lett. B **258**, 29 (1991).

[29] S. Nummela, F. Nowacki, P. Baumann, E. Caurier, J. Cederkäll, S. Courtin, P. Dessagne, A. Jokinen, A. Knipper, G. Le Scornet, L. G. Lyapin, C. Miehé, M. Oinonen, E. Poirier, Z. Radivojevic, M. Ramdhane, W. H. Trzaska, G. Walter, J. Äystö, and I. Collaboration, Phys. Rev. C **64**, 054313 (2001).

[30] Z. Radivojevic, P. Baumann, E. Caurier, J. Cederkll, S. Courtin, P. Dessagne, A. Jokinen, A. Knipper, G. Scornet, V. Lyapin, C. Mieh, F. Nowacki, S. Nummela, M. Oinonen, E. Poirier, M. Ramdhane, W. Trzaska, G. Walter, and J. yst, Nucl. Instrum. Methods Phys. Res., Sect. A **481**, 464 (2002).

[31] A. Morton, P. Mantica, B. Brown, A. Davies, D. Groh, P. Hosmer, S. Liddick, J. Prisciandaro, H. Schatz, M. Steiner, and A. Stolz, Phys. Lett. B **544**, 274 (2002).

[32] C. Gaulard, G. Audi, C. Bachelet, D. Lunney, M. de Saint Simon, C. Thibault, and N. Vieira, Nucl. Phys. A **766**, 52 (2006).

[33] D. Lunney, G. Audi, C. Gaulard, M. de Saint Simon, C. Thibault, and N. Vieira, Eur. Phys. J. A **28**, 129 (2006).

[34] D. T. Yordanov, M. Kowalska, K. Blaum, M. De Rydt, K. T. Flanagan, P. Lievens, R. Neugart, G. Neyens, and H. H. Stroke, Phys. Rev. Lett. **99**, 212501 (2007).

[35] B. V. Pritychenko, T. Glasmacher, P. D. Cottle, R. W. Ibbotson, K. W. Kemper, L. A. Riley, A. Sakharuk, H. Scheit, M. Steiner, and V. Zelevinsky, Phys. Rev. C **65**, 061304 (2002).

[36] K. Yoneda, H. Sakurai, T. Gomi, T. Motobayashi, N. Aoi, N. Fukuda, U. Futakami, Z. Gacsi, Y. Higurashi, N. Imai, N. Iwasa, H. Iwasaki, T. Kubo, M. Kunibu, M. Kurokawa, Z. Liu, T. Minemura, A. Saito, M. Serata, S. Shimoura, S. Takeuchi, Y. Watanabe, K. Yamada, Y. Yanagisawa, K. Yogo, A. Yoshida, and M. Ishihara, Phys. Lett. B **499**, 233 (2001).

[37] Z. Elekes, Z. Dombrádi, A. Saito, N. Aoi, H. Baba, K. Demichi, Z. Fülöp, J. Gibelin, T. Gomi, H. Hasegawa, N. Imai, M. Ishihara, H. Iwasaki, S. Kanno, S. Kawai, T. Kishida, T. Kubo, K. Kurita, Y. Matsuyama, S. Michimasa, T. Minemura, T. Motobayashi, M. Notani, T. Ohnishi, H. J. Ong, S. Ota, A. Ozawa, H. K. Sakai, H. Sakurai, S. Shimoura, E. Takeshita, S. Takeuchi, M. Tamaki, Y. Togano, K. Yamada, Y. Yanagisawa, and K. Yoneda, Phys. Rev. C **73**, 044314 (2006).

[38] T. Fukui, S. Ota, S. Shimoura, N. Aoi, E. Takeshita, S. Takeuchi, H. Suzuki, H. Baba, T. Fukuchi, Y. Hashimoto, E. Ideguchi, K. Ieki, N. Iwasa, H. Iwasaki, S. Kanno, Y. Kondo, T. Kubo, K. Kurita, T. Minemura, S. Michimasa, T. Motobayashi, T. Murakami, T. Nakabayashi, T. Nakamura, M. Niikura, T. Okumura, T. K. Onishi, H. Sakurai, M. Shinohara, D. Suzuki, M. K. Suzuki, M. Tamaki, K. Tanaka, Y. Togano, Y. Wakabayashi, and K. Yamada, *High Resolution In-beam Gamma Spectroscopy of N ~ 20 Neutron-rich Nuclei*, Tech. Rep. CNS-REP-69,P19 (2006).

[39] D. Morrissey, B.M. Sherrill, M. Steiner, A. Stolz, and I. Wiedenhoever, Nucl. Instrum. Methods Phys. Res., Sect. B **204**, 90 (2003).

[40] A. Stolz, T. Baumann, T.N. Ginter, D.J. Morrissey, M. Portillo, B.M. Sherrill, M. Steiner, and J.W. Stetson, Nucl. Instr. and Meth. B **241**, 858 (2005).

[41] Glenn Knoll, *Radiation Detection and Measurement*, 4th ed. (Wiley, 2010).

[42] K. Starosta, C. Vaman, D. Miller, P. Voss, D. Bazin, T. Glasmacher, H. Crawford, P. Mantica, H. Tan, W. Hennig, M. Walby, A. Fallu-Labruyere, J. Harris, D. Breus, P. Grudberg, and W. Warburton, Nuclear Instruments and Methods in Physics Research Section A: Accelerators, Spectrometers, Detectors and Associated Equipment **610**, 700 (2009).

[43] C. Prokop, S. Liddick, B. Abromeit, A. Chemey, N. Larson, S. Suchyta, and J. Tompkins, Nuclear Instruments and Methods in Physics Research Section A: Accelerators, Spectrometers, Detectors and Associated Equipment **741**, 163 (2014).

[44] N. Larson, S. Liddick, M. Bennett, A. Bowe, A. Chemey, C. Prokop, A. Simon, A. Spyrou, S. Suchyta, S. Quinn, S. Tabor, P. Tai, V. Tripathi, and J. VonMoss, Nucl. Instrum. Methods Phys. Res., Sect. A **727**, 59 (2013).

[45] W. Mueller, J. Church, T. Glasmacher, D. Gutknecht, G. Hackman, P. Hansen, Z. Hu, K. Miller, and P. Quirin, Nucl. Instrum. Methods Phys. Res., Sect. A **466**, 492 (2001).

[46] C. J. Prokop, *Shape Coexistence in the Neutron-rich Nickel Isotopes near N = 40*, PhD dissertation, Michigan State University (2016).

[47] D. Bazin, J.A. Caggiano, B.M. Sherrill, J. Yurkon, and A. Zeller, Nucl. Instrum. Methods Phys. Res., Sect. B **204**, 629 (2003).

[48] J. Yurkon, D. Bazin, W. Benenson, D.J. Morrissey, B.M. Sherrill, D. Swan, and R. Swanson, Nucl. Instrum. Methods Phys. Res., Sect. A **422**, 291 (1999).

[49] K. Meierbachtol, D. Bazin, and D.J. Morrissey, Nucl. Instrum. Methods Phys. Res., Sect. A **652**, 668 (2011).

[50] "The NSCL S800 Spectrograph," https://wikihost.nscl.msu.edu/S800Doc/doku.php, Accessed: 04-18-2017.

[51] M. Berz, K. Joh, J. A. Nolen, B. M. Sherrill, and A. F. Zeller, Phys. Rev. C **47**, 537 (1993).

[52] "S800 Spectrograph Inverse Maps Server," http://maps.nscl.msu.edu/~s800maps/, accessed: 2017-08-31.

[53] L. Riley *et al.*, to be published.

[54] O. Tarasov and D. Bazin, Nucl. Instr. Meth. B **266**, 4657 (2008).

[55] C. Detraz, M. Epherre, D. Guillemaud, P. Hansen, B. Jonson, R. Klapisch, M. Langevin, S. Mattsson, F. Naulin, G. Nyman, A. Poskanzer, H. Ravn, M. de Saint-Simon, K. Takahashi, C. Thibault, and F. Touchard, Phys. Lett. B **94**, 307 (1980).

[56] M. Langevin, C. Dtraz, D. Guillemaud-Mueller, A. Mueller, C. Thibault, F. Touchard, and M. Epherre, Nucl. Phys. A **414**, 151 (1984).

[57] G. Klotz, P. Baumann, M. Bounajma, A. Huck, A. Knipper, G. Walter, G. Marguier, C. Richard-Serre, A. Poves, and J. Retamosa, Phys. Rev. C **47**, 2502 (1993).

[58] V. Tripathi, S. L. Tabor, P. Bender, C. R. Hoffman, S. Lee, K. Pepper, M. Perry, P. F. Mantica, J. M. Cook, J. Pereira, J. S. Pinter, J. B. Stoker, D. Weisshaar, Y. Utsuno, and T. Otsuka, Phys. Rev. C **77**, 034310 (2008).

[59] C. M. Mattoon, F. Sarazin, G. Hackman, E. S. Cunningham, R. A. E. Austin, G. C. Ball, R. S. Chakrawarthy, P. Finlay, P. E. Garrett, G. F. Grinyer, B. Hyland, K. A. Koopmans, J. R. Leslie, A. A. Phillips, M. A. Schumaker, H. C. Scraggs, J. Schwarzenberg, M. B. Smith, C. E. Svensson, J. C. Waddington, P. M. Walker, B. Washbrook, and E. Zganjar, Phys. Rev. C **75**, 017302 (2007).

[60] J. Hardy, L. Carraz, B. Jonson, and P. Hansen, Physics Letters B **71**, 307 (1977).

[61] P. Doornenbal, H. Scheit, N. Kobayashi, N. Aoi, S. Takeuchi, K. Li, E. Takeshita, Y. Togano, H. Wang, S. Deguchi, Y. Kawada, Y. Kondo, T. Motobayashi, T. Nakamura, Y. Satou, K. N. Tanaka, and H. Sakurai, Phys. Rev. C **81**, 041305 (2010).

[62] S. Paschalis, I. Y. Lee, A. O. Macchiavelli, C. M. Campbell, M. Cromaz, S. Gros, J. Pavan, J. Qian, R. M. Clark, H. L. Crawford, D. Doering, P. Fallon, C. Lionberger, T. Loew, M. Petri, T. Stezelberger, S. Zimmermann, D. C. Radford, K. Lagergren, D. Weisshaar, R. Winkler, T. Glasmacher, J. T. Anderson, and C. W. Beausang, Nucl. Instrum. Methods Phys. Res., Sect. A **709**, 44 (2013).

[63] H. L. Crawford, P. Fallon, A. O. Macchiavelli, A. Poves, V. M. Bader, D. Bazin, M. Bowry, C. M. Campbell, M. P. Carpenter, R. M. Clark, M. Cromaz, A. Gade, E. Ideguchi, H. Iwasaki, C. Langer, I. Y. Lee, C. Loelius, E. Lunderberg, C. Morse, A. L. Richard, J. Rissanen, D. Smalley, S. R. Stroberg, D. Weisshaar, K. Whitmore, A. Wiens, S. J. Williams, K. Wimmer, and T. Yamamato, Phys. Rev. C **93**, 031303 (2016).

[64] H. Iwasaki, T. Motobayashi, H. Sakurai, K. Yoneda, T. Gomi, N. Aoi, N. Fukuda, Z. Flp, U. Futakami, Z. Gacsi, Y. Higurashi, N. Imai, N. Iwasa, T. Kubo, M. Kunibu, M. Kurokawa, Z. Liu, T. Minemura, A. Saito, M. Serata, S. Shimoura, S. Takeuchi, Y. Watanabe, K. Yamada, Y. Yanagisawa, and M. Ishihara, Phys. Lett. B **522**, 227 (2001).

[65] J. A. Church, C. M. Campbell, D. C. Dinca, J. Enders, A. Gade, T. Glasmacher, Z. Hu, R. V. F. Janssens, W. F. Mueller, H. Olliver, B. C. Perry, L. A. Riley, and K. L. Yurkewicz, Phys. Rev. C **72**, 054320 (2005).

[66] D. T. Yordanov for the COLLAPS Collaboration, Hyperfine Interactions **196**, 53 (2010).

[67] C. Détraz, D. Guillemaud, G. Huber, R. Klapisch, M. Langevin, F. Naulin, C. Thibault, L. C. Carraz, and F. Touchard, Phys. Rev. C **19**, 164 (1979).

[68] T. Motobayashi, Y. Ikeda, K. Ieki, M. Inoue, N. Iwasa, T. Kikuchi, M. Kurokawa, S. Moriya, S. Ogawa, H. Murakami, S. Shimoura, Y. Yanagisawa, T. Nakamura, Y. Watanabe, M. Ishihara, T. Teranishi, H. Okuno, and R. Casten, Phys. Lett. B **346**, 9 (1995).

[69] B. V. Pritychenko, T. Glasmacher, P. D. Cottle, M. Fauerbach, R. W. Ibbotson, K. W. Kemper, V. Maddalena, A. Navin, R. Ronningen, A. Sakharuk, H. Scheit, and V. G. Zelevinsky, Phys. Lett. B **461**, 322 (1999).

[70] V. Chiste, A. Gillibert, A. Lpine-Szily, N. Alamanos, F. Auger, J. Barrette, F. Braga, M. Cortina-Gil, Z. Dlouhy, V. Lapoux, M. Lewitowicz, R. Lichtenthler, R. Neto, S. Lukyanov, M. MacCormick, F. Marie, W. Mittig, F. de Oliveira Santos, N. Orr,

A. Ostrowski, S. Ottini, A. Pakou, Y. Penionzhkevich, P. Roussel-Chomaz, and J. Sida, Phys. Lett. B **514**, 233 (2001).

[71] S. Takeuchi, N. Aoi, T. Motobayashi, S. Ota, E. Takeshita, H. Suzuki, H. Baba, T. Fukui, Y. Hashimoto, K. Ieki, N. Imai, H. Iwasaki, S. Kanno, Y. Kondo, T. Kubo, K. Kurita, T. Minemura, T. Nakabayashi, T. Nakamura, T. Okumura, T. K. Onishi, H. Sakurai, S. Shimoura, R. Sugou, D. Suzuki, M. K. Suzuki, M. Takashina, M. Tamaki, K. Tanaka, Y. Togano, and K. Yamada, Phys. Rev. C **79**, 054319 (2009).

[72] S. Larsson, G. Leander, and I. Ragnarsson, Nucl. Phys. A **307**, 189 (1978).

[73] L.D. Landau, E.M. Lifshitz, and L.P. Pitaevskii, *Electrodynamics of Continuous Media*, 2nd ed. (Pergamon, New York, 1984).

[74] B. A. Brown and B. Wildenthal, Ann. Rev. Nucl. Part. Sci. **38**, 29 (1988).

[75] W. Bentz and A. Arima, Science China **53**, 1 (2010).

Thesis and Dissertation Services